

REPORT DOCUMENTATION PAGE			Form Approved OMB NO. 0704-0188		
<p>The public reporting burden for this collection of information is estimated to average 1 hour per response, including the time for reviewing instructions, searching existing data sources, gathering and maintaining the data needed, and completing and reviewing the collection of information. Send comments regarding this burden estimate or any other aspect of this collection of information, including suggestions for reducing this burden, to Washington Headquarters Services, Directorate for Information Operations and Reports, 1215 Jefferson Davis Highway, Suite 1204, Arlington VA, 22202-4302. Respondents should be aware that notwithstanding any other provision of law, no person shall be subject to any penalty for failing to comply with a collection of information if it does not display a currently valid OMB control number.</p> <p>PLEASE DO NOT RETURN YOUR FORM TO THE ABOVE ADDRESS.</p>					
1. REPORT DATE (DD-MM-YYYY) 30-03-2009		2. REPORT TYPE Final Report		3. DATES COVERED (From - To) 1-Jun-2002 - 30-Sep-2008	
4. TITLE AND SUBTITLE High Average Power Diode-Pumped Solid-State Lasers: Power Scaling with High Spectral and Spatial Coherence			5a. CONTRACT NUMBER DAAD19-02-1-0184		
			5b. GRANT NUMBER		
			5c. PROGRAM ELEMENT NUMBER		
6. AUTHORS R. L. Byer, M. Dignonnet, R. Route, H. Bae, R. Gaume, P. S. Kuo, Y. Lee, T. Plettner, A. Serpry, S. Sinha, K. Urbanek, J. Wisdom, S. Wong			5d. PROJECT NUMBER		
			5e. TASK NUMBER		
			5f. WORK UNIT NUMBER		
7. PERFORMING ORGANIZATION NAMES AND ADDRESSES Stanford University Office of Sponsored Research Board of Trustees of the Leland Stanford Junior University Stanford, CA 94305 -				8. PERFORMING ORGANIZATION REPORT NUMBER	
9. SPONSORING/MONITORING AGENCY NAME(S) AND ADDRESS(ES) U.S. Army Research Office P.O. Box 12211 Research Triangle Park, NC 27709-2211				10. SPONSOR/MONITOR'S ACRONYM(S) ARO	
				11. SPONSOR/MONITOR'S REPORT NUMBER(S) 44032-EL.1	
12. DISTRIBUTION AVAILABILITY STATEMENT Approved for Public Release; Distribution Unlimited					
13. SUPPLEMENTARY NOTES The views, opinions and/or findings contained in this report are those of the author(s) and should not be construed as an official Department of the Army position, policy or decision, unless so designated by other documentation.					
14. ABSTRACT The main program objective was the development of a kilowatt class, cw Nd:YAG diode-laser-pumped solid-state laser (DPSSL) with quantum noise limited amplitude and phase, 24by7 operation capability and the ability to be repaired while in operation. The approach was a master-oscillator power-amplifier (MOPA) laser utilizing a series of zig-zag slab power amplifiers stages. We developed fiber amplifiers at the 200W level to generate power with high optical efficiency that can effectively extract energy from the power amplifier slabs. We also worked on the					
15. SUBJECT TERMS High Average Power Lasers, Diode-Pumped Solid-State Lasers, Power Scaling of High Power Lasers, Spectral and Spatial Coherence, In-band Pumping, Nd:YAG, Yb:YAG, MOPA, Phase Locking, Fiber Amplifiers, Ceramic Laser Host Materials					
16. SECURITY CLASSIFICATION OF:			17. LIMITATION OF ABSTRACT SAR	18. NUMBER OF PAGES	19a. NAME OF RESPONSIBLE PERSON Robert Byer
a. REPORT U	b. ABSTRACT U	c. THIS PAGE U			19b. TELEPHONE NUMBER 650-723-0226

Report Title

High Average Power Diode-Pumped Solid-State Lasers: Power Scaling with High Spectral and Spatial Coherence

ABSTRACT

The main program objective was the development of a kilowatt class, cw Nd:YAG diode-laser-pumped solid-state laser (DPSSL) with quantum noise limited amplitude and phase, 24by7 operation capability and the ability to be repaired while in operation. The approach was a master-oscillator power-amplifier (MOPA) laser utilizing a series of zig-zag slab power amplifiers stages. We developed fiber amplifiers at the 200W level to generate power with high optical efficiency that can effectively extract energy from the power amplifier slabs. We also worked on the generation of high average power visible light by developing nonlinear optical materials with large apertures, low photo-refraction and minimal visible induced infrared absorption.

The second objective was to develop a 1 joule, pulse-modulated, diffraction limited MOPA laser with less than 1 MHz line-width. A follow-on objective was frequency conversion to 1.5 or 2.0 microns for remote sensing applications. We demonstrated Yb:YAG slab lasers pumped with high brightness laser diodes. Supporting this project was the development of laser diodes operating in the 1.5 micron region for pumping of erbium doped laser hosts, and the synthesis of new low-loss polycrystalline laser host materials for in-band pumping into the upper laser level to improve the laser efficiency at eye-safe wavelengths. We developed orientation patterned Ga-As to frequency convert high peak power 1-micron radiation to eye-safe wavelengths in the mid-infrared for defense applications.

The third objective, power scaling and determining the potential for phase-locking of ultra-fast laser systems for a wide range of sensing and machining applications, was demonstrated as well.

List of papers submitted or published that acknowledge ARO support during this reporting period. List the papers, including journal references, in the following categories:

(a) Papers published in peer-reviewed journals (N/A for none)

Number of Papers published in peer-reviewed journals: 25.00

(b) Papers published in non-peer-reviewed journals or in conference proceedings (N/A for none)

Number of Papers published in non peer-reviewed journals: 0.00

(c) Presentations

Number of Presentations: 0.00

Non Peer-Reviewed Conference Proceeding publications (other than abstracts):

Number of Non Peer-Reviewed Conference Proceeding publications (other than abstracts): 0

Peer-Reviewed Conference Proceeding publications (other than abstracts):

Number of Peer-Reviewed Conference Proceeding publications (other than abstracts): 0

(d) Manuscripts

Number of Manuscripts: 0.00

Number of Inventions:

Graduate Students

<u>NAME</u>	<u>PERCENT SUPPORTED</u>
Shailendhar Saraf	0.50
Arun Kumar Sridharan	1.00
Supriyo Sinha	0.50
Jeffrey Alan Wisdom	1.00
Samuel Tin Bo Wong	1.00
Yin-Wen Lee	1.00
Patrick Lu	0.50
FTE Equivalent:	5.50
Total Number:	7

Names of Post Doctorates

<u>NAME</u>	<u>PERCENT SUPPORTED</u>
Shailendhar Saraf,	0.50
Arun Kumar Sridharan	1.00
Supriyo Sinha	0.50
Jeffrey Alan Wisdom	1.00
Samuel Tin Bo Wong	1.00
Yin-Wen Lee	1.00
FTE Equivalent:	5.00
Total Number:	6

Names of Faculty Supported

<u>NAME</u>	<u>PERCENT SUPPORTED</u>	National Academy Member
Robert L. Byer	0.25	Yes
Martin M. Fejer	0.25	No
FTE Equivalent:	0.50	
Total Number:	2	

Names of Under Graduate students supported

<u>NAME</u>	<u>PERCENT SUPPORTED</u>
FTE Equivalent:	
Total Number:	

Student Metrics

This section only applies to graduating undergraduates supported by this agreement in this reporting period

The number of undergraduates funded by this agreement who graduated during this period: 0.00

The number of undergraduates funded by this agreement who graduated during this period with a degree in science, mathematics, engineering, or technology fields:..... 0.00

The number of undergraduates funded by your agreement who graduated during this period and will continue to pursue a graduate or Ph.D. degree in science, mathematics, engineering, or technology fields:..... 0.00

Number of graduating undergraduates who achieved a 3.5 GPA to 4.0 (4.0 max scale):..... 0.00

Number of graduating undergraduates funded by a DoD funded Center of Excellence grant for Education, Research and Engineering:..... 0.00

The number of undergraduates funded by your agreement who graduated during this period and intend to work for the Department of Defense 0.00

The number of undergraduates funded by your agreement who graduated during this period and will receive scholarships or fellowships for further studies in science, mathematics, engineering or technology fields: 0.00

Names of Personnel receiving masters degrees

NAME

Total Number:

Names of personnel receiving PhDs

NAME

Shailendhar Saraf
Arun Kumar Sridharan
Supriyo Sinha
Jeffrey Alan Wisdom
Samuel Tin Bo Wong
Yin-Wen Lee

Total Number:

6

Names of other research staff

NAME

PERCENT SUPPORTED

Romain Gaume	0.60	No
Roger Route	0.40	No
Michel Digonnet	0.12	No
Konstantin Vodopyan	0.20	No
FTE Equivalent:	1.32	

Total Number:

4

Sub Contractors (DD882)

Inventions (DD882)

Final Progress Report
on
High Average Power Diode Pumped Solid State Lasers:
Power scaling with high spectral and spatial coherence

DAAD19-02-1-0184

For the period 09-01-2007 to 09-30-2008
Robert L. Byer, P.I.
Stanford University

Program Objectives

The main program objective was the development of a kilowatt class, cw Nd:YAG diode-laser-pumped solid-state laser (DPSSL) with quantum noise limited amplitude and phase, 24by7 operation capability and the ability to be repaired while in operation. The approach was a master-oscillator power-amplifier (MOPA) laser utilizing a series of zig-zag slab power amplifiers stages. We developed fiber amplifiers at the 200W level to generate power with high optical efficiency that can effectively extract energy from the power amplifier slabs. We also worked on the generation of high average power visible light by developing nonlinear optical materials with large apertures, low photorefractive index and minimal visible induced infrared absorption.

The second objective was to develop a 1 joule, pulse-modulated, diffraction limited MOPA laser with less than 1 MHz linewidth. A follow-on objective was frequency conversion to 1.5 or 2.0 microns for remote sensing applications. We demonstrated Yb:YAG slab lasers pumped with high brightness laser diodes. Supporting this project was the development of laser diodes operating in the 1.5 micron region for pumping of erbium doped laser hosts, and the synthesis of new low-loss polycrystalline laser host materials for in-band pumping into the upper laser level to improve the laser efficiency at eye-safe wavelengths. We developed orientation patterned Ga-As to frequency convert high peak power 1-micron radiation to eye-safe wavelengths in the mid-infrared for defense applications.

The third objective, power scaling and determining the potential for phase-locking of ultrafast laser systems for a wide range of sensing and machining applications, was demonstrated as well.

Table of Contents

Executive Summary of program accomplishments	6
I. High Average Power Nd:YAG MOPA system	9
<i>(D. S. Hum, P. Lu, S. Sinha, K. Urbanek, R. L. Byer)</i>	
1. Introduction	9
2. Prior Progress	9
3. Conclusions	15
II. High Average Power Fiber MOPA System	17
<i>(Y. W. Lee, S. Sinha, K. E. Urbanek, M. J. F. Digonnet, R. L. Byer)</i>	
1. Introduction	17
2. Progress	17
2.1 Background	17
2.2 New developments in Yb ⁺ -doped silica fiber based systems	18
2.3 New developments in Yb ⁺ -doped phosphate fiber based systems	33
3. Conclusions and recommendations for further work in fiber MOPA systems	47
III. Ceramic Laser Development Program	50
<i>(R. Gaume, J. Wisdom, R. Feigelson, R. Route, and R. L. Byer)</i>	
1. Introduction	50
2. Progress on the fabrication of ceramics	50
3. Progress on the design of engineered ceramic gain media	56
IV. Phase-Stable Ultra-Short-Pulse Systems	61
<i>(T. Plettner, S. Sinha, S. Wong, R. L. Byer)</i>	
1. Introduction	61
2. Progress to date	61
3. Summary and suggested studies on phase-stable, ultra-short pulse systems	69
V. 1.48 mm Laser Diodes for In-Band Pumping of Erbium-Doped Laser Hosts	71
<i>(H. Bae, T. Sarmiento, J. S. Harris Jr)</i>	
1. Introduction	71
2. Progress	71
3. Summary and directions for future work on 1.48 μ m laser diodes for in-band pumping of erbium-doped laser hosts	79
VI. Optical Parametric Generation in QPM-GaAs	81
<i>(P.S. Kuo, K.L. Vodopyanov, M.M. Fejer)</i>	
1. Introduction	81
2. Progress	81
3. Directions for future research on OP-GaAs devices	90
VII. Publications and proceedings	92
1. Refereed Publications	92
2. Proceedings	95
3. Collected Reprints	96

Executive summary of program accomplishments

This is the final technical report for the fifth year of a five-year program on the power scaling of high average power, diode-pumped solid-state lasers, DAAD-02-1-0184. The program evolved from its inception to include strong research components on new, engineerable laser and nonlinear optical gain media in addition to power scaling of traditional laser gain media such as Nd:YAG and Yb:YAG in master oscillator, power amplifier (MOPA) architectures. The highlights of our progress in this final program period are summarized below.

During the course of the program, we developed the edge-pumped zig-zag slab laser geometry and we made considerable progress in increasing the reliability and demonstrating high extraction efficiency, quantum-noise limited operation of an Nd:YAG slab MOPA system. We re-designed and tested Nd:YAG slabs for the final stage of a reliable 200 W power amplifier. We investigated the use of periodically poled stoichiometric lithium tantalate for frequency doubling of high average, high peak power near-IR systems to the visible part of the spectrum.

We have focused on developing tools to integrate fiber amplifiers into MOPA systems to improve reliability and repeatability. We investigated and tested fiber tapers and silicate bonding for improved signal launching and beam expanding, respectively. We tested a new large-mode-area laser gain fiber that yielded excellent beam quality with an output power of 50 W at 1064 nm and a polarization extinction ratio of 22 dB. In a parallel effort, we have continued to develop Yb-doped phosphate fiber sources. Within the past year, we generated 20 W from an Yb-doped phosphate fiber host. This is a world record output power for this very promising laser host material. We also invented a novel technique to mitigate photo-darkening in optical gain fibers.

We designed an end-pumped Yb:YAG slab incorporating parasitic suppression techniques that led to a single pass small signal gain exceeding 13 dB at 1030 nm. We also designed and fabricated a periodically poled lithium niobate (PPLN) waveguide optical waveguide amplifier to convert the 1 μm pump wavelength to the eye-safe 1.55- μm wavelength. We measured a single-pass undepleted OPA gain of 45 dB in our chips.

We continued to acquire high temperature ceramic processing equipment intended for the fabrication of transparent ceramic laser host materials. This facility has allowed us to focus on the fabrication and characterization of three cubic oxide materials: YAG, Y_2O_3 and spinel (MgAl_2O_4). We investigated and refined a number of parallel approaches to fabricate transparent ceramics in these materials, and we are now able to reproducibly attain transparent polycrystalline samples. During the final program year, we successfully demonstrated laser action in our Nd:YAG ceramic material. In addition, we pursued the fabrication of composite ceramic structures which will be required to generate laser outputs exceeding a few hundred watts with high-beam quality in an all-solid-state laser gain medium. This project has been facilitated by the development of an in-house process to diffusion bond composites of dissimilar material together.

We applied two structure and MBE growth optimizations to our 1.55 μm laser diode development program to obtain 250 mW cw with 41% external efficiency in a 20 μm x 2933 μm device. We were also able to obtain 650 mW of peak power from this same device at a duty cycle of 0.1%.

We demonstrated a novel source of stable frequency combs for the middle infrared, namely a self-phase-locked degenerate synchronously pumped optical parametric oscillator (SPOPO). A femtosecond mode-locked laser was employed as the pump and the nonlinear gain element consisted of a short periodically poled MgO-doped lithium niobate crystal that was type I phase-matched. The output of the degenerate SPOPO was transform-limited and exhibited significant spectral comb broadening. Various techniques showed that the degenerate SPOPO was indeed phase-locked and stable. The frequency locking range was also measured and compared with a heuristic model that we developed. Such a system that produces phase-locked frequency combs in the mid-IR would be useful for applications such as high-precision metrology, high-resolution and broadband molecular spectroscopy, and laser-driven particle acceleration.

Finally, during the final program year we investigated the polarization dependence of the orientation-patterned GaAs optical parametric generator that was first reported last year by Kuo et al. in a publication on broadband mid-IR continuum generation in this material. Our results indicate that circularly polarized or unpolarized light can be used to pump the optical parametric generator.

The program has been exceptionally successful in the development of new, high-gain, high-power fiber amplifiers for power scaling 1- μm light in compact, robust geometries and in the fabrication of polycrystalline ceramic laser gain media with fully engineerable dopant densities and dopant distributions with optical properties rivaling those of single crystal devices. Recommendations for further research in all program areas have been included.

I. High Average Power Nd:YAG MOPA system

D. S. Hum, P. Lu, S. Sinha, K. Urbanek, R. L. Byer

1. Introduction

Under DARPA contract DAAD19-02-1-0184, our major task was to make ground-breaking contributions in the field of power scaling diode-pumped Nd:YAG laser systems. Until the task was completed at the beginning of the fourth program interval, we made considerable progress in increasing the reliability of the solid state MOPA system and in demonstrating high extraction efficiency, quantum-noise limited operation of Nd:YAG slab amplifiers. We designed Nd:YAG slabs for a final 200 W power amplifier. We also demonstrated the use of periodically poled stoichiometric lithium tantalate for frequency doubling of high average and high peak power near-IR systems to the visible.

2. Prior Progress

2.1 Background

Master oscillator power amplifier (MOPA) based systems are well suited for power scaling while preserving the spatial and temporal coherence of the master oscillator. In addition, the MOPA architecture allows for a robust laser design with the ability to repair the laser in modules without major disruption to the alignment. As an example, the 10 W Laser Interferometer Gravitational wave Observatory (LIGO) side-pumped Nd:YAG rod MOPA lasers, developed in our laboratory in the mid-1990s and installed at LIGO in 1997, have operated to date for more than 20,000 hours at the LIGO sites [1].

However, rod-based systems are limited by thermally induced distortions and birefringence. Demanding applications, such as advanced remote sensing and coherent LIDAR systems, will require kW class lasers in the near future. The zigzag slab architecture [2], with its nearly one-dimensional thermal gradients, allows power scaling with good beam quality by greatly reducing thermal phase distortions and birefringence [3]. Scaling to high average power levels with good beam quality and degrees of polarization better than 20 dB has been demonstrated with zigzag slab geometry systems [4]. Practical use of slab lasers has, until recently, been limited by the low efficiencies and phase distortions of the prior designs, and by the complexity of pumping and cooling the water-cooled laser head. Most of these engineering problems have now been solved and along with the availability of higher quality YAG crystals, and kW level output from slabs has been demonstrated [5].

Frequency conversion of light in periodically-poled lithium niobate (PPLN) and periodically-poled lithium tantalate (PPLT) have been widely demonstrated during the last decade. Recently, it has been shown that photorefractive damage (PRD) and green-induced infrared absorption (GRIIRA) have limited the performance of congruent PPLN

and PPLT crystals for frequency conversion at room temperature to the visible. These limitations have been mitigated by the development of near-stoichiometric PPLT.

2.2 New developments

2.2.1 Nd:YAG MOPA

In the second annual progress report, we reported that we had received and characterized a set of new 808 nm pump diodes to pump the 200-W power amplifier. We reported initial results of a Gaussian to super-Gaussian converter to improve power extraction from end-pumped slabs. We reported record 532 nm power from a periodically poled crystal through second harmonic generation of the 1064 nm output beam from the Nd:YAG MOPA. We reported on some promising results of our YAG to YAG silicate bonding process. Finally, we reported on techniques that we had employed to suppress parasitic oscillations in our end-pumped slabs that substantially increased our small signal gains.

In the third program period, we did considerable work to make the Nd:YAG MOPA system more reliable and repeatable. Our solid-state MOPA at the beginning of the third program year is shown in Figure 1.

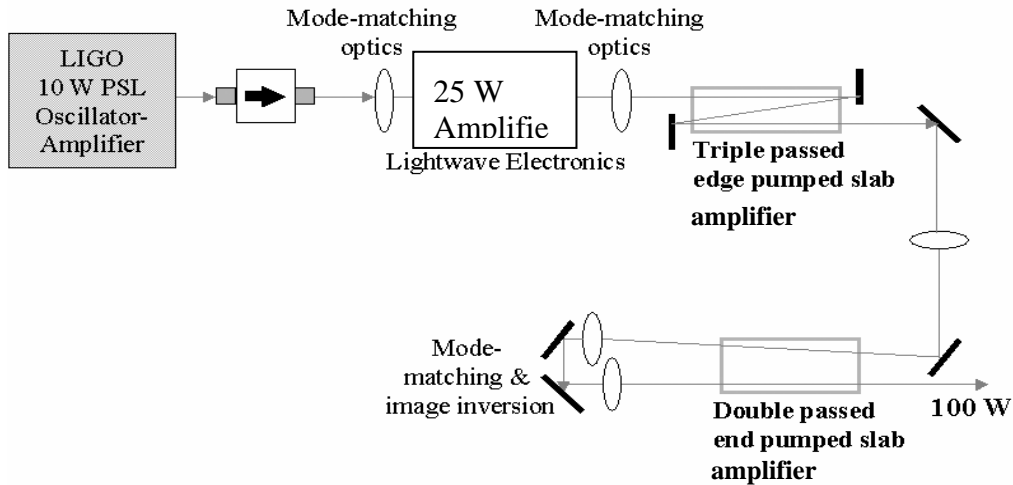


Figure 1 Original experimental setup for 100 W MOPA

Although MOPA systems are very reliable and provide output power despite element failures, the overall system reliability decreases as the number of amplification stages increase. The system shown in Figure 1 has a total of four amplification stages to amplify the NPRO oscillator to the 100 W level. A second issue for the MOPA system shown above arose from the long path length from the oscillator to the power amplifiers. Pointing instability due to thermal drift (and other environmental perturbations) coupled with the long path length led to intensity noise and beam quality fluctuations of the output beam from the power amplifiers. We took two steps to improve the reliability of the system.

First, we removed the triple-passed edge-pumped slab amplifier from the amplifier chain. This reduced the number of amplification stages to three which reduced the power incident on the end-pumped slab from 40 W to 26 W. Second, we inserted a low-finesse mode-cleaner before the end-pumped slab. The mode-cleaner improved the pointing stability and beam quality downstream so that a more stable and more reliable beam was incident on the power amplifiers. The internal losses and mode-matching losses to the mode-cleaner slightly reduced the power incident on the end-pumped slab, from 26 W to 23 W. The system layout of the modified MOPA with a single stage power amplifier is shown below in Fig. 2a. Testing was carried out by pumping with fiber-coupled Laserline diodes that produced 250 W of 808 nm pump power.

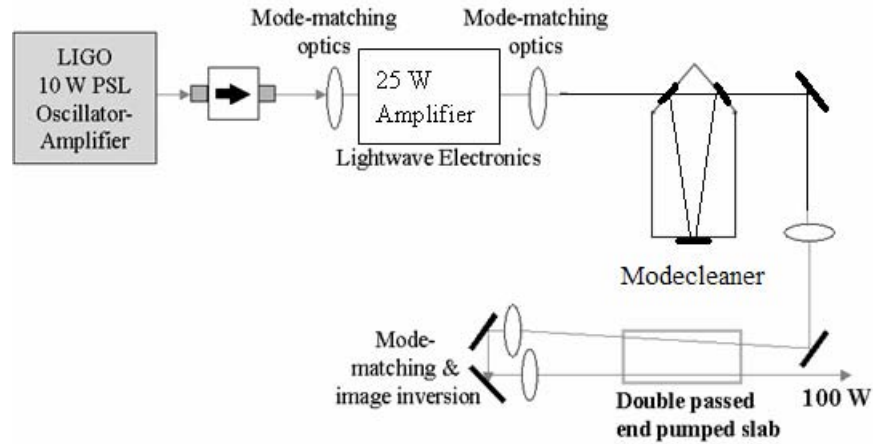


Figure 2a Schematic of modified Nd:MOPA system with increased stability and reliability

We believe that the gain in reliability out-weighted the slight loss in power. Furthermore, the spot size of the saturating beam in the end-pumped slab suggested that we needed only 10 W to saturate the gain of the slab. Thus, 23 W should have been more than sufficient to extract most of the power available from the double-passed first slab, the output of which ultimately reached 84 W. This was well below the 200 W goal of our study, however, so a second double-passed, end-pumped slab amplifier stage (also having non-doped ends) was added to the chain, as illustrated in Fig. 2b. The second amplifier stage was pumped with fiber-coupled 808 nm LIMO diodes with a maximum output power around 400 W. With the exception of a slightly different spot size from this second set of fiber-coupled pump diodes, the pumping geometry for the second end-pumped slab was identical to that of the first. During initial characterization of the second slab's extraction efficiency (35 W from a single pass with 320 W of incident pump power), optical damage occurred at the interface between the central gain-section of the slab and the non-doped diffusion-bonded input end due to excess thermal dissipation. These were the only two slabs with non-doped ends that we had remaining, and we decided to forego the substantial expenses of another slab fabrication run until the reason for the excess thermal loading at the non-doped/doped interface could be identified and the problem solved. We focused our efforts during the fourth program year on studying silicate bonding technology in place of thermal diffusion bonding, as described in the fourth technical progress report.

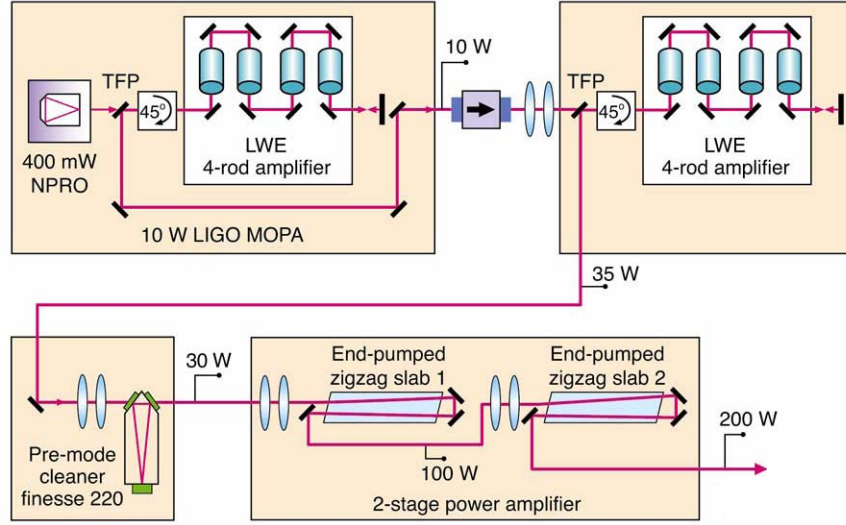


Figure 2b Schematic of Nd:MOPA system with two power amplifier stages

2.2.2 High Energy Second Harmonic Generation

At Stanford, the vapor transport equilibration method has been shown to produce high quality near-stoichiometric PPLT and has enabled the generation of 10W of cw 532-nm radiation by second harmonic generation (SHG) [6]. Typical devices are limited in aperture to the thickness of available substrates, commonly 1 mm. For scaling to high peak and average power [7], large aperture sizes are desirable to avoid surface damage and mitigate thermal effects. Previous work to increase crystal thickness includes periodic poling of lower coercive field materials like KTiOPO_4 (KTP) [8], or magnesium-oxide-doped LN [9]. Diffusion bonding of uniformly poled LN to periodically poled LN has also been used to increase optical aperture [10]. We propose a new topology based on rotated-cut, near-stoichiometric LT (SLT) for scaling to even larger apertures [11]. By periodically poling a rotated-cut crystal, light incident on the large wafer surface can be partially polarized along the extraordinary axis to use the largest nonlinear coefficient and make use of a geometrical projection of the grating k -vector for QPM as illustrated in Fig. 3.

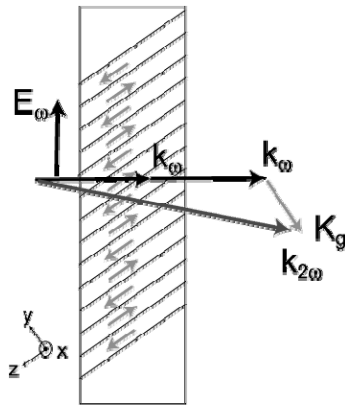


Figure 3 A new topology for large aperture PP crystals. Light propagates through the large wafer face and is partially polarized along the z -axis enabling efficient SHG or other nonlinear interactions

To estimate the expected power scaling capabilities, a measurement of the damage threshold was performed. 3-mm-long, uncoated samples of congruent lithium niobate, CLT and SLT were polished and cleaned for this measurement. A 12-ns-pulsewidth, diffraction-limited, Q-switched, 2.4-mJ, 10-Hz-repetition-rate, 1064-nm Nd:YAG laser was loosely focused to a $55\text{ }\mu\text{m}$ spot ($1/e^2$ -intensity radius) inside the crystal. The length of 3 mm was chosen to avoid damage arising from self-focussing. Detectors were placed to monitor the input energy, the crystal transmission and the scattered radiation. The experimental setup is shown in Fig. 4(a). The dichroic mirror was used to reject any stray second harmonic generation that could corrupt the measurement. By slowly increasing the input energy and monitoring the correlation of damage to crystal transmission and scattered radiation, multi-shot, laser-annealed damage probability statistics as a function of input energy were collected. We defined the damage fluence as the largest fluence before crystal transmission began to decline which was correlated with a step-like increase in scattering. The typical number of pulses incident on one location before damage occurred was approximately 200. Damage statistics are plotted in Fig. 4(b) with the number of test spots (N) for each sample indicated.

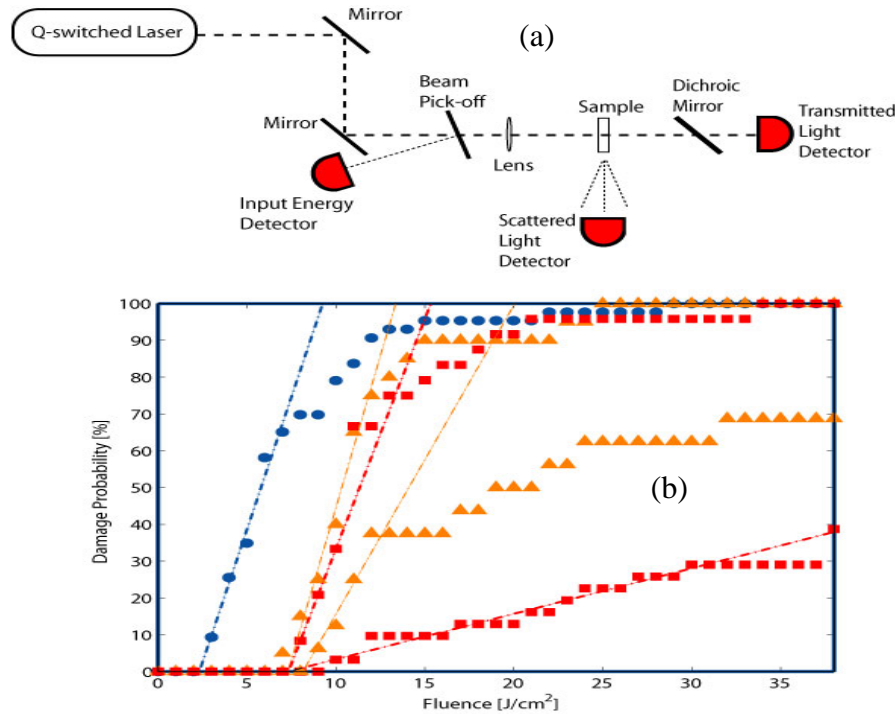


Figure 4 (a) Damage threshold measurement setup. (b) Damage probabilities for congruent lithium niobate (circles, N=43) and two samples of both CLT (triangles, N=20,16) and SLT (squares, N=31,24).

Measured damage fluence thresholds for congruent lithium niobate, CLT and SLT are $2.3\text{ J}/\text{cm}^2$, $7.3\text{ J}/\text{cm}^2$ and $7.3\text{ J}/\text{cm}^2$, respectively. The damage threshold was measured by extrapolating the Weibull distribution back to zero probability. For all congruent lithium niobate samples, surface damage was the predominant damage mechanism, however, all

CLT and SLT samples damaged in the bulk before the surface. The CLT and SLT samples were all taken from different substrates. It is interesting to note that the two samples of CLT and SLT had widely different defect densities, and some volumes of LT did not damage at even the highest input energies. This suggests that both the defect itself and the concentration of bulk damaging defects in LT are determined by the growth of the original LT substrates.

From these measurements, we expect 50% conversion efficiency for a 1-ns pulse in a 600-micron-thick sample at energies that are 33% of the damage fluence. We estimate that a 10 J, 1-ns pulse of 532-nm radiation is possible using the full area of a 2-inch wafer.

Our earlier work indicated that 42-degree-rotated, Y-cut substrates of SLT could be periodically poled and used for generation of 532-nm radiation through frequency doubling. We continued in this vein by working with 25-degree-rotated, X-cut substrates that could be operated at Brewster's angle. These substrates allowed the incident fundamental wave to be nearly fully polarized along the z-axis.

Periodic poling of 25-degree-rotated, X-cut samples was carried out using aluminum electrodes at 130°C. Our poling results showed that for first order periodic poling with an 8 μm poling period, 532-nm generation through SHG was possible. Domain quality as viewed from the side is shown in Fig. 5.

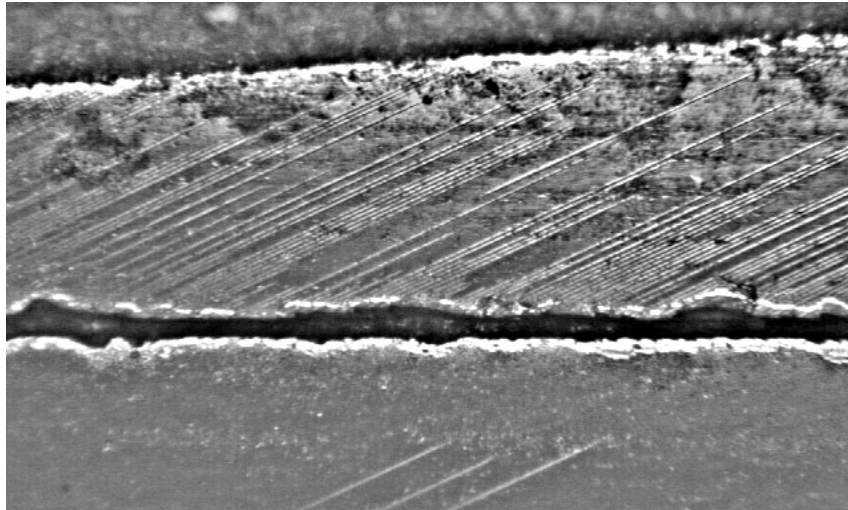


Figure 5 Side-view of 8 micron domains in a 25-degree-rotated, X-cut sample of SLT

This sample was used to frequency double a 12-ns-pulsewidth, diffraction-limited, 2.4-mJ, 10 Hz, multi-axial mode, single-transverse mode, 1064-nm Nd:YAG laser. The pump beam was loosely focused to a 270- μm spot ($1/e^2$ -intensity radius) inside the crystal. Angle phase matching was possible and produced a maximum of 18 μJ of SHG or approximately 12% of the theoretical efficiency. The discrepancy between theoretical and experimental efficiency is consistent with the poor periodic poling illustrated in Fig. 5.

Uniformity of the SHG over a 7 mm by 7 mm area was measured and is shown in Fig. 6. The sample conversion seems quite uniform with only a small area of defects towards the edge of the device. These results show promise for power scaling in the future using 25 degree cut PPSLT as a nonlinear material.

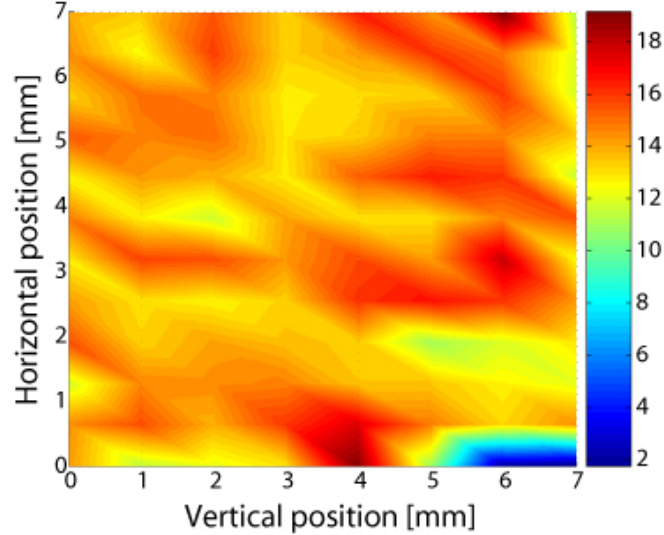


Figure 6 SHG energy in microjoules as a function of position from a 7 mm x 7 mm x 600 micron sample of periodically-poled, 25-degree-rotated, X-cut, near-stoichiometric lithium tantalate

3. Conclusions

This study clearly demonstrated that in any follow-on slab laser scaling programs, it will be important to compare the mode quality and power produced by two different types of zig-zag end-pumped slab amplifiers, one incorporating parasitic suppression design features and one not. Although we experimentally compared the performance of the two slabs with respect to their small signal gains, we did not have the opportunity to experimentally compare their respective performance under saturation. Only by characterizing the mode quality produced by the two different types of slab amplifiers, will it be possible to clearly identify the effects of the parasitic design features and determine the influence of saturating beam parameters under Gaussian conditions.

During the fourth program year, we investigated silicate bonding of dielectrically-coated YAG pieces for parasitic mode suppression studies and for the application of non-doped YAG end-pieces to a doped central section to mitigate thermal end effects. This technology, used in place of conventional thermal diffusion bonding, would significantly reduce the cost of slab fabrication. (Prior to these studies, we carried out extensive analysis of silicate bonding of fused silica pieces. Fused silica was investigated before YAG because of the easier availability of highly polished fused silica samples. The promising results led us to begin investigating the bonding of YAG pieces.) In this study, we bonded approximately 10 pairs of YAG samples. The mechanical strength was

sufficient to fracture the bulk samples before the bonded interfaces failed, but we were unable to make quantitative measurements of the reflection at the bond, bond strength (in shear or tension) or damage threshold. Ultimately, it will be necessary to carry out for YAG, an experiment similar that performed during the third program year in which 100 pairs of fused silica samples were silicate-bonded to determine what concentration, solution volume and curing temperature of the silicate bonding solution yields the best optical and mechanical performance bonds.

Periodic poling of 25-degree-rotated, X-cut, near-stoichiometric lithium tantalate has been demonstrated to hold immense potential for high-power second-harmonic conversion to the green because there would be no limits to the apertures achievable. Improved periodic poling quality should allow the demonstration of high energy SHG in a large area device. This is a potential breakthrough result that could lead to efficient single pass frequency conversion of multi-Joule high pulse energy lasers.

References

- [1] W. Wiechmann, T.J. Kane, D. Haserot, F. Adams, G. Truong, J.D. Kmetec, "20-W diode-pumped single-frequency Nd:YAG MOPA for the Laser Interferometer Gravitational Wave Observatory," CLEO 1998.
- [2] W.S. Martin and J.P. Chernoch. "Multiple internal reflection face pumped laser." U.S. Patent 3633126, 1972.
- [3] Eggleston, J.M, T.J. Kane, K. Kuhn, J. Unternahrer, R.L. Byer, "The Slab Geometry Laser - Part 1: Theory," *IEEE JQE*, Vol. **20**, pp. 289-301 (1984).
- [4] R. J. Shine, Jr., A. J. Alfrey, and R. L. Byer, "40-W CW, TEM₀₀-mode, diode-laser-pumped, Nd:YAG miniature-slab laser," *Opt. Lett.* **20**, 459 (1995).
- [5] R. J. St. Pierre, D.W. Mordaunt, H. Injeyan, J.G. Berg, R.C. Hilyard, M.E. Weber, M.G. Wickham, G. M. Harpole, "Diode-array-pumped kilowatt laser," p. 2-8, High-Power Lasers; Santanu Basu; Ed. Jun 1998, p. 2-8.
- [6] D.S. Hum, R.K. Route, K. Urbanek, R.L. Byer, M.M. Fejer, "Generation of 10.5-W CW 532-nm Radiation by SHG in Vapor-Transport-Equilibrated, Periodically-Poled, Near-Stoichiometric Lithium Tantalate", CLEO 2006.
- [7] D. Eimerl, "High Average Power Harmonic Generation", *IEEE J. Quant. Electron.*, QE-23, 575-592 (1997).
- [8] M. Peltz, U.Bäder, A. Borsutzky, R. Wallenstein, J. Hellström, H. Karlsson, V. Pasiskevicius, F. Laurell, "Optical Parametric Oscillators for high pulse energy and high average power operation based on large aperture periodically poled KTP and RTA", *Appl. Phys. B*, **73**, 663-670 (2001).
- [9] H. Ishizuki, T. Taira, S. Kurimura, J.H. Ro and M. Cha, "Periodic Poling in 3-mm-Thick MgO:LiNbO₃ Crystals". *Jpn J. Appl Phys*, **24**, L108-L110 (2003).
- [10] K. Nakamura, T. Hatanaka and H. Ito, "High Output Energy Quasi-Phase-Matched Optical Parametric Oscillators Using Diffusion-Bonded Periodically Poled and Single Domain LiNbO₃", *Jpn. J. Appl. Phys*, **40**, L337-L339 (2001).
- [11] D.S. Hum, R.K. Route, G.D. Miller and M.M. Fejer, "Quasi-phase-matched second harmonic generation using 42° rotated Y-cut near-stoichiometric lithium tantalate", CLEO 2004.

II. High Average Power Fiber MOPA System

Y. W. Lee, S. Sinha, K. E. Urbanek, M. J. F. Digonnet, R. L. Byer

1. Introduction

Under DARPA contract DAAD19-02-1-0184, we made important contributions to the field of power scaling diode-pumped Yb-doped fiber systems. In this final reporting period, we focused on developing the tools to build a reliable integrated Yb-fiber amplifier system. We tested in-line fiber tapers for efficient launching into large-mode-area (LMA) fibers, and we also tested the reliability of signal/pump combiners. These components, together with the gain fiber characterization, end-cap development and noise investigations we performed in earlier periods, will allow for the construction of a robust, inexpensive, integrated 200-W class fiber amplifier. In addition, we developed an integrated 10-W fiber amplifier system to test necessary control electronics that we developed to ensure long-term robust operation of the system. Finally, we developed a high-power 20-W diffraction-limited single-frequency green source at 532 nm by frequency doubling the high-power Yb-doped fiber MOPA output in a single pass.

2. Progress

2.1 Background

High-power single-frequency light sources are required for applications as varied as gravitational wave detection [1], advanced remote sensing [2] and resonant nonlinear frequency conversion processes [3]. Master oscillator power amplifiers (MOPA) have been shown to be a robust approach for amplifying a stable single-frequency laser seed to extremely high power levels while preserving the seed's line-width and coherence [4]. Traditionally, the amplifier of choice in master-oscillator/power-amplifiers (MOPAs) has been solid-state gain media, but recently fiber amplifiers have gained interest due to their near-quantum-limited efficiency and high mode quality.

The highest single-frequency power reported to date in a silica fiber MOPA is greater than 250 W [5]. This device used three stages of fiber amplifier amplification. Our goal was to produce 150 W of single frequency output from a single stage fiber amplifier. We planned to use this source as a test bed to characterize and improve the spatial mode quality, relative intensity noise (RIN), frequency noise, pointing stability, ASE suppression, degree of polarization, and the long-term stability of the output. Our overall objective was to demonstrate a system that can operate continuously without manual adjustment for several weeks and meets the stringent requirements of highly demanding applications such as gravitational wave detection [1].

Stimulated Brillouin scattering (SBS) is the main physical limitation in power scaling of single frequency silica fiber MOPAs. Phosphate glass offers a potential solution to this

problem because rare-earth oxides are considerably more soluble in this material than in silica. For example, Yb³⁺-doped phosphate glass fibers can be doped with up to 3.07×10^{21} Yb³⁺ ions/cm³ (~15 times as much as silica) and still exhibit no up-conversion. Since the theoretical SBS gain coefficient of phosphate glass is comparable to that of silica, [6] the maximum achievable output power of a single-frequency phosphate fiber source is expected to be ~15 times higher than in a silica fiber source with a comparable geometry. In addition, photo-darkening has recently emerged as a serious limiting factor in the long-term performance of high power silica fiber lasers and amplifiers. The study of phosphate fibers as laser hosts is therefore important because it presents the opportunity to evaluate whether this material has a higher threshold for photo-darkening than silica.

The first rare-earth-doped phosphate fiber lasers were demonstrated by Yamashita in 1989 [7]. In 2004, NP Photonics reported the first cw 1060-nm single-frequency laser emission in a 1.5-cm single-mode Yb-doped phosphate fiber, with more than 200 mW of output power and a linewidth of 3 kHz [8]. Thus far, however, the use of Yb³⁺-doped phosphate fibers for power scaling at 1 μ m has not been reported.

References

- [1] B. Barish and R. Weiss, "LIGO and the Detection of Gravitational Waves", *Physics Today*, October 1999.
- [2] S. Henderson, P. Suni, C. Hale, S. Hannon, J. Magee, D. Bruns, E. Yuen, "Coherent laser radar at 2 μ m using solid state lasers", *IEEE Trans. On Geoscience and Remote Sensing*, **31**, p. 4-15, 1993.
- [3] C. Denman, "20 Watt CW 589-nm Sodium Beacon Excitation Source for Adaptive Optical Telescope Applications", *SPRC* 2003.
- [4] W. Wiechmann, T.J. Kane, D. Haserot, F. Adams, G. Truong, J.D. Kmetec, "20-W diode-pumped single-frequency Nd:YAG MOPA for the Laser Interferometer Gravitational Wave Observatory," *CLEO* 1998.
- [5] J. Nilsson, J. Sahu, D. Soh, C. Alegria, P. Dupriez, C. Codemard, et al. "Single-frequency, polarized ytterbium-doped fiber MOPA source with 264 W output power", *CPDD1, CLEO* 2004.
- [6] D. Heiman, D. S. Hamilton, and R. W. Hellwarth, "Brillouin scattering measurements on optical glasses," *Phys. Rev. B*, **19**, p. 6583-6592, 1979
- [7] T. T. Yamashita, "Nd- and Er-doped phosphate glass for fiber laser," *Proc. of SPIE, Fiber Laser Source and Amplifiers*, **1171**, p. 291-297, 1989.
- [8] J. D. R. Myers, T. Wu, L. Chen, M. J. Myers, C. R. Hardy, and J. K. Driver, "New high power rare-earth-doped fiber laser materials and architectures," *Proc. of SPIE*, **4974**, p.177-184, 2003.

2.2 New developments in Yb⁺-silica fiber based systems

2.2.1 Progress towards an integrated 200-W Yb-silica fiber MOPA

During the course of this program, we developed a 150-W class Yb-doped silica-based fiber MOPA as illustrated below in Fig. 7.

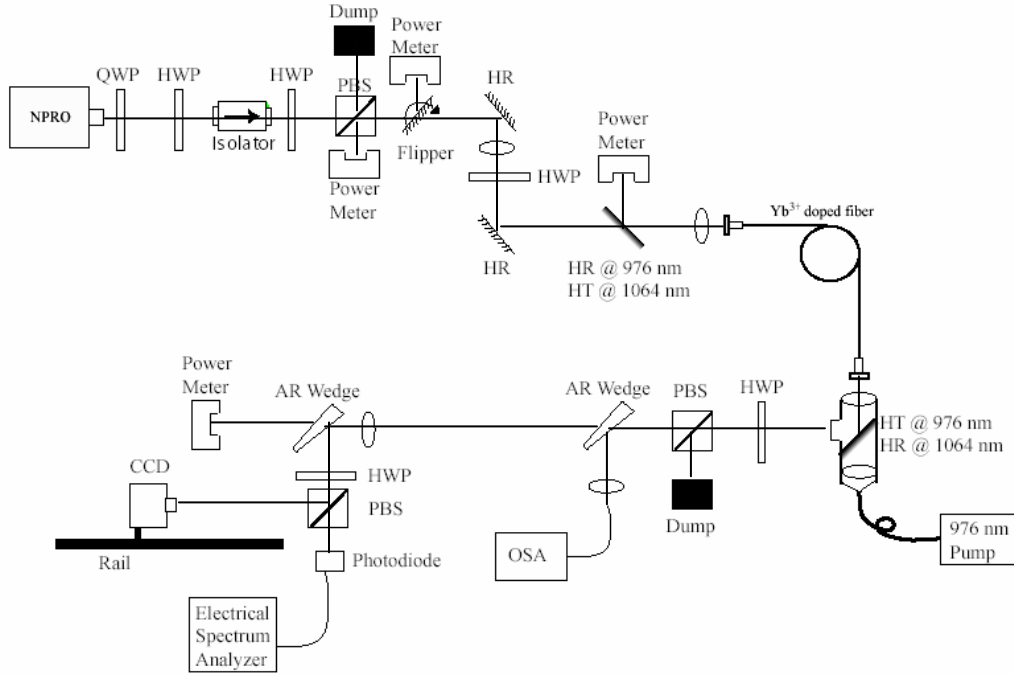


Figure 7 Experimental setup for a Yb-doped silica fiber 150-W MOPA illustrative diagnostic equipment.

This system was very useful to carefully characterize the gain fiber, in particular its nonlinear thresholds, its refractive index uniformity (as it pertains to mode quality), and its thermal properties. We characterized the output beam's mode profile with a high-finesse mode cleaner to determine its precise mode content.

Although such a system would be acceptable for laboratory demonstrations, the large number of free-space components and the system's high sensitivity to launch conditions at the input to the active LMA fiber would significantly degrade its manufacturability and long-term reliability. To that end, we invested a considerable amount of research design towards integrating the fiber amplifier system in order to enhance the overall system reliability and decrease the cost of ownership of the source. Such an integrated source could look similar to the schematic shown in Fig. 8 which we included in the previous year's report.

approached several vendors to develop a solution. The taper from the standard 6- μm fiber mode size to the LMA fiber size is accomplished in two steps. First, the output of the pre-amplifier is launched into a fiber-pigtailed isolator. The isolator, which also has a spectral filter to minimize the amount of launched ASE into the power amplifier, has a set of aspheric lenses to couple the light from the 6- μm input fiber to a 13- μm polarization-maintaining (PM) single-clad output fiber. This fiber is then straightforwardly spliced to a double-clad fiber of the same mode field diameter and cladding size. This 13- μm double-clad fiber is then tapered in the pump combiner module to a 25- μm MFD in a passive double-clad fiber at the output with a 250- μm glass inner cladding. This pump combiner module is a tapered fiber bundle (TFB) that combines the pump power output from 12 separate 100- μm fiber-coupled 976-nm-wavelength pump diodes. Each of the 12 arms of the device can handle 30 W of input power so that over 300 W of pump power can be launched into the gain fiber. This 25/250 passive fiber at the output would then be spliced to a 25/250 active fiber. According to our simulations, one should be able to achieve over 250 W of output power from such a source using commercial Liekki active fiber before the onset of stimulated Brillouin scattering. A second pump combiner (as shown above in Fig. 2), would not be needed and the output end of the fiber would be end-capped with a silicate bonded flat. This flat could then be easily mounted in a standard opto-mechanical stage to achieve the required mechanical stability.

The fiber-pigtailed isolator is manufactured by one vendor and the pump combiner module is made by a second vendor. We sought to determine the reliability of the two devices. Our tests of some prototypes showed that the pigtailed isolator that transforms the 6- μm fiber to the 13- μm fiber, in addition to providing spectral filtering, can have losses as low as 2.2 dB with a polarization extinction ratio exceeding 30 dB. We also carefully tested the pump combiner module. The polarization extinction ratio (PER) of the module was excellent (greater than 26 dB). The mode quality was also very good, as shown below in Figure 9 on the following page.

The M^2 was measured to be 1.08 and 1.10 in the two axes and the beam did not jitter and the profile did not distort over time, provided the fiber was not bent excessively (a bend radius of 2" or larger seemed to be required). We verified with a single 100- μm fiber-

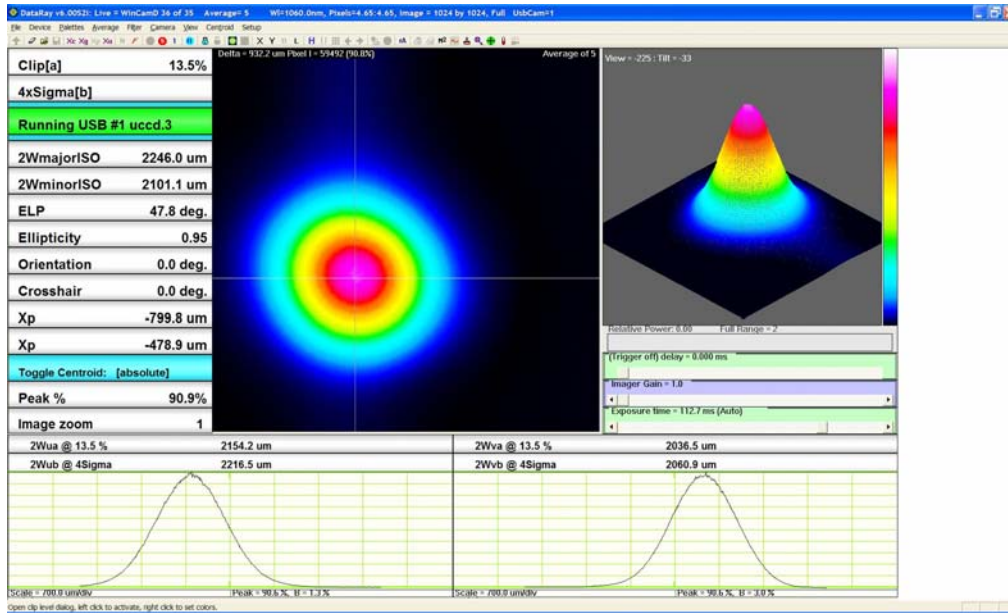


Figure 9 Output mode from signal pump combiner with 25/250 fiber.

coupled laser diode that the module was able to withstand more than 35 W in a single arm. Unfortunately, we did not have more 100- μm fiber-coupled laser diodes to test the module with a higher total amount of pump power. The final test we undertook was to splice the output of the combiner to the Liekki gain fiber. This splice was not trivial and it required the core-cladding concentricity of the Liekki fiber to be very small. However, once we obtained a fiber sample with a suitable small concentricity, the output mode from the fiber was very good and very repeatable. The mode profile is shown in Fig. 10.

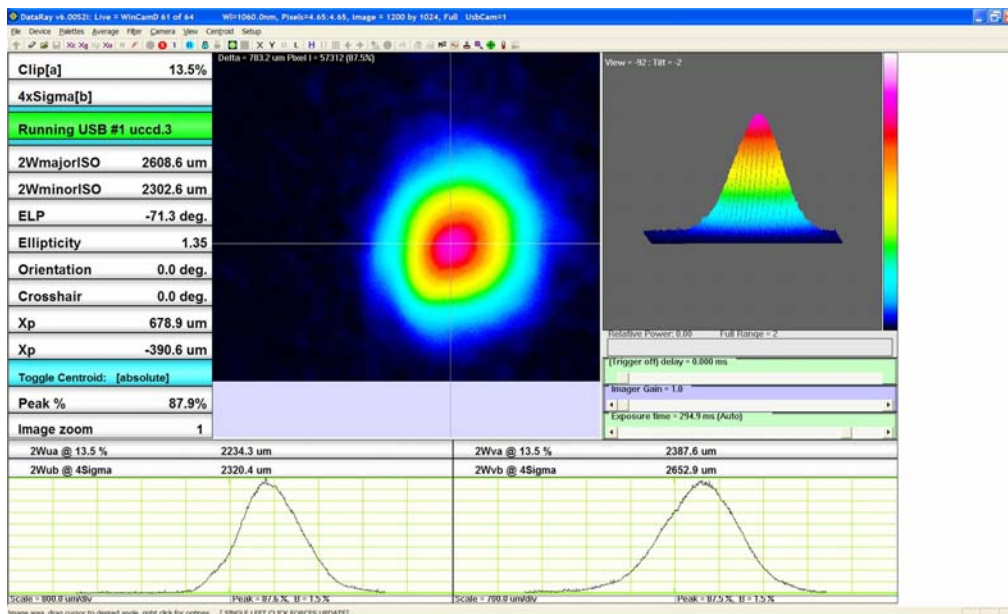


Figure 10 Mode profile out of the 25/250 gain fiber. The distortions near the edges of the beam are due to the small amount of light coupled into the cladding after the splice.

The M^2 was measured to be 1.10 and 1.09 in the two axes, indicating a negligible deterioration in beam quality after the splice.

In summary, we believe that this system could be straightforwardly assembled and the total cost of parts (including seed) could be less than \$20,000.

References

- [1] R. W. P. Drever, J. L. Hall, F. V. Kowalski, J. Hough, G. M. Ford, A. J. Munley and H. Ward, "Laser phase and frequency stabilization using an optical resonator," Appl. Phys. B, **31**, p. 97-105 (1983).

2.2.2 20-W class integrated Yb-doped silica fiber MOPA

In the previous report, we reported on our efforts to develop a 20-W class integrated fiber MOPA using non-LMA Yb-doped silica fiber that uses only convective cooling. We had several objectives in constructing this system. First, we wanted to test several components in a functioning system to determine their reliability. These included a low-power TFB and the silicate bonded flat at the output. A second objective was to develop control electronics to allow for reliable operation of a high-gain fiber MOPA. The third objective was to develop a medium power source to test amplification in high-power bulk Nd:YAG crystalline media.

We developed and tested a 10W fiber MOPA system, using a 6- μ m core, Yb-doped silica PM fiber (LIEKKI Yb1200-DC-PM) as the amplifying medium, as illustrated in Fig. 11 below. We found the optimal fiber length to be 3.7m. At this length, we observed nearly 10W of diffraction limited output, a PER of 23dB, and RIN below 1% above 1Hz, shown in Figs. 12 and 13 on the following pages.

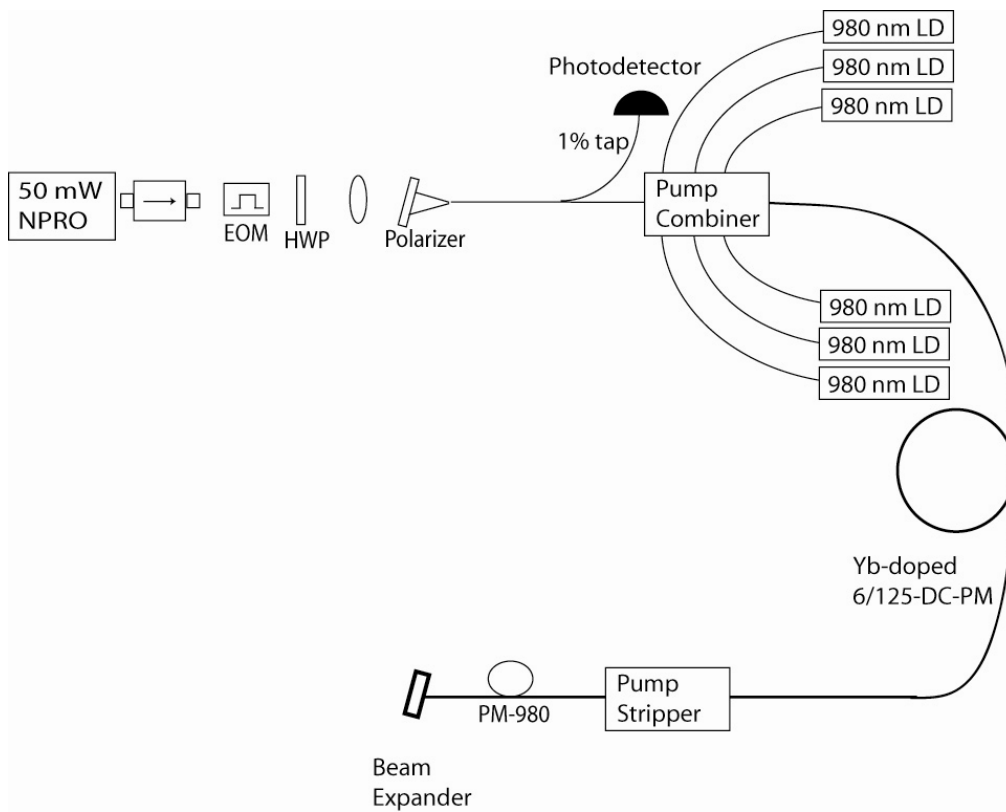


Figure 11 Experimental setup for 10-W fiber amplifier

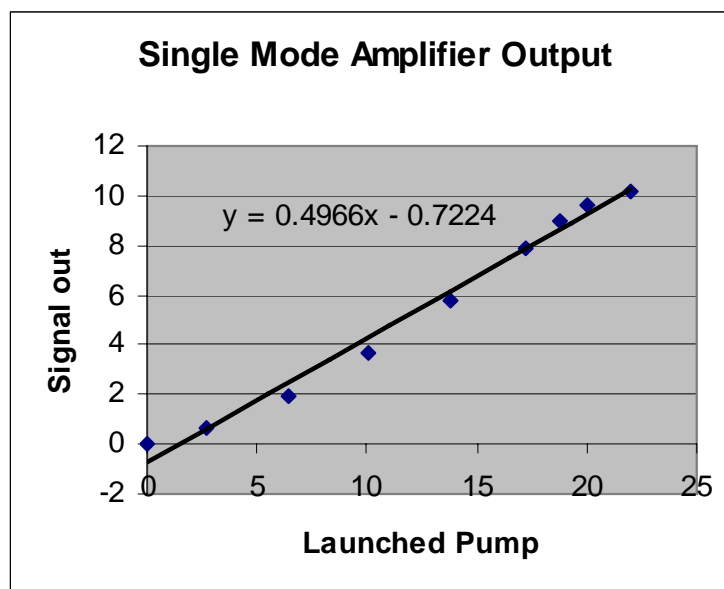


Figure 12 Slope efficiency of our 10 fiber MOPA

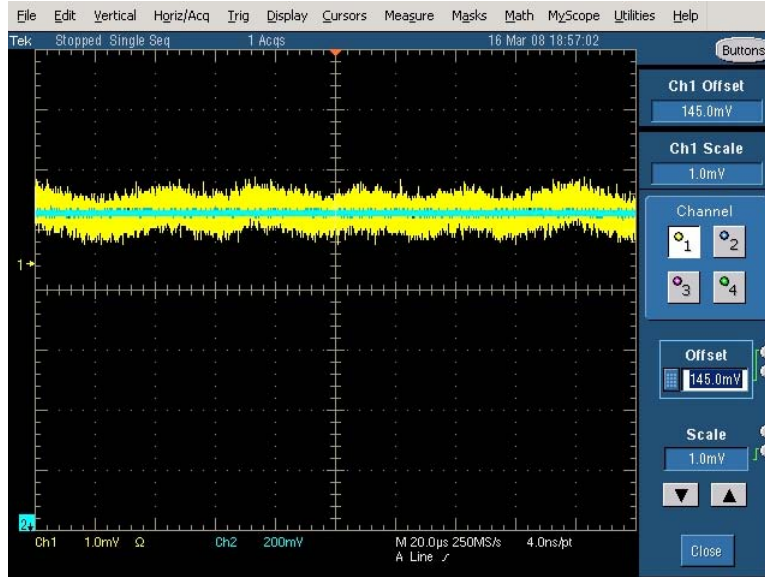


Figure 13 RIN measurement. Blue line is in the near field, yellow line is after a Faraday isolator, containing two thin film polarizers

We used the Pound-Drever-Hall technique to lock the output of the laser to a reference cavity for purposes of characterization. Any beam pointing instability as well as phase noise shows up as amplitude noise past the reference cavity. This is also a good indicator of mode quality. When locked, the cavity (finesse of 50) scrapes off all of the higher order modes. Figure 14 shows that 97% of the incident light could be resonantly coupled into the cavity as the laser frequency was scanned through the resonant frequency of the cavity. Thus, at least 97% of the output from the fiber was shown to be in a diffraction-limited TEM_{00} mode.

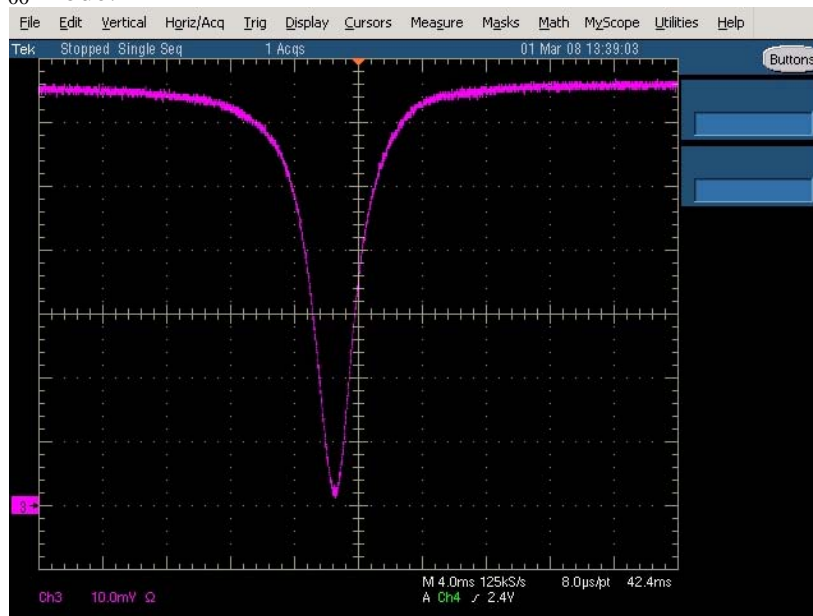


Figure 14 Incident light coupled into a high-Q cavity as the frequency of the fiber source was swept through the cavity resonance.

In addition to testing of individual components, we developed control electronics to prevent damage to the system. In particular, we added circuitry to shut down the pump diodes in case the seed shuts down or the feedback to the amplifier exceeds a certain threshold value. The shutting-off of the diodes needs to be done very quickly in order to prevent damage. For the case in which the seed turns off abruptly, or even degrades below a certain level, it is important that the pump diodes be shut down within microseconds to prevent the gain fiber from passively Q-switching and damaging the gain fiber or the pump diodes. We developed circuitry to shut down the diodes within 6 microseconds, and we experimentally verified that this was sufficiently fast enough to prevent damage to the fiber.

It will remain to future programs to demonstrate a medium power, 30-W of amplification system by adding a second stage of amplification. Such a 30 W of power would be realized by using strictly single-mode fiber (instead of few-moded LMA fiber).

2.2.3 Room-temperature stable generation of 19 Watts of single-frequency 532-nm radiation in a periodically poled lithium tantalate crystal

This section describes a system that produces 19 W of diffraction-limited radiation at 532 nm through single-pass frequency doubling of the output of a 1064-nm Yb³⁺-doped fiber MOPA in a periodically-poled, near-stoichiometric lithium tantalate (PPSLT) crystal. The output of the system was stable at the 19-W level for over one hour with no signs of photo-refraction. The green power is believed to be limited by infrared-induced thermal de-phasing in the PPSLT crystal.

High-power visible light generation with good spatial beam quality is required in applications ranging from astronomy [1] to medicine [2] to laser displays [3]. Efficient direct generation of diffraction-limited visible light is difficult due to the absence of appropriate lasing materials. Nonlinear frequency conversion of infrared solid-state sources has successfully produced multiple watts of power in the blue [4], green [5], and yellow [6]. In recent years, the development of double-clad large-mode-area fibers has enabled the realization of 100-W-class diffraction-limited infrared sources with optical efficiencies well above 50% [7]. These sources allow for the possibility of high-power 10-W-class visible sources possessing excellent beam quality with overall optical efficiencies well over 10%.

However, high-damage threshold nonlinear optical crystals that use birefringent phase-matching (such as LBO) require peak powers in the IR of several kilowatts for efficient single-pass frequency conversion [5]. External resonant frequency doublers can increase the second harmonic generation (SHG) efficiency of continuous-wave (cw) or low-peak-power pulsed sources in birefringently phase-matched crystals at the expense of considerable system complexity [8]. Intracavity SHG is not suitable for the master-oscillator-power-amplifier (MOPA) architecture, which is most commonly used for high-power single-frequency systems.

Quasi-phase-matched (QPM) nonlinear materials offer considerably higher conversion efficiencies than available birefringently phase-matched media. Periodically poled lithium niobate is widely used due to its high nonlinearity and its wide availability. However, the congruent composition that is commonly available for ferroelectrics (such as lithium niobate and lithium tantalate) suffers from photorefractive damage (PRD) at even moderate levels of visible light [9].

In the past decade, considerable effort has been expended by several research groups on the development of ferroelectrics that have a near-stoichiometric composition, since stoichiometric crystals have lower defect densities [10]. The lower defect density increases the resistance of these materials to PRD and photo-chromic effects, such as green-induced infrared absorption (GRIIRA) [11].

The nonlinearities of these stoichiometric ferroelectrics are ideally suited for the 100-W and kW range powers that have now become available from fiber laser systems. The development of these stoichiometric nonlinear materials coupled with efficient fiber laser systems has led to the demonstration of efficient narrow-linewidth, watt-class sources in the green and yellow [12,13]. We describe in this section a system that generates 18.8 W of cw diffraction-limited power at 532 nm in a single longitudinal mode through frequency doubling the output of a Yb^{3+} -doped fiber MOPA in a periodically poled near-stoichiometric lithium tantalate (PPSLT) chip. To the best of our knowledge, this power represents the highest diffraction-limited power in the green (cw or average) that has been generated in a periodically poled material. It is also the highest cw power generated through nonlinear frequency conversion to the green in a single-pass configuration (QPM or birefringently phase matched).

The experimental setup is shown in Fig. 15. The fiber amplifier shown below is the same as that illustrated in Fig. 7.

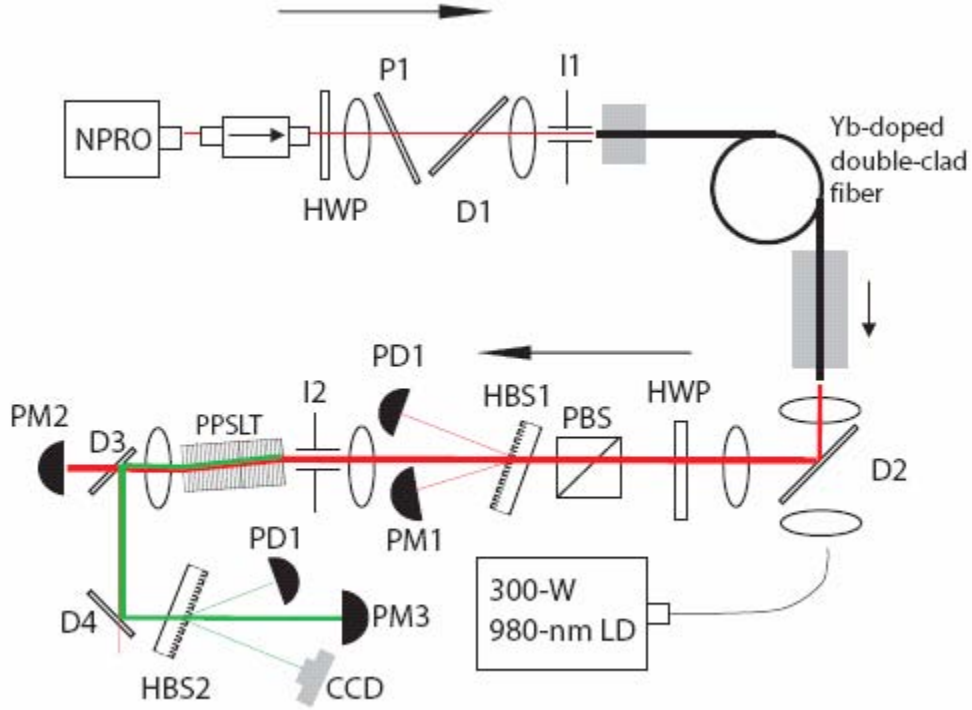


Figure 15 Experimental setup for high-power green generation. NPRO: non-planar ring oscillator; HWP: half-waveplate; P1: pickoff to measure onset of SBS; D1: 980 nm/1064 nm-dichroic that reflects 980 nm; D2: 980 nm/1064 nm dichroic that reflects 1064 nm; D3, D4: 532 nm/1064 nm dichroics that reflect 532 nm; I1, I2: high-power irises; PBS: polarizing beamsplitter; PD1, PD2: photodetectors; PM1, PM2, PM3: thermal power meters; HBS1: 1064 nm holographic beam sampler; HBS2: 532-nm holographic beam sampler; LD: laser diode; CCD: charge-coupled-device camera. The paths of the 1064-nm and 532-nm beams are shown. The 980-nm laser diode light path is omitted for clarity.

To frequency double the 1064-nm light, a 4-cm-long, 1-mm-thick PPSLT chip was used. Near-stoichiometry was achieved by taking the originally congruent-composition unpoled wafer and subjecting it to the vapor-transport-equilibration (VTE) process. After the VTE process, we periodically poled the chip. The details of the crystal fabrication and periodic poling processes have been reported in the literature by Hum et al [10]. A low-temperature broadband anti-reflection (AR) coating with a center wavelength of approximately 800 nm was applied to both ends of the chip to maximize the generated green power. The PPSLT chip was placed in a home-made mount whose temperature was controlled with a thermo-electric cooler (TEC) and monitored with a thermistor. Care was taken to ensure that the mount was uniformly heated and thermally insulated from the environment.

Although the chips were AR coated, the reflection at 1064-nm was measured to be approximately 2%. This reflection provided sufficient feedback to the amplifier to cause spiking in the 1064-nm output of the NPRO as the pump diode power was increased. This spiking damaged one of our earlier PPSLT samples. Since we did not have an isolator that could handle 100 W of incident IR power, we chose to mitigate this problem by

slightly angling the PPSLT crystal in the horizontal direction and inserting an iris to prevent the reflected light from reaching the gain fiber. We experimentally determined the minimum allowable tilt angle by monitoring the fiber amplifier output with a fast photodiode to detect the onset of spiking. Since the width of the poled regions on the chip was only about 400 μm , we had to increase the size of the waist in the crystal in the horizontal dimension to prevent the diffracting beam from sampling non-poled regions, which would result in decreased efficiency and distortions to the spatial mode of the generated green output. We focused the IR beam to waists with $1/e^2$ diameters of 80 μm and 110 μm in the horizontal and vertical dimensions, respectively.

We measured a low-power, normalized conversion efficiency of 0.3%/(W·cm) in our PPSLT chip, which is about 2.2 times lower than ideal given our focusing conditions. The discrepancy is most likely caused by a non-ideal poling duty cycle [10]. To demonstrate that these PPSLT frequency doublers could be operated near room temperature without the onset of photorefractive damage, gratings with a poling period of 8.0 μm that were designed to phase-match the 1064-nm frequency doubling process at 40°C were used. Low-temperature phase-matching has the additional advantage that the thermal conductivity of SLT is higher at lower temperatures [14], so the temperature rise is reduced for a given amount of absorbed optical power. As a result of the tilt of the chip, the peak phase-matching temperature was shifted downwards to 31.3°C. As shown in Fig. 16 on the next page, the measured low-temperature tuning curve for the 4-cm device agrees well with theoretical predictions.

We increased the power from the fiber amplifier incident on the PPSLT chip in steps and monitored the generated green power as shown in Fig. 17, also on the next page. As the 1064-nm power was increased, the controller's temperature set-point for the PPSLT chip was manually adjusted for maximum green power. The need for the adjustment is predominantly due to absorption of the incident IR in the PPSLT. We measured a maximum power of 18.3 W outside of the chip (corresponding to 18.8 W inside the chip) with a launched 1064-nm power of 75 W. This represented an overall optical efficiency of 16% with respect to incident diode pump power.

As the incident power was increased beyond 30 W, we found that the generated green power began to deviate from the theoretical \tanh^2 curve. We think that this deviation may have been due to thermal de-phasing, a process by which the phase-matching in the nonlinear medium is spoiled due to the uncompensated temperature dependence of the refractive index at the fundamental and second harmonic frequencies [15]. In the case of focused interactions in long nonlinear optical chips in which the heat is removed in an axis perpendicular to the optical axis of the beam, longitudinal temperature variations can be neglected and the thermal de-phasing can be almost completely attributed to transverse variations. For efficient conversion under high nonlinear drive, the de-phasing must be kept below $\pi/10$ [16]. The thermal conductivity of the PPSLT crystal was measured in both the z-axis and in the direction normal to it [14]. Using the geometric mean of the values measured in the two axes of 6.7 W/(m·K), and using measured values of 0.1%/cm and 0.02%/cm for the PPSLT chip's linear and green-induced absorption at 1064 nm, we can calculate the thermal de-phasing for a given incident power [17]. We determined that

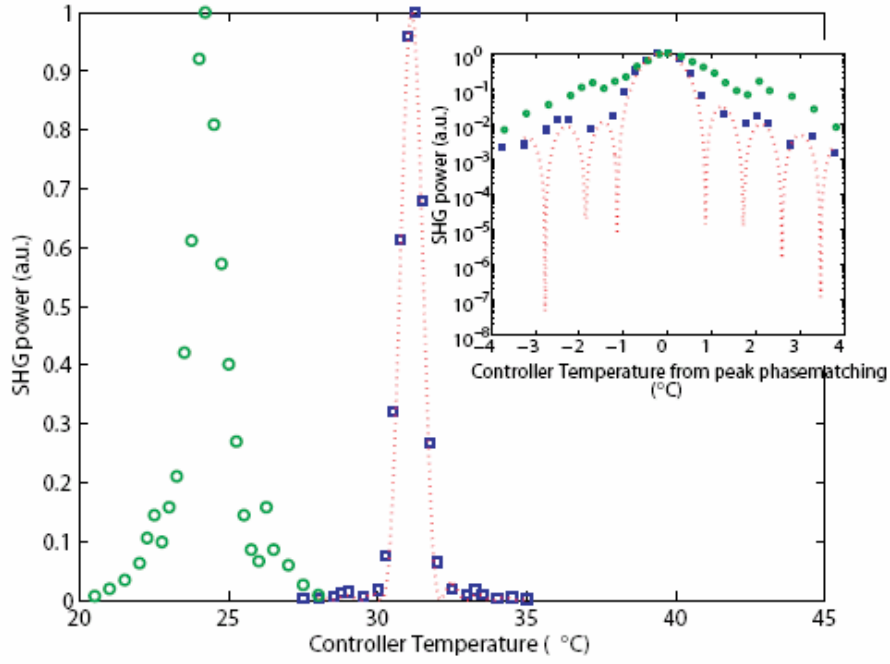


Figure 16 Temperature tuning curves for the PPSLT chip. The low-power measurements (squares) and the theoretical tuning curve assuming no absorption (dotted line) for the given focusing conditions are shown. The measured tuning curve at the 19-W level is also shown (circles). Inset: Superimposed tuning curves at low-power (squares) and high-power (circles) on a logarithmic scale. The theoretical curve (dotted line) is also shown.

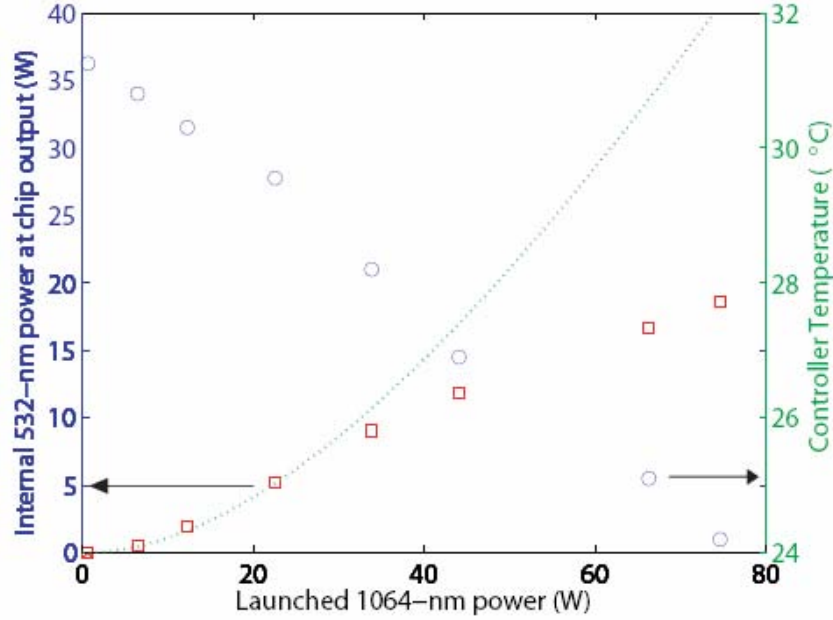


Figure 17 Internal SHG power (squares) and optimum controller set-point temperature (circle) versus internal 1064-nm power. The dotted line is the extrapolated $P \times \tanh^2$ curve from the measured low-power conversion efficiency.

given our focusing conditions and measured normalized efficiency of our 4-cm-long PPSLT chip, the thermal de-phasing reaches $\pi/10$ when the 1064-nm launched power is 35 W, which matches well the measured results shown in Fig. 17.

At the maximum green power of 18.8W, we measured the temperature tuning curve shown in Fig. 17. The broadening of the tuning curve at maximum power is clearly illustrated in the inset, in which the low-power and high-power tuning curves have been superimposed on semi-logarithmic axes.

The beam quality of the IR and green beams were each measured at both low and high powers. At low powers, the M^2 of the IR beam was found to be 1.05 and 1.03 in the horizontal and vertical dimensions, respectively. At the maximum used power of 75 W, the M^2 of the 1064-nm beam was 1.04 and 1.05 in the horizontal and vertical dimensions, respectively. At low powers, the M^2 of the 532-nm beam was 1.04 and 1.01 in the horizontal and vertical dimensions, respectively. At the maximum power of 18.8 W, the M^2 of the green had deteriorated slightly to 1.19 and 1.05 in the horizontal and vertical dimensions, respectively, probably due to thermal focusing.

We also monitored for over an hour the power fluctuations in the green beam to determine if we could observe the appearance of photorefractive or photo-chromic damage. The results, shown in Fig. 18 indicate that for over more than one hour, there

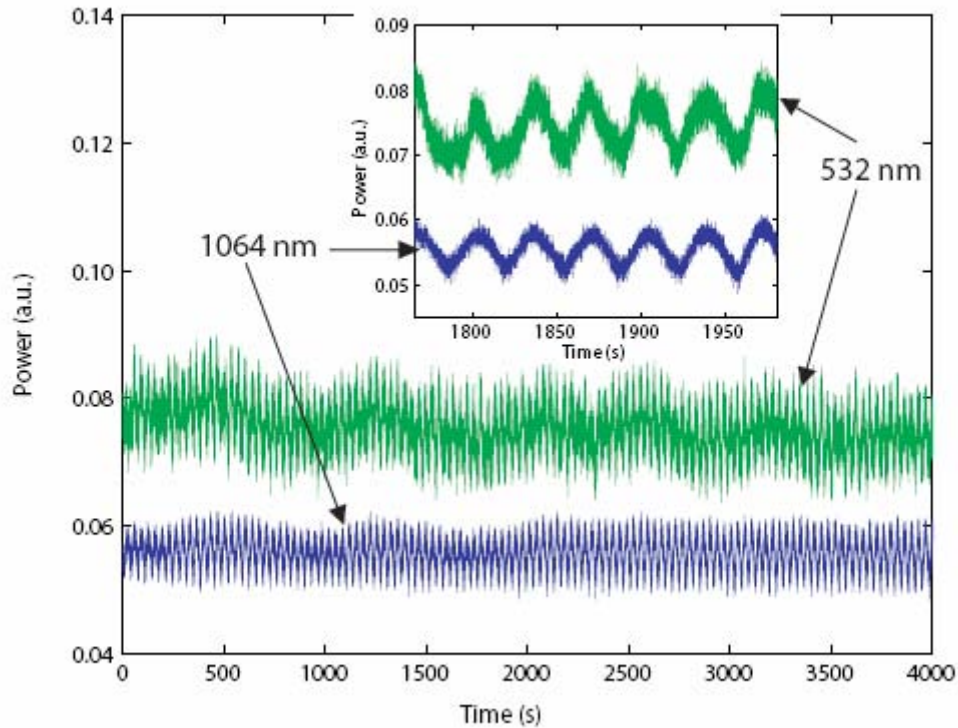


Figure 18 4000-second trace at the maximum green operating point (19 W) taken with a fast photodiode. The IR power incident on the PPSLT chip is also shown. Inset: Zoomed-in trace of the green and IR demonstrating the 35-second-period oscillations in the IR and green due to fluctuations in the pump-diode wavelength.

was no significant deterioration in the green generated output. The measured peak-to-peak fluctuations in the green power were $\pm 16\%$ over the 4000-second measurement period. Further examination of the photodiode data indicated that the fluctuations in the generated green power were due to fluctuations of the incident IR power (see inset in Fig. 13). We determined that the fluctuations in the IR power were due to a periodic wavelength drift of the stack of pump diodes. This wavelength drift had a large effect on the output power since our gain fiber was quite short and the Yb^{3+} absorption peak at 975 nm is quite narrow. The power fluctuations at both 1064 nm and 532 nm could be eliminated by using volume Bragg grating stabilized pump diodes. Further improvements in efficiency can be achieved by improving periodic poling quality and/or by reducing of thermal de-phasing effects. The latter may be achieved by using either a shorter PPSLT crystal to increase the temperature acceptance bandwidth of the chip, or with segmented ovens to thermally compensate the temperature gradients along the chip. Using the same Yb^{3+} -doped fiber amplifier, we expect to generate more than 22 W of 532-nm light using a 1.7-cm-long PPSLT crystal without further improvements in poling quality.

References

- [1] W. Happer, G. MacDonald, C. Max, and F. Dyson, "Atmospheric-turbulence compensation by resonant optical backscattering from the sodium layer in the upper atmosphere," *Journal of the Optical Society of America A: Optics and Image Science, and Vision* 11, 263–276 (1994).
- [2] N. Sadick and R. Weiss, "The utilization of a new yellow light laser (578 nm) for the treatment of Class I red telangiectasia of the lower extremities," *Dermatologic Surgery* 28, 21–25 (2002).
- [3] R. Knize, "Full color solid state laser projector system," (1994). US Patent 5,317,348.
- [4] D. Woll, B. Beier, K. Boller, R. Wallenstein, M. Hagberg, and S. O'Brien, "1 W of blue 465-nm radiation generated by frequency doubling of the output of a high-power diode laser in critically phase-matched LiB_3O_5 ," *Optics Letters* 24, 691–693 (1999).
- [5] A. Liu, M. Norsen, and R. Mead, "60-W green output by frequency doubling of a polarized Yb -doped fiber laser," *Optics Letters* 30, 67–69 (2005).
- [6] J. Bienfang, C. Denman, B. Grime, P. Hillman, G. Moore, and J. Telle, "20 W of continuous-wave sodium D2 resonance radiation from sum-frequency generation with injection-locked lasers," *Optics Letters* 28, 2219–2221 (2003).
- [7] Y. Jeong, J. Sahu, D. Payne, and J. Nilsson, "Ytterbium-doped large-core fiber laser with 1.36 kW continuous-wave output power," *Optics Express* 12, 6088–6092 (2004).
- [8] S. Yang, C. Pohalski, E. Gustafson, R. Byer, R. Feigelson, R. Raymakers, and R. Route, "6.5-W, 532-nm radiation by cw resonant external-cavity second-harmonic generation of an 18-W Nd:YAG laser in LiB_3O_5 ," *Opt. Lett.* 16, 1493–1495 (1991).
- [9] Y. Furukawa, K. Kitamura, S. Takekawa, A. Miyamoto, M. Terao, and N. Suda, "Photo-refraction in LiNbO_3 as a function of $[\text{Li}]/[\text{Nb}]$ and MgO concentrations," *Applied Physics Letters* 77, 2494 (2000).
- [10] D. Hum, R. Route, G. Miller, V. Kondilenko, A. Alexandrovski, J. Huang, K. Urbanek, R. Byer, and M. Fejer, "Optical properties and ferroelectric engineering of vapor-transport-equilibrated, near-stoichiometric lithium tantalate for frequency conversion," *Journal of Applied Physics* 101, 093108 (2007).
- [11] K. Kitamura, Y. Furukawa, S. Takekawa, M. Nakamura, A. Alexandrovski, and M. Fejer, "Optical damage and light-induced absorption in near-stoichiometric LiTaO_3 crystal," *Lasers and Electro-Optics, 2001. CLEO'01. Technical Digest. Summaries of papers presented at the Conference on pp. 255–256* (2001).
- [12] S. Tovstonog, S. Kurimura and K. Kitamura, "High power, continuous-wave green light generation by quasi-phase matching in Mg stoichiometric lithium tantalate," *Applied Physics Letters* 90, 051115 (2007).

- [13] S. Sinha, K. Urbanek, D. Hum, M. Digonnet, M. Fejer, and R. Byer, "Linearly polarized, 3.35-W narrow-linewidth, 1150-nm fiber master oscillator power amplifier for frequency doubling to the yellow," *Optics Letters* 32, 1530–1532 (2007).
- [14] D. Hum, "Frequency conversion in near-stoichiometric lithium tantalate fabricated by vapor transport equilibration," Ph.D. thesis, Stanford University (2007).
- [15] O. Louchev, N. Yu, S. Kurimura, and K. Kitamura, "Thermal inhibition of high-power second-harmonic generation in periodically poled LiNbO₃ and LiTaO₃ crystals," *Applied Physics Letters* 87, 131101 (2005).
- [16] D. Eimerl, "High average power harmonic generation," *IEEE Journal of Quantum Electronics* 23, 575–592 (1987).
- [17] P. Blau, S. Pearl, A. Englander, A. Bruner, and D. Eger, "Average power effects in periodically poled crystals," *Proceedings of SPIE* 4972, 34 (2003).

2.3 New developments in Yb³⁺-doped phosphate fiber based systems

2.3.1 Development of Yb³⁺-doped phosphate glass sources

In the prior reporting period, we developed a 20-W single-mode phosphate fiber laser as well as carried out studies on the material properties of single-mode Yb³⁺-doped phosphate fibers, including the SBS gain coefficient and photo-darkening resistance. We established that Yb³⁺-doped phosphate fibers do offer several distinct advantages over Yb³⁺-doped silica fibers when used as the gain media in high-power single-frequency single-mode laser sources. For example, the fiber length requirement for a single-frequency source is reduced by about an order of magnitude, or, conversely, an order of magnitude more power can be extracted from a phosphate fiber as compared to a silica fiber. We have also shown that phosphate fibers can be doped very highly, with as much as 12 wt.% of Yb₂O₃, while exhibiting no measurable photo-darkening. These exceptional characteristics offer the potential of single-frequency fiber amplifiers in the kW range in a step-index single-mode fiber instead of an LMA fiber, which would produce much cleaner and less noisy output beams.

In this final technical report of our program, we document our most recent progress in modeling and testing high-power single-mode single-frequency phosphate fiber amplifiers. We describe in particular a 16-W phosphate fiber amplifier doped with one of the highest published concentrations for a Yb³⁺-doped fiber (12 wt.% Yb₂O₃) and only 74.5 cm in length. This is the first report of a watt-class Yb³⁺-doped phosphate fiber MOPA. We also describe power scaling to nearly 60 W in a 71.6-cm Yb³⁺-doped phosphate fiber laser (not single-frequency). Thermal-loading calculations predict that with standard cooling, this type of fiber device should be capable of producing up to 700 W of single-frequency power in a step-index, single-mode core, and considerably more in a multimode LMA (large mode area) fiber.

2.3.1.1 Material properties of Yb³⁺-doped phosphate fibers

The preforms used to fabricate the fibers tested in this work (alkaline-earth phosphate glasses) were all made by NP Photonics in a close collaboration with the characterization and device research studies at Stanford. The glass was composed of more than 50 mol% P₂O₅, as well as Al₂O₃, BaO, ZnO and La₂O₃. Al₂O₃ (~5 mol%) was added to ensure high mechanical strength and good chemical durability of the glass. Alkali ions and transition metals such as Fe and Cu were eliminated to further enhance the glass properties.

The upper-state lifetime of the Yb^{3+} ions in 12 wt.% Yb^{3+} -doped bulk phosphate glass was measured to be 1.2 ms, which is longer than in highly doped silica glass host (~ 0.8 ms) due to the presence of germanium in the latter [1]. The measured fluorescence relaxation curve showed a single exponential, thus demonstrating negligible concentration quenching in spite of the extremely high Yb^{3+} concentration. The same phosphate glass host doped up to 26 wt% of Yb_2O_3 (~ 15 times as much as is possible in silica without inducing quenching) still does not exhibit noticeable concentration quenching, up-conversion, or crystallization [2].

For the purposes of evaluating high-power phosphate fiber laser sources, two types of double-clad phosphate fibers were tested, a standard one with a circular inner cladding and a fiber with a slightly eccentric core and a small air-hole some distance from it. This second fiber was designed to provide mode mixing (the role of the air hole) and improved spatial overlap between the pump modes and the doped core (the reason for the eccentricity of the core). These two effects increased the pump absorption in the doped core. Both fibers had only two claddings and wereunjacketed. The outer cladding was made of phosphate glass and had thermal properties superior to the polymers widely used as outer cladding in double-clad silica fibers. A photograph of the cleaved ends of each of these fibers is shown in Fig. 19

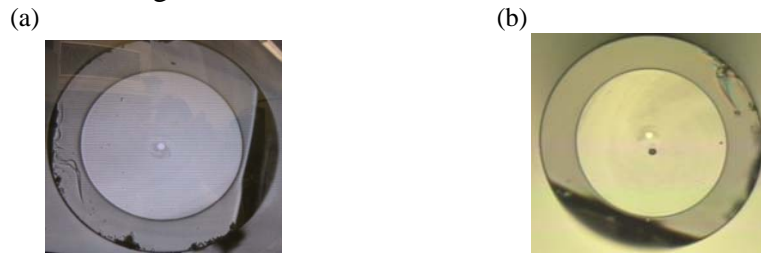


Figure 19 Photograph of the cleaved end face of the two types of double-clad phosphate fibers used in this work: (a) with a concentric core, and (b) with an offset core and adjacent air hole to mix the pump modes.

The preforms used to draw these fibers were manufactured at NP Photonics by the rod-in-tube technique. This well-developed technology is commonly used for producing soft-glass fibers [3] and silica-based fibers with compound-glass core compositions [4]. The main reason is that some of the chemicals required to fabricate a phosphate fiber by a chemical-vapor deposition procedure cannot be volatilized. A core glass rod and two cladding tubes were fabricated and assembled to form the fiber preform. The core rod was cored out of a larger bulk sample with a diamond-embedded core drill, and the barrel of the rod was polished. Both the inside and outside surfaces of the glass tubes for the inner and outer claddings were polished to a high surface quality. The inside diameter of the inner cladding tube was matched to the diameter of the core rod, and the inside diameter of the outer-cladding tube matched to the outer diameter of the inner-cladding tube. Both core and cladding glasses were carefully prepared to ensure that their chemical and thermo-mechanical characteristics were compatible, especially their softening temperature and thermal expansion coefficient. The fiber was drawn in a special furnace optimized for soft non-silica glasses, at a temperature of approximately 765°C . The

drawing process for both double-clad fibers was identical, except that a slightly positive pressure was applied to keep the air hole in the air-hole fiber from collapsing due to surface tension.

2.3.1.2 Theoretical predictions of Yb³⁺-doped phosphate fiber amplifier

Modeling phosphate fiber laser sources

To predict the quantitative performance of Yb³⁺-doped fiber lasers and amplifiers based on phosphate and other hosts, and optimize their physical parameters, we have developed a simulation code based on the original work of Wagener *et al.* [5]. This simulator solves the coupled laser rate equations numerically to predict the output performance of the fiber source, such as the amount of pump power and the length of fiber required to achieve a certain output power level, the population inversion at every point along the fiber, the forward and backward amplified spontaneous emission (ASE) powers and spectra, the gain spectrum, excess noise, etc., in either a core-pumped or a cladding-pumped configuration. The input parameters include the fiber structure and all the relevant spectroscopic parameters, such as the ion concentration, absorption and emission cross-section spectra, and excited-state lifetime. Comparison of the code prediction to the measured properties of Er³⁺-doped super-fluorescent fiber sources [6] and high-power Yb³⁺-doped silica and phosphate fiber lasers [7, 8] has shown that this code is quite accurate.

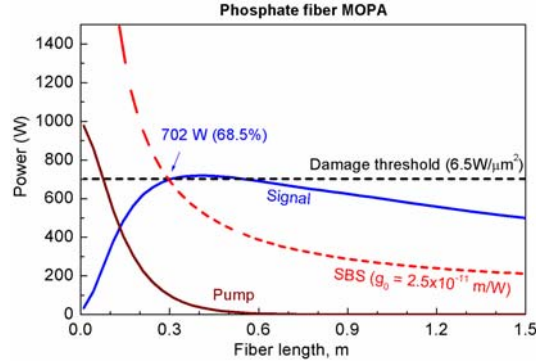
700-W true single-mode phosphate fiber MOPA

To evaluate the maximum output power that can be expected from a single-frequency, truly single-mode phosphate fiber laser or amplifier before the onset of SBS, we used our code to compare the predicted performance of two fiber master-oscillator power amplifiers (MOPAs), one made with a phosphate fiber and the other one with a silica fiber. For fair comparison, the two amplifiers had exactly the same fiber characteristics, and they were seeded and pumped exactly the same way. Both fibers were taken to have a step-index core diameter of 10 μm , a core NA of 0.07, and an inner-cladding diameter of 125 μm . The calculated effective core area was 108 μm^2 . To reflect actual differences between the two types of fibers, namely their propagation loss, upper-state lifetime, and Yb³⁺ concentration, each of these three parameters was given its actual measured value for each fiber. For the silica fiber, we used the best current values reported for commercial fibers, i.e., a loss of 0.03 dB/m, an upper-state lifetime of 0.85 ms, and a concentration of 1.2×10^{20} Yb³⁺/cm³ [9]. The corresponding values for the phosphate fiber were 3 dB/m, 1.2 ms, and 14.2×10^{20} Yb³⁺/cm³, respectively. The fiber length was a free parameter. Each amplifier was seeded with 15 W of single-frequency laser light at 1064 nm and cladding-pumped of 700 W in the forward direction and 300 W in the opposite direction, both at 975 nm. The pump powers were selected such that at the optimum length the output power just reaches the damage threshold power. This imbalanced bidirectional pumping was arranged to maintain an even thermal distribution. The simulator used the actual measured absorption and emission cross-section spectra of these two fibers as input.

Figures 20a and 20b show the theoretical prediction of the output power versus fiber length for the phosphate and silica fiber MOPAs (blue solid-curves), respectively. These

curves were plotted for a total launched pump power of 1000 W, chosen so that the output power of the phosphate fiber MOPA is as high as possible. The maroon solid-curves show the residual unabsorbed pump power. The red dashed-curves represent the SBS threshold power, assuming the conventional SBS gain coefficient of 5×10^{-11} m/W for the silica fiber, and the measured value of 2.5×10^{-11} m/W for our phosphate fiber [10].

(a)



(b)

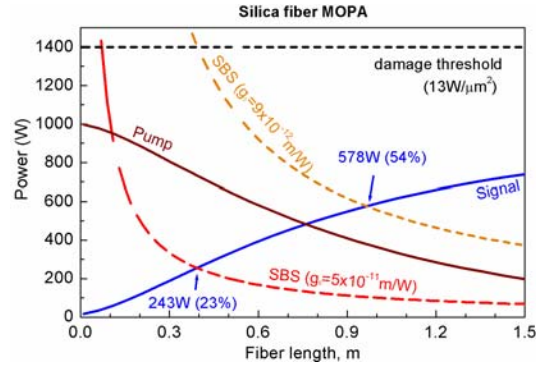


Figure 20 Theoretical predictions of the single-frequency output power dependence on fiber length for (a) a phosphate fiber MOPA and (b) a silica fiber MOPA. The blue and maroon solid-curves show the output signal and unabsorbed pump power as a function of the fiber length, respectively. The red, orange and black dashed-curves trace the SBS and damage power thresholds, respectively.

Figure 20 also shows the damage limitation for each fiber. The damage threshold for the silica fiber is 1.3 GW/cm^2 for the silica fiber [11]. Because of the lack of experimental data, the damage threshold of phosphate fibers was taken to be 0.65 GW/cm^2 , estimated conservatively by considering the bonding strength of P-O compared to Si-O and the measured damage threshold of Nd-doped phosphate glasses [12].

Figure 20a shows that as the length of the phosphate fiber is increased, the output power first increases, then decreases, as a result of the fairly high fiber loss. The figure predicts that at its optimum length (~ 30 cm), the phosphate fiber MOPA will produce 702 W of single-frequency output power without suffering from SBS. This value is in fact limited not by SBS but by surface damage. Figure 14b shows that at the same pump power level, the silica fiber MOPA produces a maximum output power of only 243 W, limited this time by the onset of SBS. Note also that at the optimum length, most of the pump power (81%) is absorbed in the phosphate fiber MOPA, so its conversion efficiency is very high

(68.5%). In contrast, in the optimized silica fiber amplifier only ~26% of the pump is absorbed, and the efficiency is consequently much lower (23%).

The reason for this difference in absorption is that the unsaturated pump absorption coefficient in the cladding of the phosphate fiber is 58 dB/m. Therefore most of the pump power is absorbed in this 30-cm phosphate fiber, and the amplifier has a high efficiency. In contrast, the corresponding absorption coefficient for the silica fiber is only 4.1 dB/m. Furthermore, the silica fiber cannot be any longer than 40 cm before the onset of SBS. Therefore, and as can be seen in Fig. 20b, these two limitations result in a pump absorption efficiency of only 26% in the 40-cm silica fiber, which explains its much lower output power.

It has been shown that the SBS gain coefficient of an LMA silica fiber can be reduced to $\sim 9 \times 10^{-12}$ m/W, i.e., a factor of 5.5, by designing the fiber such that the core acts as an anti-acoustic guiding region, which forces the acoustic-mode energy to be located away from the core [13]. Since this reduction greatly improves the maximum power that can be extracted from a single-frequency silica fiber MOPA, it was interesting to repeat this comparison assuming that the silica fiber exhibits this reduced SBS gain coefficient. The resulting SBS threshold power curve is shown in Fig. 20b as the top orange dashed-curve for the acoustic anti-guiding silica fiber. The silica fiber MOPA produces a maximum power of 578 W with 54% conversion efficiency before the onset of SBS. This is still 20% lower than the output power of the phosphate fiber (702 W). The efficiency of the phosphate fiber MOPA is also ~15% higher. This advantage of phosphate fibers would be further enhanced if the fiber loss were to be reduced to the current bulk-loss value of 0.43 dB/m [14] (same maximum output power, but with efficiency increased to 83%). Note also that the damage threshold intensity assumed for the phosphate fiber (0.65 GW/cm^2) is a conservative value, or could be increased by placing a coreless fiber end-cap or silica window at the output of the phosphate fiber [15]. The maximum output power of a single-mode phosphate fiber could then be further increased by applying the anti-acoustic guiding principle to phosphate fibers, although its applicability to a phosphate-glass fiber made by the rod-in-tube technique needs to be demonstrated.

The origin of this expected superior performance of a truly single-mode phosphate fiber MOPA is, again, that (1) the phosphate fiber can be much more heavily doped with Yb^{3+} (~15 times), hence it is shorter, and (2) it has a lower SBS gain coefficient. The downside of this increased efficiency, however, is increased thermal loading in the phosphate fiber, which leads to a higher fiber temperature. As discussed in subsequent sections, this problem is quite manageable.

2.3.1.3 Demonstration of high-power single-mode fiber amplifier and laser

16-W single-frequency phosphate fiber amplifier

The experimental setup for the Yb^{3+} -doped phosphate fiber MOPA is shown in Fig. 21. The gain medium was a 74.5-cm length of single-mode double-clad phosphate fiber. The fiber, of the type shown in Fig. 19a, had a 355- μm outer cladding, a 240- μm inner cladding with a NA of 0.445, and a 10- μm core diameter with a NA of 0.07. The core diameter and NA were designed to carry only the fundamental mode at wavelengths

above 914 nm. The fiber core was uniformly doped with $1.42 \times 10^{21} \text{ Yb}^{3+}/\text{cm}^3$ (~12 wt.% Yb_2O_3). Both fiber ends were polished at an 8° angle to prevent lasing. A counter-propagating geometry was chosen to maximize the amplifier output power. The fiber was pumped with a 972-nm fiber-coupled laser diode through a dichroic beam splitter placed on the signal output side. The fiber core was seeded with 31.6 mW of 1029.5-nm power from a commercial fiber laser with a full-width at half-maximum (FWHM) linewidth of <30 kHz. Both fiber ends were clamped in aluminum mounts. The pump-end mount was 10-inch long and water-cooled to drain heat from the fiber end region and prevent optical damage. The signal-end mount was served to passively drain heat from the end regions of the fiber. The reason for this asymmetry is that the thermal loading was much higher at the pump-end than at the signal-end. The portion of fiber between the two mounts was also cooled by conduction by cementing it to a metal plate with a thin layer of UV glue to ensure good mechanical contact.

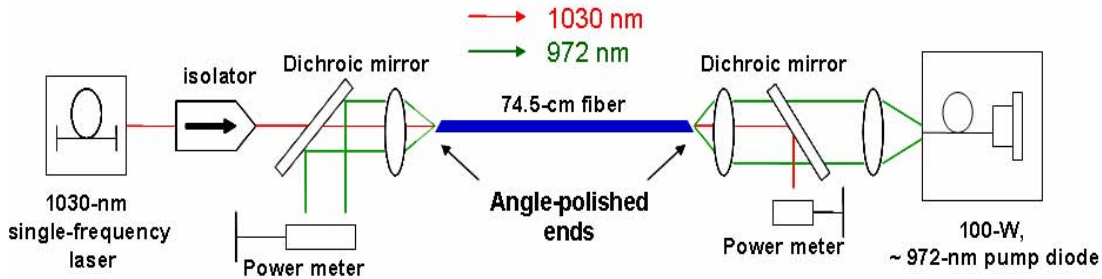


Figure 21 Experimental Yb^{3+} -doped phosphate fiber amplifier

The measured output performance of this fiber MOPA is shown in Fig. 22. A maximum output power of 16.3 W, corresponding to a gain of 27 dB with respect to the launched signal power, was reached at an absorbed pump power of 28.1 W (76 W launched). To the best of our knowledge, this is the first report of a watt-level Yb^{3+} -doped phosphate fiber MOPA. The maximum output power was limited by the available pump power.

The solid curve in Fig. 22 was generated using the aforementioned numerical simulator and the measured fiber parameter values. The spatial overlap between the pump intensity distribution in the inner cladding and the dopant in the core has a strong influence on the rate of pump absorption along the fiber. Since this overlap is not known, we used it as a free fitting parameter to best match our code prediction to the experimental data points. The best-fit solid curve in Fig. 22 was obtained with a spatial overlap of 29.5%. (An overlap of 100% would correspond to a pump distribution that is uniform across the core and inner cladding.) The theoretical curve agrees very well with the measured data. The slightly higher measured efficiency at higher pump powers is simply the result of the pump wavelength being red-shifted towards the 975-nm Yb^{3+} absorption peak at higher diode drive currents.

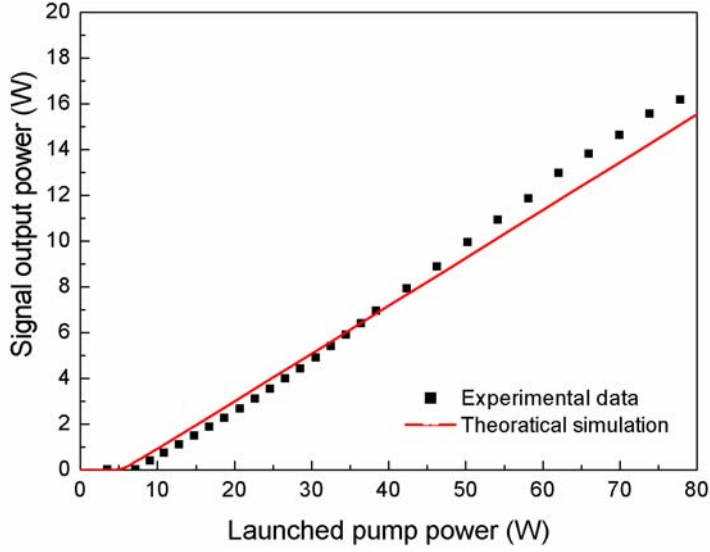


Figure 22 Measured 1.03- μm signal output power generated by the 74.5-cm phosphate fiber amplifier as a function of launched pump power.

The predicted 29.5% overlap was confirmed by studying the residual unabsorbed pump power transmitted by the fiber MOPA (see Fig. 20). Figure 23 shows the measured unabsorbed pump power as a function of launched pump power. At the maximum launched pump power of 76 W, the unabsorbed pump power is as large as 28 W. Figure 24 also shows the unabsorbed pump power predicted by the code for this amplifier, using the same parameter values as to generate the solid curve of Fig. 22, including a spatial overlap of 29.5%. The simulation curve matches the measured data well. This agreement confirms the numerical value of 29.5% for the pump/dopant overlap, and it explains why ~40% of the pump power was not absorbed in the fiber. This relatively low overlap is believed to be due to the high azimuthal symmetry of the core/inner cladding configuration, which results in insufficient scattering of the pump modes in the fiber (which was kept straight). This overlap can be increased by using a fiber with an air hole parallel to the core (see Fig. 25b) [8], as demonstrated in the next section, or a polarization-maintaining fiber, where the stress rods then act as mode mixers.

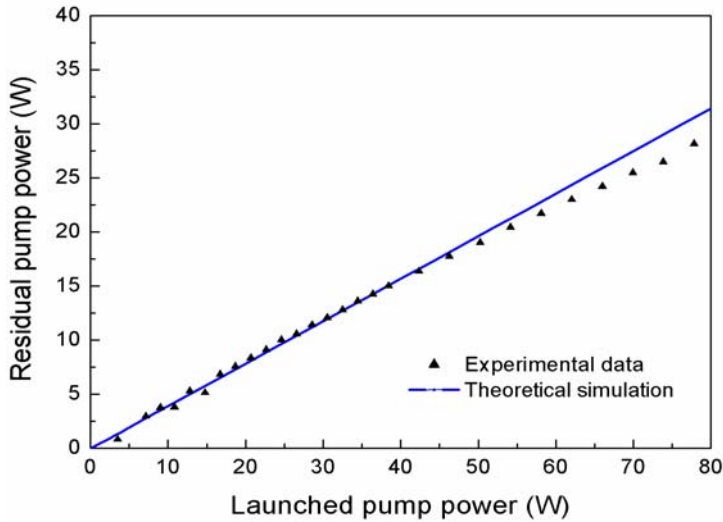


Figure 23 Measured and simulated residual pump power as a function of launched pump power.

The measured output spectrum of the fiber amplifier measured at 14.6 W is shown in Fig. 24. It indicates that the ASE power level is more than 25 dB below the 1029.5-nm signal level. The ratio of total ASE power to signal power was estimated as <1% from our code. As shown in the inset of Fig. 24, the output signal was in the fundamental fiber mode (LP01) and of excellent quality, as expected for a step-index single-mode core.

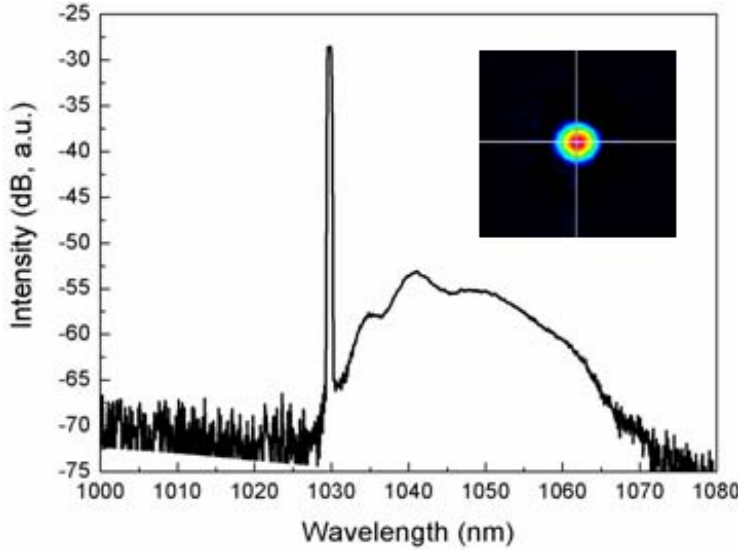


Figure 24 Measured amplifier spectrum at an output power of 14.6 W. The inset is the measured output beam profile.

57-W single-mode phosphate fiber laser

Our early studies of phosphate fiber lasers taught us that adding an air-hole to the inner cladding and making the core eccentric break the axial symmetry of the waveguide and greatly improve the pump/dopant spatial overlap [8]. It was therefore interesting to test these air-hole fibers in our fiber MOPA. However, a high-gain fiber MOPA requires angled fiber ends to avoid lasing. We could neither polish the fiber ends (without clogging the air hole with debris that would induce optical damage) nor cleave them at an angle for lack of suitable equipment. As an alternative, to study the power scalability of this Yb^{3+} -doped phosphate fiber beyond the power level we were able to achieve in an amplifier, we cleaved the ends of the fiber at 90° and used the fiber to make a phosphate fiber laser.

The experimental configuration of this laser is shown in Fig. 25. It consisted of a 71.6-cm length of air-hole Yb^{3+} -doped phosphate fiber placed in an optical cavity. One cavity mirror was a dielectric high reflector (HR) with a reflectivity greater than 99% at 1064 nm, butt-coupled to one of the cleaved fiber ends. The other mirror was the other cleaved fiber end, which provided a 5% reflection and acted as the output coupler (OC). The cleaved fiber end is shown in Fig. 19b. This fiber has the same structure as the fiber used in the fiber MOPA, except that the active core is offset from the fiber center and an air hole is added. The core and the air hole are symmetrically located with respect to the center of the fiber, and 30 μm apart center to center. The fiber was cladding-pumped with a fiber-coupled laser diode at 977 nm through a dichroic beam splitter placed on the OC side. The fiber ends were cooled using the same arrangement as the MOPA, except that the 1-inch mount at the mirror end was also water-cooled.

Our previous phosphate fiber laser [8] had a slope efficiency of 25.8%, which was limited by the relatively low absorption of the 940-nm pump. Significant efficiency improvement in the same laser configuration was achieved by changing the pump wavelength to 977 nm, where Yb^{3+} absorption is much stronger.

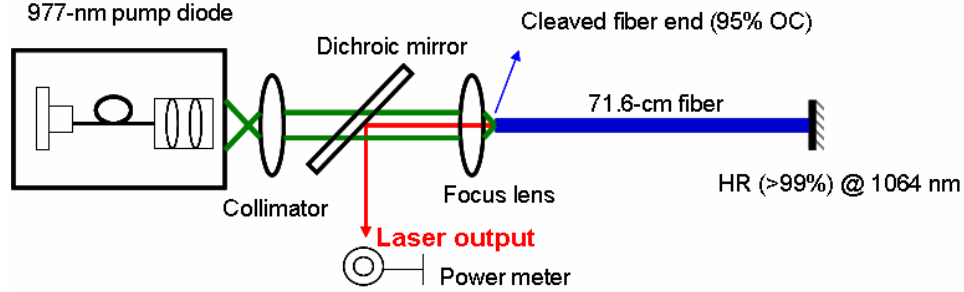


Figure 25 Experimental Yb^{3+} -doped phosphate fiber laser

Figure 26 shows the laser output power measured versus launched pump power. The threshold was ~ 3 W. The maximum output power was 56.9 W for 116.7 W of launched pump power (104.3 W absorbed). The output was in the LP_{01} mode, and the laser FWHM linewidth was ~ 4 nm. The measured slope efficiency was 50.8% against launched pump power and 56.7% against absorbed pump power. These efficiencies are more than twice as high as in our previous laser [8]. In addition, these efficiencies are well predicted by our simulation if we assume a spatial overlap of 100% (solid curve in Fig. 26). At the maximum output power, we observed catastrophic damage of the fiber inside the pump-input V-groove mount near where the fiber exits the mount. We believe the damage was likely caused by excessive stress applied to the fiber's outer surface by imperfections in the machined V-groove in which the fiber rested inside the mount, combined with the pump-induced increase in the fiber temperature.

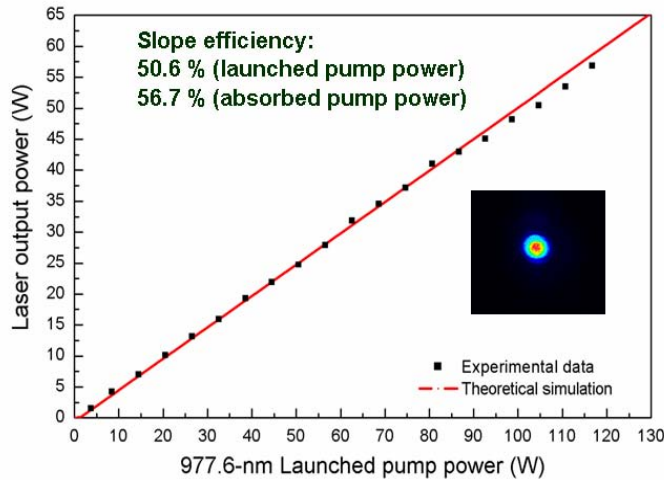


Figure 26 The 1.06- μm laser power generated by the 71.6-cm phosphate fiber laser as a function of the launched pump power at 977 nm. The inset shows the measured output beam profile.

The fiber length used in this laser was in fact optimized theoretically to maximize the laser output power at the highest available pump power. Although the slope efficiency was fairly good, it was not as high as could have been, in spite of this optimization, because not all the pump was absorbed, and increasing the fiber length still further would

have increased the loss at both the signal and pump wavelengths, more so than the gain. Simulations showed that by reducing the fiber loss from 3 dB/m to 0.3 dB/m, the slope efficiency, after optimizing the length, would have been as high as 86%, which is comparable to what is achievable in silica fibers. This analysis shows that it is crucial to study the origin of the loss in the phosphate fibers, in particular whether it comes from absorption or scattering mechanisms. Identification of the loss mechanism will then what steps should be taken to reduce this loss. The fact that bulk phosphate glass can have a much lower loss (~ 0.43 dB/m) [14] than our current phosphate glass fibers suggests that this goal is achievable.

2.3.1.4 Analysis of fiber loss

The propagation loss of our phosphate fibers is expected to arise primarily from absorption and/or scattering. Absorption converts light energy into heat, which not only degrades the laser efficiency but also increases the fiber temperature. The lower efficiency results in a higher pump power requirement, which further increases the temperature. The higher temperature may result in thermal damage and limit the power scalability of the system. In contrast, if scattering is only a source of loss; it reduces efficiency without generating heat. We used this fundamental difference to measure these two components independently.

Absorption loss measurements

In the absorption measurements, the fiber was placed in a calorimeter and optically probed with a 1.55- μm laser, where Yb^{3+} does not absorb. Thermocouples inside the calorimeter measured the fiber temperature increase, from which, after suitable calibration, the amount of heat released by the fiber in the calorimeter per unit time could be calculated. As shown in Fig. 27, the calorimeter consisted of two identical glass

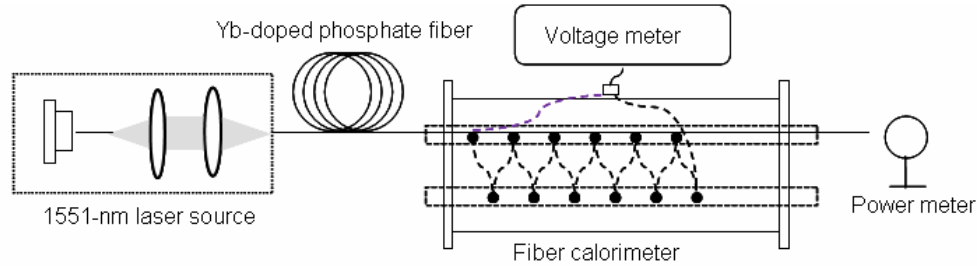


Figure 27 Schematic diagram of the fiber calorimeter.

capillaries placed inside a cylindrical aluminum shield [16]. The two capillary tubes were 16.2 cm long and had an inner diameter of 1 mm. The fiber under test was threaded through one capillary. The other capillary served as a reference. Six thermocouples were attached to both capillaries in series. They were evenly distributed along the capillaries so as to provide the temperature difference averaged over six points along the length of the capillaries. Because only temperature differences are measured, environmental temperature fluctuations are subtracted. The role of the aluminum shield was to maintain a homogeneous temperature distribution in the vicinity of the capillaries. The response of the calorimeter was calibrated by placing a copper wire with known resistance inside the test capillary, then sending a known current through it, giving us a known amount of heat.

A 119-cm length of non-jacketed single-mode 12% Yb-doped phosphate fiber was used in this measurement. The fiber had a core diameter of 5 μm and a cladding diameter of 125 μm . Light from a 450-mW, 1551-nm laser pigtailed to a single-mode fiber was launched into the fiber core. Any light guided by the cladding was carefully stripped before the point of entry of the fiber into the calorimeter by placing index-matching gel on the fiber surface. Since the capillaries' glass has negligible absorption around 1.55 μm , the portion of signal light scattered by the fiber was absorbed only by the aluminum shield, and thus did not induce any heating of the capillaries. After turning on the laser, the fiber temperature rose above the ambient temperature, from the absorbed power at 1551nm, then quickly (~ 2 minutes) settled to a constant value. The absorption loss coefficient of the fiber was derived from the measured steady-state temperature difference between the capillaries and the measured transmitted laser power. The absorption loss coefficient obtained by this process was 2.27 dB/m.

Scattering loss measurements

To cross-check this absorption loss measurement, we also measured the scattering loss of a piece of fiber from the same spool. Portion of a 168-cm length of fiber was placed in 1-inch-diameter integrating sphere coated with barium sulfate, and light from the 1551-nm laser was launched into the fiber. An InGaAs photodiode mounted in the output port of the integrating sphere measured the portion of fiber-guided laser light scattered in the sphere. A baffle was mounted parallel to the fiber to shield the detector from direct illumination with forward-scattered light. The fiber surface prior to its point of entry into the sphere was covered with index-matching gel to strip out cladding modes. The response of the integrating sphere was calibrated by pulling the fiber back until its free end was at the center of the sphere, then measuring the power collected by the detector and comparing it to the known power released inside the sphere. This procedure yielded a scattering coefficient of 0.68 dB/m.

The total loss of this fiber, measured by an independent cut-back method, is 2.95 dB/m at 1551 nm. This value is in very good agreement with the sum of the measured absorption loss (2.27 dB/m) and scattering loss (0.68 dB/m) coefficients. The absorption loss therefore accounts for 77% of the total loss, and scattering for the remaining 23%. In principle, the absorption component is mainly due to impurities in source material, while scattering arises from inhomogeneities in the bulk and/or irregularities at the boundary between the core and inner cladding. This result (77%/23%) indicates that absorption loss must be reduced to improve the efficiency of the fiber laser.

2.3.1.5 Optical damage limit

The limitation that ultimately prevents further power scaling of any laser is optical damage caused by breakdown, thermal loading or stress fracture. This limitation is anticipated to be more prominent in a soft glass such as a phosphate, compared for example to thermo-mechanically tougher glasses such as silica. To this end, it was interesting to study the thermal loading of our high-power phosphate fiber laser, and forecast how high a single-mode phosphate fiber laser can be scaled in power.

Three main optical damage mechanisms need to be assessed when dealing with cw lasers, namely (1) optical surface damage arising from the high electric field at the input and

output ends of the fiber; (2) melting of the glass; and (3) stress fractures caused by radial or longitudinal temperature gradients in the fiber. The surface damage threshold of a 10- μm single-mode phosphate fiber has been discussed in Section 2.3. Melting and stress fracture in lasers are induced by excessive thermal loading of the laser material. Li *et al.* reported a 3-dimensional thermal analysis of short-length phosphate fiber lasers [17]. Measurements have shown that when cooled with TEC coolers, a fiber made with the same phosphate host as used in this work exhibits no signs of damage at 1.5 μm at a thermal loading of 180 W/m. In addition, the thermal simulation further predicted that TEC-cooled phosphate fiber lasers have the potential to dissipate thermal loads up to ~ 1 kW/m with the same cooling design. Assuming a weak dependence of damage on wavelength, this value can be used as a lower bound value for stress fracture and melting in a cooled Yb^{3+} -doped fiber source.

To evaluate how much power can be extracted from a Yb^{3+} -doped fiber laser source before this level of thermal loading is reached, we developed an analytical model of thermal loading. As in other hosts, in a pumped phosphate fiber heat is produced first by the relaxation of phonons that make up for the quantum defect between the pump and laser photons, and second by the absorption component of the fiber loss, which originates from impurities. Both the pump and the laser signal contribute to this second mechanism.

The heat generated per unit time, ΔH_1 , by the first mechanism along a short length of fiber Δz is given by:

$$\Delta H_1(z) = \eta \alpha_{abs}(z) P_p(z) \Delta z, \quad (1)$$

where $\alpha_{abs}(z)$ is the z -dependent, saturated absorption coefficient of Yb^{3+} at the pump wavelength, η is the quantum defect (only $\sim 8.9\%$ in a 1064-nm laser pumped at 977 nm), and $P_p(z)$ is the remaining pump power at z .

The heat produced per unit time, ΔH_2 , by absorption loss of the pump and signal along this same length of fiber Δz is:

$$\Delta H_2(z) = \alpha_a [P_p(z) + P_s(z)] \Delta z \quad (2)$$

where α_a is the absorption loss coefficient and $P_s(z)$ is the laser power at z . The total heat, ΔH , generated along the gain fiber, or thermal load, is the sum of these two contributions,

$$\Delta H(z) = \Delta H_1(z) + \Delta H_2(z) \quad (3)$$

The thermal load of phosphate fiber lasers was evaluated numerically by making use of our simulator, which calculates, among many other parameters, the distribution of the signal and pump powers along the fiber. For simplicity, and without loss of accuracy, we assumed that the pump absorption loss is uniform across the core and inner cladding. The quantum-defect-induced loss is generated only inside the core.

Figure 22 shows the thermal load calculated for the parameters of our experimental fiber laser at its maximum output power of 57 W. Both contributions, as well as the total thermal load, are plotted as a function of position along the fiber. All three curves

decrease monotonically from the pumped (left) end of the fiber, as expected. The highest thermal loading is ~ 200 W/m. The fiber loss accounts for more than 50% of the thermal loading, which stresses again the importance of reducing the fiber loss. If the absorption loss is removed, the loss contribution will become negligible, and the thermal loading will drop to ~ 60 W/m, i.e., about 1 W/m per W of output power, suggesting that from the standpoint of thermal loading and heat removal alone, at least ~ 1 kW could be extracted from this truly single-mode device.

The shaded area in Fig. 28 identifies the portion of the pump-side fiber end that was actively cooled. As mentioned earlier, at the highest pump power the fiber damaged at the point identified by the arrow, which is near the un-cooled portion of the fiber. When replaced, the next fiber damaged also at about the same point. This seems to suggest that the damage was caused by an excessive longitudinal temperature gradient in this region as well as imperfections in the machined V-groove. Cooling the entire fiber should solve this problem.

In addition, we plot the calculated thermal loading for the 700-W phosphate fiber MOPA, reported in Section 2.3, in Fig. 29. The launched pump power was taken to be 700 W in the forward direction and 300 W in the backward direction. The fiber core diameter was $10\text{ }\mu\text{m}$, the core NA 0.07, the inner-cladding diameter $125\text{ }\mu\text{m}$, and the pump wavelength 975 nm. The total pump power was selected to produce a maximum output of 700 W equal to the surface-damage threshold for this core size. Again the loss contribution dominates. The thermal loading is more uniform because of bidirectional pumping. The maximum thermal loading is approximately constant and under 800 W/m. This simulation shows that the thermal-loading limit (> 1 kW/m) is not reached before the onset of surface damage. With suitable cooling, the maximum output power of a single-mode Yb^{3+} -doped fiber laser can be limited by the ultimate damage mechanism, i.e., surface damage.

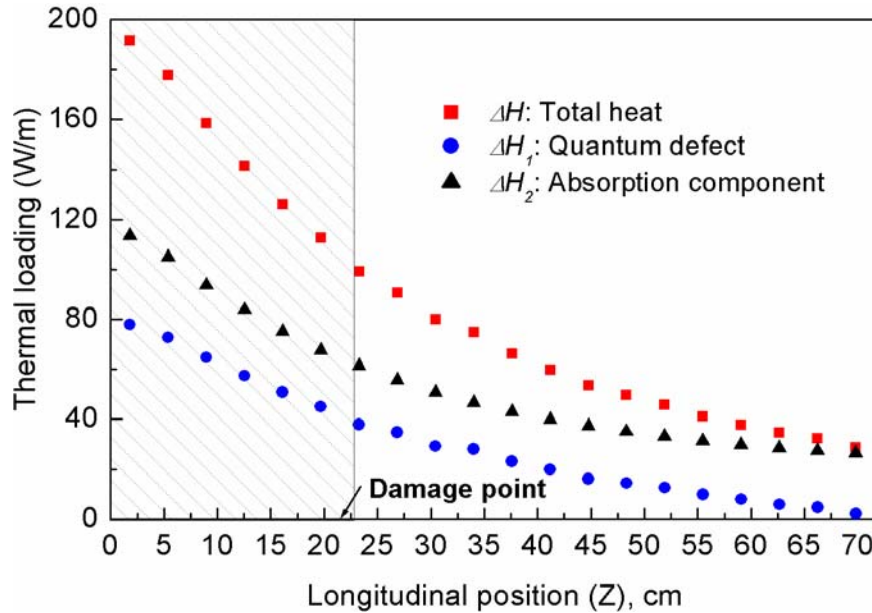


Figure 28 Calculated thermal loading of the 56.9 W phosphate fiber laser.

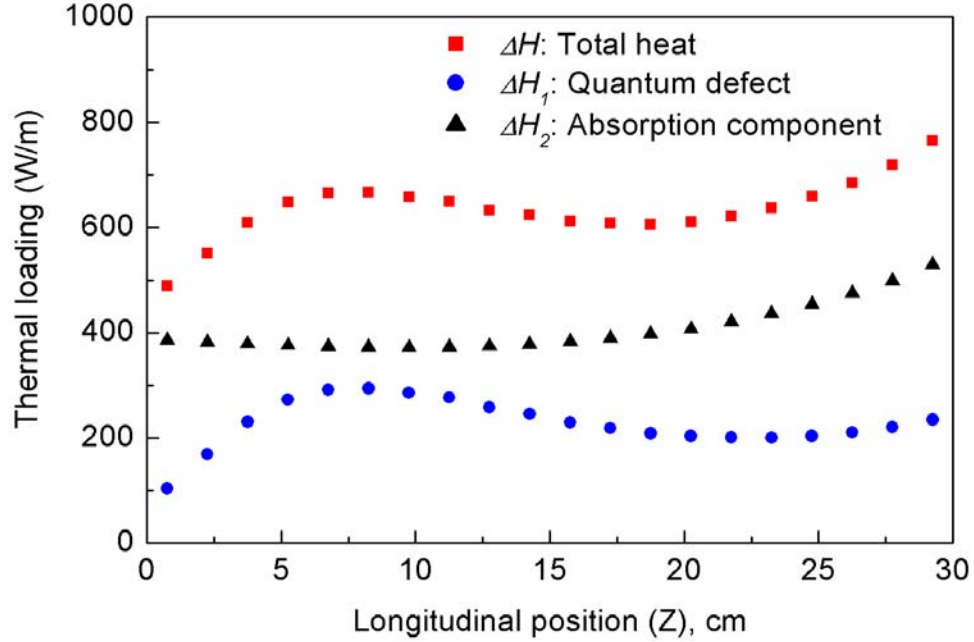


Figure 29 Calculated thermal loading of the proposed 700-W phosphate fiber MOPA

References

- [1] R. Paschotta, J. Nilsson, A. Tropper, and D. C. Hanna, "Ytterbium-Doped Fiber Amplifiers", IEEE Journal of quantum electronics, vol. 33, No. 7, 1997, pp. 1049-1056.
- [2] NP Photonics, Arizona, unpublished results.
- [3] S. Suzuki, S. Jiang, N. Peyghambarian, and A. Chavez-Pirson, "Image amplifier based on Yb³⁺-doped multi-core phosphate optical fiber" Optics express, vol. 15, No. 7, 2007, pp. 3759-3765.
- [4] E. Snitzer and R. Tumminelli, "SiO₂-clad fibers with selectively volatilized soft-glass cores", Optics letters, vol. 14, No. 14, 1989, pp. 757-759
- [5] J. L. Wagener, D. G. Falquier, M. J. F. Digonnet, and H. J. Shaw, "A Mueller Matrix Formalism for Modeling Polarization Effects in Erbium-Doped Fiber," IEEE J. Lightwave Technol., vol. 16, No. 2, 1998, pp. 200-206.
- [6] D. G. Falquier, J. L. Wagener, M. J. F. Digonnet and H. J. Shaw, "Polarized Superfluorescent Fiber Sources", Optical Fiber Technology, vol 4, No. 4, 1998, pp. 453-470
- [7] S. Sinha, Ph. D. thesis, Stanford, Chapter 2, pp. 57-63.
- [8] Y. W. Lee, S. Sinha, M. J. F. Digonnet, R. L. Byer, and S. Jiang, "20 W single-mode Yb³⁺-doped phosphate fiber laser," Optics Letters, vol. 31, No. 22, 2006, pp. 3255-3257.
- [9] J. Koponen, M. Söderlund, H. J. Hoffman, D. A. V. Kliner, and J. P. Koplow, "Photodarkening measurements in large mode area fibers," Proc. SPIE, vol. 6453, 2007, pp. 64531E
- [10] Y. W. Lee, K. E. Urbanek, M. J. F. Digonnet, R. L. Byer and S. Jiang, "Measurement of the stimulated Brillouin scattering gain coefficient of a phosphate fiber" Proc. SPIE, vol. 6469, 2007, pp. 64690L.
- [11] J. Limpert, F. Roser, S. Klingebiel, T. Schreiber, C. Wirth, T. Pesche R. Eberhardt, and A. Tunnermann, "The Rising Power of Fiber Lasers and Amplifiers", IEEE JOURNAL OF SELECTED TOPICS IN QUANTUM ELECTRONICS, vol 13, No. 3, 2007, pp. 537-545.
- [12] J.H. Campbell, T.I. Suratwala, "Nd-doped phosphate glasses for high-energy/high-peak-power lasers", Journal of Non-Crystalline Solids, vol 263&264, 2000, pp. 318-341.

- [13] M.-J. Li, X. Chen, J. Wang, S. Gray, A. Liu, J. A. Demeritt, A. B. Ruffin, A. M. Crowley, D. T. Walton, and L. A. Zenteno, “Al/Ge co-doped large mode area fiber with high SBS threshold”, *Optics Express*, vol. 15, NO. 13, 2007, pp. 8290-8299
- [14] F. Hanson and G.Imthurn, “Efficient Laser Diode Side Pumped Neodymium Glass Slab Laser”, *IEEE J. Quantum Elect.*, vol. 24, No. 9, 1988, pp. 1811-1813.
- [15] S. Sinha, K. E. Urbanek, A. Krzywicki, and R. L. Byer, “Investigation of the suitability of silicate bonding for facet termination in active fiber devices”, *Optics Express*, vol 15, NO. 20, 2007, pp. 13003-13022.
- [16] D. Jundt, PhD Dissertation, Stanford University, 2007, pp. A77-83
- [17] L. Li, H. Li, T. Qiu, V. L. Temyanko, M. M. Morrell, and A. Schülzgen, “3-Dimensional thermal analysis and active cooling of short-length high-power fiber lasers”, *Optics Express*, vol 13, NO. 59 2005, pp. 3420-3428. 6.1 M. Leigh, W. Shi, J. Zong, Z. Yao, S. Jiang, and N. Peyghambarian, High peak power single frequency pulses using a short polarization-maintaining phosphate glass fiber with a large core, *Applied Physics Letters*, 2008, 92, (18), p. 1811.

3. Conclusions and recommendations for further work in fiber MOPA systems

3.1 Summary of research contributions

Yb^{3+} -doped phosphate fibers constitute a promising gain element for power-scaling truly single-mode single-frequency fiber amplifiers to near the kilowatt level. We have shown that as a result of their extremely high doping level, low SBS gain coefficient, and absence of photodarkening. Numerical simulations predict that in a double-clad, step-index phosphate fiber heavily doped with Yb^{3+} , up to ~ 700 W of single-frequency single-mode power can be generated without the onset of SBS, at a thermal-loading level that can be handled by a cooled fiber. As a proof of principle, we report the first high-power sources in a Yb^{3+} -doped phosphate fiber, namely a $1.03\text{-}\mu\text{m}$ fiber MOPA producing 16 W of single-frequency power and a 57-W multiple-frequency $1.06\text{-}\mu\text{m}$ fiber laser. Both sources used only ~ 75 cm of a step-index single-mode fiber doped with as much as 12 wt.% Yb_2O_3 . The slope efficiency of these sources (51% and 57% with respect to absorbed and launched pump power, respectively) is found to be limited by the fairly high fiber loss (~ 3 dB/m). Measurements indicate that 77% of this loss is due to impurity absorption, and the rest to scattering. By reducing the fiber loss from 3 dB/m to 0.3 dB/m, the slope efficiency of these phosphate fiber lasers will be as high as 86% and the thermal loading can be decreased by more than 3 dB. Further studies should focus on reducing this loss and developing cooling systems to achieve higher powers.

3.2 Future directions and applications

3.2.1 Linearly polarized Yb^{3+} -doped phosphate fiber laser sources

The experimental results presented here confirm the feasibility of making high-power, single-mode, single-frequency phosphate fiber laser sources. However, successful demonstration of a linearly polarized output beam is required to fulfill the need of most applications, including gravitational-wave detections. This can be accomplished using polarization maintaining (PM) fibers. PM Er/Yb co-doped phosphate fibers have been used to demonstrate a high-peak-power fiber amplifier at $1.5\text{ }\mu\text{m}$ [1]. Our co-workers at

NP Photonics have fabricated a polarization-maintaining, step-index, single-mode, Yb^{3+} -doped phosphate fiber by using a PANDA fiber structure. However, our preliminary studies showed that the optical properties of this newly fabricated PM phosphate fiber were not good enough for laser applications. Specially, we found its spontaneous radiation was much lower than expected from our simulation code, and the signal propagation loss was much higher than 3dB/m. Both phenomena indicate the material properties of the fiber core need to be improved. Once such a PM truly single-mode Yb^{3+} -doped phosphate fiber can be successfully fabricated, we are confident that a high-power linearly polarized phosphate fiber MOPA with a high polarization extinction ratio and pointing stability can be implemented. In addition, we believe a PM PANDA fiber can provide a high pump/dopant overlap because the stress rods break the circular symmetry of the inner cladding.

3.2.2 Further power scaling of Yb^{3+} -doped phosphate fiber laser sources

To build a single-mode phosphate fiber MOPA with an output power in excess of 200 W for Advanced LIGO, increasing the pump-to-signal conversion efficiency and minimizing the thermal loads will be crucial. Both a high conversion efficiency and low thermal load can be achieved by significantly decreasing the fiber background loss. As mentioned previously, the conversion efficiency will be as high as 83% and the thermal loading decreased by more than 3 dB by reducing fiber losses from 3 dB/m to 0.43 dB/m, the loss value achieved in Nd^{3+} -doped bulk phosphate glass. According to our study, the background absorption loss dominates the total fiber background loss in current phosphate fibers. Further materials research into the wavelength dependence of the background absorption and scattering losses can provide useful information to modify the fabrication process so as to produce lower loss fibers. For the background absorption loss, impurity species existing in the fiber preforms (transition metals or Er^{3+} ions) can be explored through the observation of large absorption lines. Furthermore, each scattering mechanism produces fiber loss with its own wavelength dependence. Rayleigh scattering loss and the loss induced by density fluctuations in multi-component fibers vary as λ^{-4} . However, the scattering loss induced by geometric fiber imperfections is not always wavelength dependent. The wavelength dependence of this type of loss is controlled by the defect dimensions [2]. By measuring the wavelength dependence of the scattering loss, one can perhaps isolate the dominant scattering mechanism in our fibers or even identify the properties of the scattering loss mechanisms.

3.2.3 Pulsed phosphate fiber laser sources

Phosphate fibers are also advantageous for high-power narrow-linewidth pulsed fiber amplifiers as well as broadband Q-switched and mode-locked fiber lasers. For a high-power narrow-linewidth pulsed fiber laser system, phosphate fibers present the same advantages as those mentioned for single-frequency CW fiber laser systems. An additional benefit is that pulsed fiber laser sources require a less advanced thermal management compared to CW laser sources because of their lower average power. In Q-switched fiber lasers, the maximum output power is often limited by stimulated Raman scattering (SRS), as opposed to SBS, because the laser linewidth is very wide. Although phosphate fibers are known to have a SRS gain coefficient 5 times larger than silica-

based fibers [3], they still exhibit a higher SRS threshold power in a Q-switched laser system because the ion concentration can be as much as 10 times higher, and therefore the fiber length can be 10 times shorter. Combining both factors, Q-switched phosphate fiber lasers can generate at least twice as much peak power as silica fiber lasers without the onset of SRS. In contrast to Q-switched fiber lasers, the most troublesome effect in a high-power mode-locked fiber laser source is self-phase modulation (SPM). To push back the SPM limitation, phosphate fibers are a good alternative due to their slightly lower nonlinear refractive index [4] and much shorter required fiber length compared to silica fibers. Overall, we believe that Yb^{3+} -phosphate fibers are a promising material for a new class of pulsed high-power fiber lasers as well.

3.2.4 Tm^{3+} -doped phosphate fiber lasers

Compared to Yb^{3+} and Er^{3+} -doped fiber lasers, Tm^{3+} -doped fiber lasers were developed much later, and they are still currently an active area of fiber-laser research. This new class of fiber gain media can efficiently access the 2- μm wavelength range, which is important for atmospheric data transmission, strongly reducing potential damage to the human eye, and an ideal wavelength for efficient wavelength conversion to the mid-IR region from 3 -5 μm . In terms of fiber laser design, the long emission wavelength allows using larger single-mode cores with reduced nonlinearities. With sufficient Tm^{3+} concentrations, an energy efficiency exceeding 90% is achievable due to a two-for-one optical excitation of the thulium upper laser level through cross-relaxation [5, 6]. Phosphate glass is also an attractive host for high-power single-frequency 2- μm Tm^{3+} -doped fiber lasers because the high solubility of rare-earth ions in this host, its high photo-darkening resistance, and small SBS gain coefficient. In addition, Tm^{3+} ions can also be excited through energy transfer from excited Yb^{3+} ions that can be co-doped into the host glass. Efficient Yb^{3+} -to- Tm^{3+} energy transfer has been utilized to realize dual-wavelength pumping schemes for further power scaling of cladding-pumped Tm^{3+} -doped fiber lasers [6]. Because the phonon energy compared is higher in phosphate than silica, Yb/Tm co-doped phosphate fibers are expected to provide a more efficient Yb^{3+} -to- Tm^{3+} energy transfer. Based on the above, it will be interesting to investigate high-power Tm^{3+} -doped phosphate fiber laser sources.

References

- [1] R. M. Wood, "The power-and energy-handling capability of optical materials," SPIE Press, p. 27 (2002)
- [2] F. L. Galeener, J. C. Mikkelsen, Jr., R. H. Geils, and W. J. Mosby, "The relative Raman cross sections of vitreous SiO_2 , GeO_2 , B_2O_3 , and P_2O_5 ," *Applied Physics Letters*, **32**, (1), p. 34 (1978)
- [3] D. Milam, and M. J. Weber, "Nonlinear refractive index coefficient for Nd phosphate laser glasses," *IEEE Journal of Quantum Electronics*, **12**, (8), p. 512 (1976)
- [4] D. G. Lancaster, A. Sabella, A. Hemming, S. Bennetts, S.D. Jackson, "Power-scalable thulium and holmium fibre lasers pumped by 793 nm diode-lasers," *Advanced Solid-State Photonics*, 2007, Technical Digest, WE5.
- [5] J. Wu, Z. Yao, J. Zong, and S. Jiang, "Highly efficient high-power thulium-doped germanate glass fiber laser," *Optics Letters*, **32**, (6), p. 638 (2007)
- [6] S. Jackson, "Power scaling method for 2- μm diode-cladding-pumped Tm^{3+} -doped silica fiber that uses Yb^{3+} codoping," *Applied Physics Letters*, **28**, (22), p. 2192 (2003)

II. Ceramic Laser Development Program

R. Gaume, J. Wisdom, R. Feigelson, R. Route, and R. L. Byer

1. Introduction

The ceramic laser development program initiated at Stanford under DARPA contract DAAD19-02-1-0184 has largely contributed to bringing together, at an academic research scale, essential lab equipment and expertise in laser ceramic fabrication and characterization. This research program has focused in two complementary directions:

- (i) the fundamental understanding of transparent ceramics fabrication
- (ii) the design of engineered ceramic gain media for improved laser efficiency

Major achievements have been obtained over the course of this contract. In particular, we have investigated and refined a number of parallel approaches to fabricate transparent ceramics and are now in a position to reproducibly attain transparency in undoped and doped YAG, Y_2O_3 and MgAl_2O_4 . Laser grade quality has been achieved recently and later work has been devoted to further reducing residual scattering.

The investigation of transparent ceramic fabrication requirements and constraints for making engineered doping profiles has lead to the development of unique algorithms and design concepts that are now being applied.

Finally, this program also benefited the training of half-a-dozen students in the field of ceramic processing and laser ceramic engineering (3 master's students, 2 graduate students, and 1 postdoc fellow).

2. Progress on the fabrication of ceramics

2.1 Background:

2.1.1 Nanopowder fabrication: the key to transparency

From our studies on the fabrication of transparent YAG, Y_2O_3 and MgAl_2O_4 ceramics, we have determined that the optical quality of the final ceramic depends strongly on the purity, the morphology and the degree of agglomeration of the starting powder. The extension of our existing capability to produce nanoparticles with better control of size, and morphology has broadened the spectrum of nanopowders beyond those available from commercial sources. We have investigated fabrication techniques to reduce scatter loss in the ceramic materials that we produce. Particular emphasis has been given to controlled garnet stoichiometry, particle nucleation and growth from solution. Doped rare-earth sesquioxide and garnet precursor nanoparticles, for example, are obtained by co-precipitation from aqueous solutions. The main processing parameters that influence the final quality of high purity ceramic nanopowders are the pH of the solution, the nature of the anions present, the action of template complexes and the precursor calcination schedule.

2.1.2 Sintering studies - turning a powder compact into a transparent ceramic

Once the powder fabrication process has been validated, our focus has shifted to control of ceramic transparency. In this part of the process, the powder size distribution is tightly controlled within narrow bounds, with the goal being of forming a green ceramic body with a high packing density. Traditional powder casting techniques are employed. During sintering, the relative rates of grain growth versus densification is controlled, as required, using sintering aids to favor complete densification of the material while maintaining small grain sizes. If done successfully, the sintering process leads to an optically clear material, free of voids.

2.1.3 Optical characterization

The optical quality of the ceramic materials that we produce is characterized with standard methods including scatterometry. These measurements are compared to microstructural characteristics as a means to refine the fabrication processes. The optical scattering loss technique is based on a coherent transmission scattering probe, and it provides two-dimensional spatial scattering maps of the optical quality of ceramics. These maps are used to determine the loss signatures of classical scatterers in ceramics (i.e., grain boundaries, secondary phases, microvoids and large pores) and their spatial distribution in large samples. Low levels of scattering loss ($\leq 2\%$) are difficult to detect by other (incoherent) techniques.

2.2 New developments

2.2.1 Transparent Ceramic Fabrication

We have used different fabrication techniques and have developed thus far to significantly decrease the loss level of our materials. It appears that whatever sintering technique one uses (pressureless or hot-pressing), critical attention must be paid to the preparation of the raw powders if scatter-free ceramics are to be achieved. In that regard, the rate of agglomeration of the starting powders is of prime importance. Ball-milling is a very valuable technique to de-agglomerate powders. However, it always contaminates the slurry being milled due to the continuous abrasion of the milling medium as well as generating particulates which are chipped off from the colliding balls. This renders control of the milling very difficult, especially for the case of YAG powders (the maximum solubility limit of alumina in YAG, for instance, is particularly low, ~ 0.1 mol %). One must calibrate the abrasion loss of the balls for given milling conditions (rotation speed, mass and size of the grinding medium, solid fraction of the slurry, diameter of the milling-jar, etc) to account for the stoichiometry shift in the final mixture. During the last period, we have determined the experimental conditions to minimize stoichiometry shift during ball-milling while optimizing powder mixing and de-agglomeration. This has been very effective in improving the optical quality of our YAG ceramics.

2.2.2 Transparent YAG Ceramics

We have carried out comparative studies on different YAG powders and powder forming techniques. These investigations were followed by the fabrication of transparent YAG

ceramics by vacuum sintering and motivated the development of the following powder synthesis technique for the fabrication of transparent ceramics. The results that we obtained however were not always consistent and refining the processing conditions to achieve better consistency appeared to be a priority before stepping forward in the fabrication of gain-engineered materials.

The influence of stoichiometry has been carefully studied on both reactive sintering¹ and non-reactive sintering² routes. We found that the loss during the initial reaction of the starting powders, the main contributor to departure from stoichiometric composition, needs to be known and controlled within tight limits. Series of YAG samples with compositions varying around stoichiometry within $\pm 1\text{mol}\%$ were prepared (Fig. 30) and helped us in determining the solubility limit of both alumina and yttria excess in the YAG phase. The distortion of the YAG lattice parameter induced by the solute in excess was measured by XRD and compared with optical micrograph and scattering data. These characterizations have shown that at most 0.1 mol% of alumina and 0.2 mol% of yttria were soluble in YAG. Within the solid solution domain, sample with an excess of yttria tend to have a smaller grain size than samples having an excess of alumina.



Figure 30 Series of YAG ceramic samples (4-mm thick) with composition slightly departing from stoichiometry ($\pm 0.5\text{ mol}\%$). Samples on the left side are $\text{Nd}^{3+}:\text{YAG}$ (pink), while samples on the right are $\text{Gd}^{3+}:\text{YAG}$ (yellowish). The cloudiness of the samples is associated with the presence of remaining porosity

In a collaborative work [1] with Los Alamos National Laboratory and Imperial College in London, we have been able to relate these lattice parameter changes to the actual nature of the point defects that form as a consequence of composition departure from stoichiometry. It has already been proven that these defects have a profound effect on diffusion kinetics and therefore on densification, grain-growth and dopant diffusion. In addition, they may also affect optical performance by introducing color centers that will compete with normal laser operation or favor photo-darkening.

¹ where intimate mixtures of nanopowders of yttria and alumina are compacted and reacted together at high temperature during the sintering stage.

² where YAG nanopowder fabricated before-hand is compacted and sintered at high temperature.

Contrary to crystal growth, transparent ceramics processing allows for fine composition tuning that is not dictated by thermodynamic equilibria at the liquidus. This particular aspect was a key concept to enable the present investigation. This study not only validates the computational tools that our collaborators developed to model non-stoichiometry in a crystalline lattice, but it also shed a new light on defect formation energetics in the YAG crystalline structure as summarized in Fig. 31. Besides the benefits that this fundamental study will provide on the general understanding of laser ceramic fabrication and performance, it is also expected that it will impact the field of scintillator ceramics.

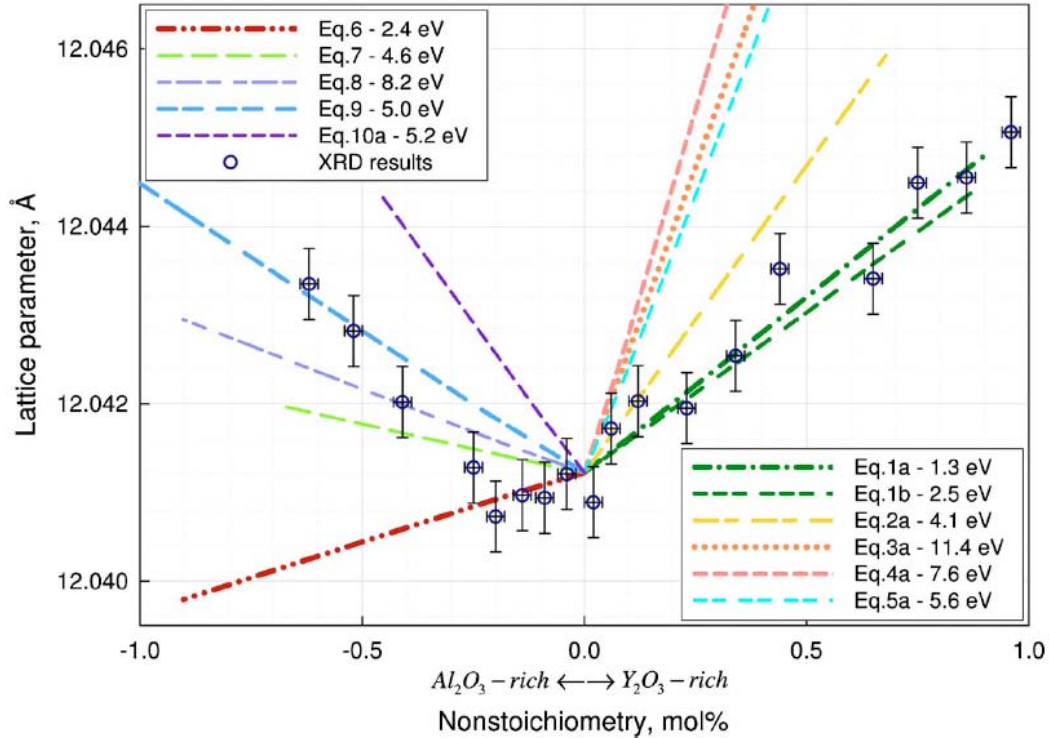


Figure 31 The variation in YAG lattice parameter with respect to deviations from stoichiometry, determined by either atomistic simulation or XRD. The simulation results correspond to various defect reactions identified in this work

Over the last year, we have produced laser grade Nd:YAG and low optical loss Gd^{3+} doped YAG ceramics. Laser performances in Nd:YAG are currently limited by residual scattering and are yet to be improved. The achievement of stabile processing conditions and the recent acquisition of supplemental equipment (spray-dryer), which will help controlling the agglomeration state of the starting powders, make us confident that the optical quality of the ceramics we produce will improve in the near future.

2.2.3 Transparent Y_2O_3 Ceramics

Concerning the fabrication of transparent yttria ceramics, we studied the influence of hot isostatic pressing and air-annealing conditions. As we reported for the last period, we mostly considered the use of hot-pressing to densify this material. Commercial Y_2O_3 powders with purities superior to 99.995%, with 1- μ m average size were used. The

control of the agglomeration rate by decantation has been shown to be crucial in obtaining high quality ceramics (Figs. 32 and 33).

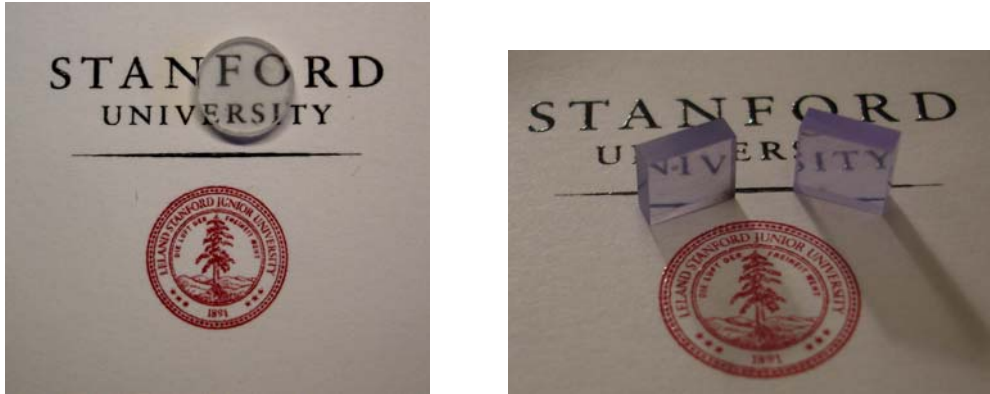


Figure 32 (Left) Piece of a 0.9-cm diameter, 3-mm thick YAG ceramic. (Right) 7x7x2 mm slabs of 0.8 at. % Nd:Y₂O₃ ceramics

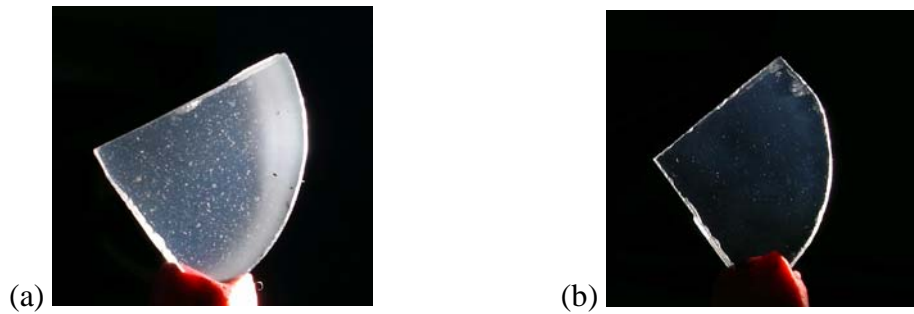


Figure 33 Illustration of the effect of particle classification prior ceramic densification on the scattering centers density. (a) Y₂O₃ ceramic made from unclassified particles. Large particle agglomerates introduce macro- and micro-porosities which preclude the formation of a fully transparent ceramic. (b) Y₂O₃ ceramic made from a classified powder and sintered under the same condition as (a) showing a lesser amount of scattering centers

The optimum transparency is obtained for a HIPing pressure of 200 MPa at a temperature of 1700°C followed by an annealing at 1200°, as shown in Fig. 34 on the next page.

Despite the significant improvements of our process, the optical quality of the ceramics we have produced does not meet laser grade requirements. Some inherent scattering loss not associated with porosity was found to originate from Nd₂O₃ clustering. Cathodoluminescence under scanning electron microscope (Fig. 35a), as well as confocal

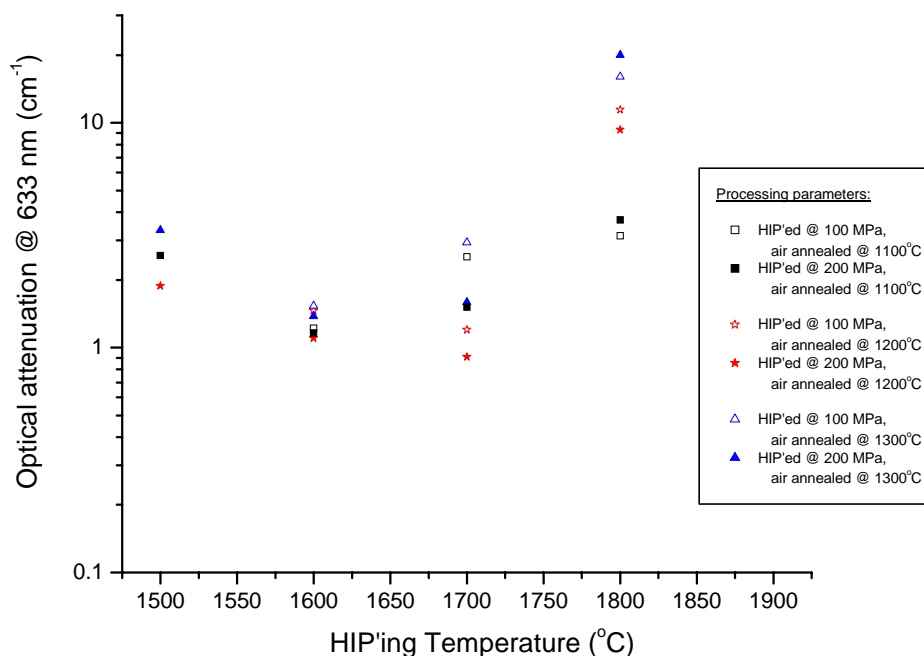


Figure 34 Hot isostatic pressing and air-annealing conditions applied to hot-pressed 0.8 at. % Nd:Y₂O₃ ceramics. Optimum transparency is obtained for a HIP'ing pressure of 200 MPa at a temperature of 1700°C followed by an annealing at 1200°C

microscopy (Fig. 35b), have brought evidence that the inter-diffusion of neodymium and yttrium ions is limited and does not favor mixing of the starting oxides. The clusters of Nd₂O₃-rich grains cause sufficient refractive index fluctuations to preclude the formation of an optically homogeneous ceramic. Our current approach starts with homogeneously Nd-doped yttria particles as a raw material to optimize dopant mixing after sintering.

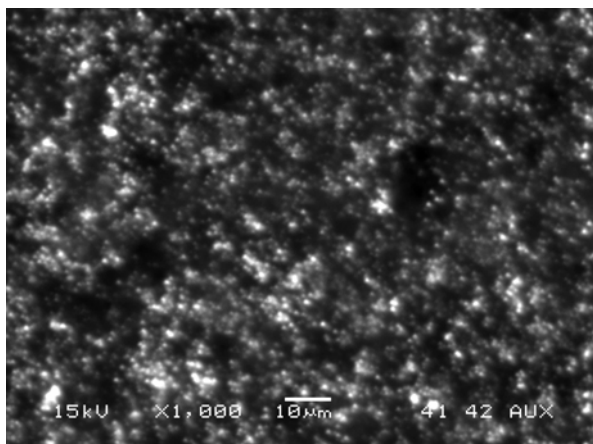
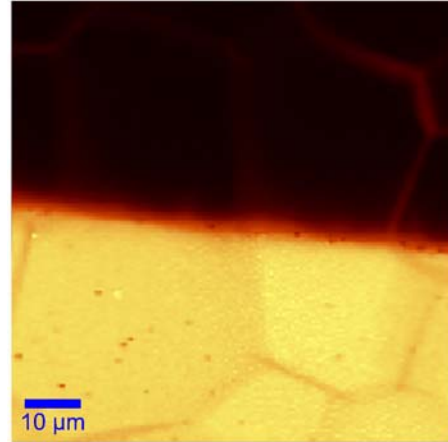


Figure 35a Cathodoluminescence image of a 0.8 at. % Nd:Y₂O₃ ceramic. The luminescence of Nd³⁺ ions excited by a 15kV-electron beam appears as bright spots as a consequence of strong doping inhomogeneities

Figure 35b Luminescence of Nd^{3+} ions at the interface between a doped (bright) and undoped (dark) Y_2O_3 ceramics bonded together and heat-treated for 100h at 1800°C . This image, obtained by confocal microscopy, illustrates the extremely slow inter-diffusion of neodymium and yttrium ions in the Y_2O_3 crystalline lattice. Most neodymium transport happens at grain-boundaries



3. Progress on the design of engineered ceramic gain media

3.1 Background

The utility of the solid-state gain medium is to convert the low brightness light emitted from pump diodes into a higher brightness optical beam. Solid-state laser performance can be improved by engineering a dopant concentration profile (“doping profile”) into the solid-state laser medium. Doping profiles can improve the overlap between pump diodes and cavity modes in edge-pumped geometries [2,3] as well as uniformly distribute deposited heat in a gain medium[4,5].

Laser system engineers currently face severe challenges in making highly efficient 100 kW-class edge-pumped slab lasers. Edge-pumped slabs are ideal for 100 kW class laser systems by allowing pump power to be coupled in along the length of the slab and allowing cooling through two large faces. However, the uniform doping profiles common in single crystal materials tend to have poor overlap between the regions absorbing the pump and the regions sampled by the signal because the signal cannot extract power from the transverse edges of the slab (where a considerable amount of pump power is absorbed). We have reported efforts in an earlier report to develop Gaussian to super Gaussian converters to circumvent this challenge and on doping profile studies to improve pump signal overlap using Gaussian doping profile. The dramatic increase in efficiency resulting from such engineered gain media would reduce pump diode power requirements (i.e. cost) and laser cooling system requirements. The development of transparent ceramic laser materials over the past decade has sparked interest in creating engineered doping profiles. Because engineering doping profiles in ceramics is a straightforward extension of the existing ceramic fabrication process, these materials may have significant potential as a cost-effective alternative to other fabrication techniques. We have fabricated a first generation test device to understand the underlying material science. Such doping profiles in transparent ceramics are fabricated by creating a concentration profile in the green ceramic, which is a formed, but un-cooked collection of nano-particles. Investigations into the benefits of ~3-mm radial doping profiles made by this method have been performed by other authors [6,7,8]. Doping profiles transverse to the beam propagation direction of a small size are useful for improving device

performance because they result in higher inversion densities and therefore higher gain. For laser devices this produces lower laser thresholds and higher slope efficiencies than uniformly doped samples provided that losses are low[9]. If cationic diffusion rates are small enough even waveguides with improved efficiency [10] could be fabricated directly from a green ceramic. However, fabricating a low-loss laser ceramic with a sub-millimeter transverse doping profile is technically challenging since the difference in the sintering rates between doped and undoped regions can lead to the formation of defects such as pores at their interface that increase scattering losses. Because the cavity eigenmode propagates along this interface, laser oscillation in a sample with a small transverse doping profile is an important demonstration for ceramic structures with small spatially varying gain profiles.

3.2 Results and future developments:

The results from our investigations into micro-engineered ceramic structures provided several critical insights. First, the length scale of possible doping profiles can be characterized by measuring distance over which the doping level falls to $1/e$ its initial value, referred to as L , the diffusion length. Multiplying this distance by two is a measure of the possible width of engineerable doping profiles. Accordingly, the measurements of Nd-diffusion distance in reactively sintered ceramics demonstrate that the smallest width for state-of-the-art reactive-sintering techniques is 500 microns wide. The next two questions to ask are what materials systems and processing conditions are best suited for much smaller profile widths (~ 10 microns), and, how useful are large profiles for laser performance?

Processing conditions for 10-micron-wide doping profiles

There are tradeoffs between sintering time and temperature on the overall transparency of a ceramics and the distance doping ions are expected to travel. If a ceramic is sintered at a low temperature for a short time, for example, the dopant ions are not expected to travel very far. However, the optical quality of the ceramic can be expected to suffer because at low temperatures and times the pores within the ceramic are not able to collapse, leaving scattering centers. We performed measurements of the diffusion distances of Nd ions in fully densified (transparent) ceramics and for different sintering times and temperatures. This allowed us to determine the maximum processing time and temperature for 10-micron-wide profiles.

The variation of the diffusion length with sintering time, t , and sintering temperature T , was experimentally shown to follow,

$$L = \frac{t^{3/10}}{\exp(E/(RT) - A)},$$

where E is and experimentally determined activation energy with a value of 310 ± 30 kJ/mol, R is the ideal gas constant and A is a constant with a value of 21.92 using units of microns/hour. According to the measurements, if the initial nanoparticles are larger than

200 nm, 10-micon-wide doping profiles can be fabricated by sintering at 1650°C, for up to 200 hours. There is a greater potential for small doping profiles with single-phase sintering techniques, rather than reactive sintering.

Centimeter-scale doping profiles for laser applications

Doping profiles with 1-cm-and-larger widths are readily achievable with current ceramic processing techniques. One application for doping profiles is to simplify edge pumping of slab lasers by clustering more dopant in the center of the gain medium where it can be easily extracted by a TEM₀₀ mode beam. Figure 36 below shows the relevant geometry. For standard edge-pumped lasers, a gain medium with a uniform doping profile is used. This results in power being absorbed at the edges of the gain medium making it difficult to extract. Clustering more dopant in the center of the slab allows the slab to operate more efficiently with TEM₀₀ beams.

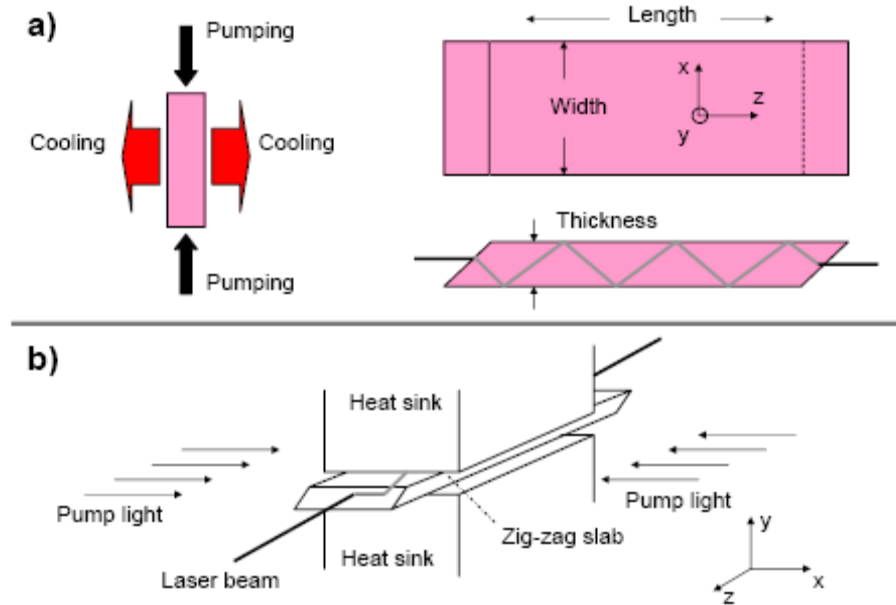


Figure 36 End-pumped (top) and edge-pumped (bottom) geometries

There is a complication that comes with changing the doping level of gain ions: as the doping level is varied the refractive index also changes. Refractive index variations from doping profiles can distort TEM₀₀ beams, eliminating the advantage of more efficient pumping and extraction. Therefore, the doping profile used must be carefully considered, so that it both improves extraction but does not result in large beam distortions. Using a genetic algorithm, we determined a doping profile that was able to improve wall-plug efficiency for an edge-pumped Nd:YAG slab by 39% over an optimally designed uniformly doped slab. The resulting profile is shown in Fig. 37 below.

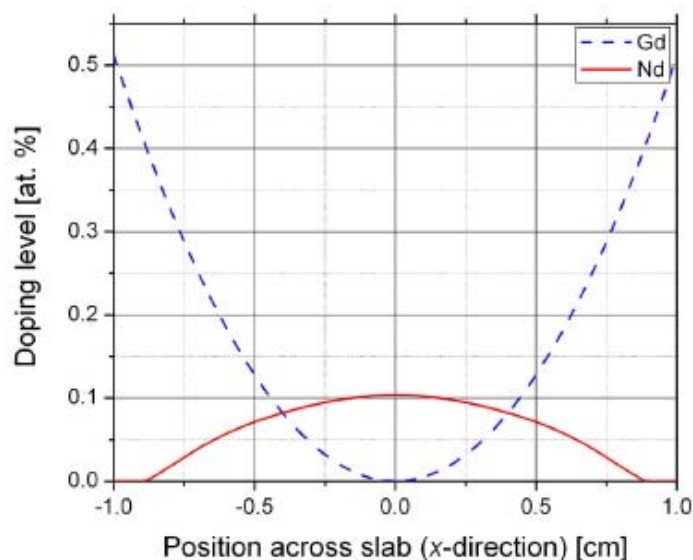


Figure 37 Calculated Nd^{3+} and Gd^{3+} doping concentrations in the cross-section of a laser slab optimized for edge-pumping operation

We have started to produce ceramic composites with simple Gd and Nd profiles and have been carrying out optical characterizations. These preliminary studies will lead the way to the fabrication of more relevant profiles (similar to the one shown in Fig 38) in the very near future.



Figure 38 Preliminary Nd^{3+} , Gd^{3+} :YAG ceramic composites made at Stanford. Samples are 7 mm long and are laser grade

References

- [1] A.P. Patel, M.R. Levy, R.W. Grimes, R.M. Gaume, R.S. Feigelson, K.J. McClellan, and C.R. Stanek, "Mechanisms of non-stoichiometry in $\text{Y}_3\text{Al}_5\text{O}_{12}$ ", Applied Physics Letters, 93, 191902 (2008)
- [2] D. Freiburg, R. Wilhelm, M. Frede, D. Kracht, K. Dupré, and L. Ackermann, "End-Pumped Nd:YAG Laser Applying a Novel Laser Crystal with Longitudinal Hyperbolic Dopant Distribution," in Advanced Solid-State Photonics, Technical Digest (Optical Society of America, 2006), paper WE6
- [3] Born and Wolf, Principles of Optics, pg. 522, 7th edition
- [4] R.J. Smith, R.R. Rice, L.B. Allen, Soc. Photo-Opt. Instrum. Eng., 247, 144 (1980)
- [5] D. Kracht, R. Wilhelm, M. Frede, K. Dupre, L. Ackermann, "407 W End-pumped Multi-segmented Nd:YAG Laser," Optics Express 13, 10140

- [6] T. Bhutta, J. I. Mackenzie, D. P. Shepherd, and R. J. Beach, "Spatial dopant profiles for transverse-mode selection in multimode waveguides," *J. Opt. Soc. Am. B* 19, 1539-1543 (2002)
- [7] D. Kracht, D. Freiburg, R. Wilhelm, M. Frede, and C. Fallnich, "Core-doped Ceramic Nd:YAG Laser," *Opt. Express* 14, 2690-2694 (2006)
- [8] A. Lucianetti, R. Weber, W. Hodel, H. P. Weber, A. Papashvili, V. Konyushkin, T. Basiev," Beam-quality improvement of a passively Q-switched Nd:YAG laser with a core-doped rod," *Applied Optics*, 38, 1777 (1999)
- [9] J. Wisdom, "Design, Characterization and Fabrication of Neodymium Doping Profiles in Transparent YAG Ceramics", Ph.D. Dissertation, Stanford University (March 2008)
- [10] M. Ostermeyer and I. Brandenburg, "Simulation of the extraction of near diffraction limited Gaussian beams from side pumped core doped ceramic Nd:YAG and conventional laser rods," *Opt. Express* 13, 10145-10156 (2005)

III. Phase-stable ultra-short pulse systems

T. Plettner, S. Sinha, S. Wong, R. L. Byer

1. Introduction

Under DARPA contract DAAD19-02-1-0184, we proposed to pursue ongoing research and development at Stanford University and SLAC on structure-based laser-driven particle accelerators. These research programs have focused on the demonstration of this particle acceleration technology and have so far only employed off-the-shelf commercial lasers for experiments designed to test very short accelerator structures powered by a single laser. In the future stages when the accelerator structures are scaled up a phase-coherent laser array will be required for the operation of such a device. Laser-driven particle accelerators employ ultra-short sub-psec pulses, and therefore not only the optical phase but also the envelope timing has to be controlled through the entire accelerator structure. This will either require a phased mode-locked laser array or a master oscillator mode-locked laser followed by stable amplifier stages. In addition, in a similar fashion to RF accelerators the low-energy section of the laser accelerator may require a longer drive-wavelength to allow for larger-volume electron bunches and to mitigate space charge effects. Such wavelengths have to be exact sub-harmonics of the wavelength applied to the downstream sections of the accelerator.

2. Progress to date

2.1 Background

At the present time most laser-particle accelerator experiments employ Ti:sapphire lasers due to their mature stage of development and commercial availability, and for near-future experiments these lasers will be adequate. However for a future wall-plug efficient laser system that powers a larger-scale accelerator more efficient laser systems that are also capable of ultra-short pulse operation appear as better candidates. One example is Yb doped silica mode-locked fiber laser technology, where ~ 36 fs pulses produced directly from the oscillator [1] have been demonstrated. These oscillators use very inexpensive pump lasers and the entire oscillator can be built at a fraction of the cost of a commercial Ti:sapphire laser. We have built and successfully run a 40 MHz oscillator with at least 3 nJ of energy with a compressed FWHM pulse duration of less than 100 fs, and are presently exploring effective means for its comb stabilization. For a sub-harmonic wavelength of 1 μm thulium and holmium (Ho^{3+}) co-doped systems appear as promising 2 μm radiation sources. There are quite a few applications in which it would be preferable to operate at eye-safe wavelengths.

Although the work described is motivated by laser-accelerator technology, other applications may benefit from a phased array of ultra-short pulse laser beams. The objective of the present work is to identify a laser architecture with the following properties, which are summarized below:

- It should produce ultra-short laser pulses in the 100 fsec range with a timing stability below 1 degree of optical phase. Adaptation of existing carrier-to-envelope stabilization techniques to accomplish the required degree of stability will be essential for the long-term objective of the realization of a phase-coherent mode-locked laser array.
- Investigation of the most stable architecture. The envisioned system is likely to include a very-stable low-power mode-locked laser oscillator that serves as a master clock for the entire laser-accelerator and its optical signal will be distributed to local MOPA systems that power individual sections of the accelerator and are optically locked to the master clock.
- Compatibility with the generation of sub-harmonic wavelengths for the injector section of the accelerator. One method includes direct active phase-locking of two different wavelength lasers by stabilization and manipulation of their respective frequency combs and a second possibility includes the production of the sub-harmonic wavelength by utilization of a stable sync-pumped OPO system. At the present time an investigation in this direction is taking place.

2.2 New developments

2.2.1 Ultrafast Phase-Coherent Efficient Degenerate Optical Parametric Oscillator

In the spirit of phase-locking ultrafast mode-locked lasers, we are developing techniques to generate femtosecond phase-coherent pulses using optical parametric processes. We are also seeking ways to make these systems power/energy scalable by improving conversion efficiency.

We decide to use degenerate processes (i.e. the signal and idler frequencies are equal) where all the pump photons are theoretically converted to signal photons so that conversion efficiency can be maximized by reducing the pump quantum defect to zero. Because these are parametric processes, the phase relationship between the pump and signal is correlated and thus can be established and controlled.

There are a few immediate applications for such a sub-harmonic generator:

- Efficient conversion to 1.5 μm (from a tunable Ti:sapphire system) or to 2 μm (from a mode-locked YAG laser or a Yb^{3+} :silica fiber laser). Such wavelengths are useful for applications such as remote sensing, medical/surgical technologies, and phased array of ultra-short and high-energy lasers used to drive a series of particle accelerator structures.
- Sub-harmonic pre-buncher placed before a laser-driven particle accelerator so that electrons are initially bunched at sub-harmonic (or ω/N) wavelengths to suppress effects from neighboring wake fields. Conversion efficiency is not so critical for this.

- Phase-locking techniques for ultrafast systems where the sub-harmonics are used for self-referencing so phase noise may potentially be reduced. Phase coherence is key.

2.2.2 Frequency down-conversion using parametric processes

There are generally two options to generate 1.5 μm or 2 μm : build a laser that directly emits these wavelengths or down-convert a pre-existing laser using optical parametric processes. Material systems known to have atomic transitions at 1.5 μm or 2 μm are hosts (e.g. YAG or silica fiber) doped with erbium (Er^{3+}) and thulium (Th^{3+}), respectively. Systems co-doped with thulium and holmium (Ho^{3+}) are also known to generate 2 μm . Alternatively, optical parametric amplification (OPA) or oscillation (OPO) uses three-wave mixing in a nonlinear crystal to generate a broad range of wavelengths limited by the gain bandwidth and transparency of the crystal as long as energy conservation is met.

We decide to pursue nonlinear down-conversion techniques to obtain 1.5 μm or 2 μm due to the flexibility in ease and practicality. The tunability implies we are not limited by the pump laser and if the pump source is efficient, a degenerate parametric process can have high conversion efficiency. Thulium sources, which can have quantum efficiencies around 2 due to cross-relaxation, are limited by up-conversion processes. Th^{3+} and Ho^{3+} lasers are still in a premature stage of development.

2.2.3 Synchronously-pumped optical parametric oscillator (OPO)

We exploited second-order nonlinear processes for down-conversion to longer wavelengths in the middle infrared. Additionally, we took advantage of the fixed phase relationship between pump, signal, and idler in optical parametric oscillation (OPO), i.e. $\phi_p = \phi_s + \phi_i - \pi/2$. We predicted that a mode-locked OPO operating at frequency degeneracy (assuming type I phase-matching where the signal and idler are co-polarized) would exhibit phase-locking because the signal and idler combs experience mutual or self-injection locking.

Phase coherence between the pump and output waves in a continuous-wave (CW) OPO is automatically accomplished at frequency degeneracy because the signal and idler are indistinguishable. When their phase difference becomes zero (or equivalently an integer multiple of 2π), a degree of freedom in the fixed phase relationship for the OPO disappears, thus yielding a locking requirement given as

$$2\phi_{s,i} - \phi_p = m2\pi + \frac{\pi}{2}. \quad (1)$$

Note that if the identical signal or idler phase is changed by a factor of π , Eq. (1) still remains the same. There are effectively two phase eigenstates.

The locking analysis for a synchronously-pumped OPO (SPOPO), however, needs to account for the multi-axial-mode structure of frequency combs, represented as $f_n = nf_{rep} + \delta$, where n is the mode number, f_{rep} is the mode spacing, and δ is the carrier-envelope offset (CEO) frequency. The synchronous-pumping condition stipulates that f_{rep} is equivalent for the pump, signal, and idler combs. Hence, both $n_p = n_s + n_i$ and $\delta_p = \delta_s + \delta_i$ need to be satisfied. The SPOPO is considered phase-locked when the difference between the signal and idler CEO frequencies is a multiple of the mode spacing because the corresponding temporal carrier-envelope phase slips are identical provided that the carrier frequencies remain equal. The locking condition for the CEO frequencies is

$$2\delta_{s,i} - \delta_p = mf_{rep} \rightarrow 2\delta_{s,i} - \delta_p = 0. \quad (2)$$

When the SPOPO is degenerate, the signal/idler CEO frequency is one-half that of the pump. If the degenerate signal and idler combs are shifted by half a mode spacing in opposite directions, the SPOPO remains in the phase-locked (degenerate) regime; hence, there are two distinct offset eigenstates separated by $0.5f_{rep}$. According to Eq. (2), however, this distinction disappears after doubling the SPOPO comb to compare with the pump comb for confirming phase coherence, analogous to the phase in Eq. (1).

The nonlinear gain element used for the SPOPO was a 1-mm-long MgO-doped periodically-poled lithium niobate (PP-MgO:LN) crystal, which was non-critically phase-matched for 1550 nm at 140 °C. The nonlinear crystal was placed inside a linear near-symmetrically folded confocal cavity, as shown in Fig. 39. A titanium-sapphire mode-locked laser (180-fs pulses at 80 MHz) was employed as the pump at 775 nm. A 50% output coupler was used and a 6-mm long AR-coated plate of fused silica was inserted inside the SPOPO cavity to compensate group velocity dispersion (GVD) at 1550 nm. The SPOPO cavity length was controlled coarsely with a motorized translation stage and finely with a piezoelectric transducer (PZT).

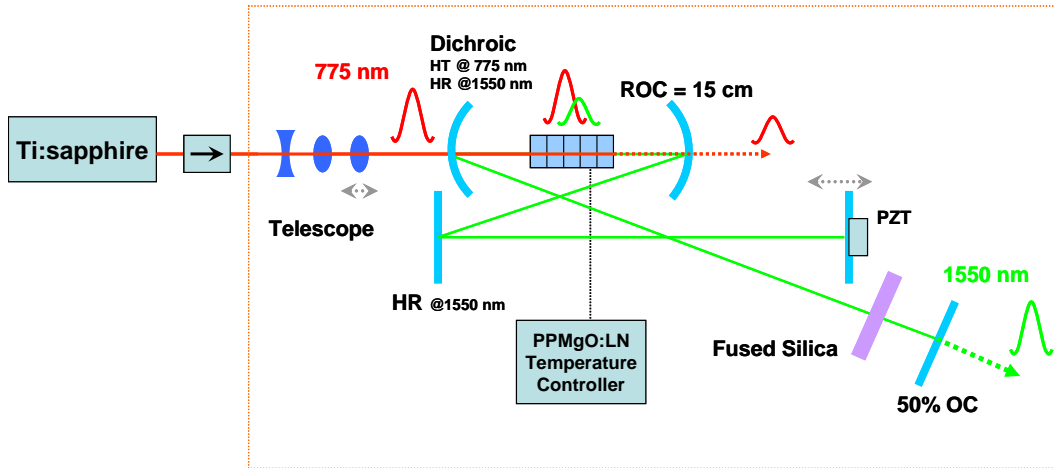


Figure 39 Experimental setup for the SPOPO. The cavity consists of a folded standing-wave confocal resonator. A femtosecond mode-locked Ti:sapphire laser pumps the nonlinear PPMgO:LN crystal.

The degenerate SPOPO pump threshold was measured to be 140 mW. A maximum output power of 250 mW when pumped at 900 mW was observed. The spatially averaged pump depletion reached 60%. The slope efficiency with respect to incident pump power was 32%. The FWHM spectral bandwidth at degeneracy was 200 cm^{-1} or 50 nm centered around 1550 nm. Because the initial pump bandwidth was 75 cm^{-1} , there was output comb broadening factor of about three. The duration of the degenerate output pulses was 70 fs and thus transform-limited for Gaussian profiles. Fig. 40 compares the clean degenerate pulse with a distorted non-degenerate pulse.

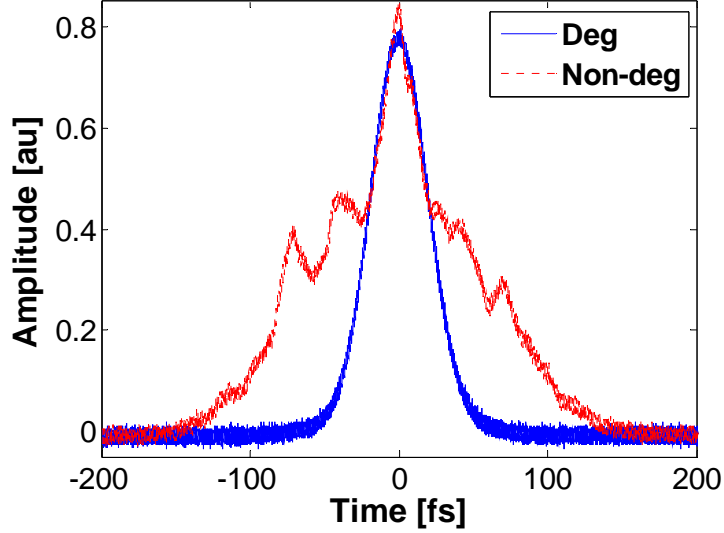


Figure 40 Comparison of the autocorrelation pulse shape and width between degenerate and non-degenerate SPOPO operation. The degenerate pulse is transform-limited with a duration of 70 fs whereas the non-degenerate pulse is wider with a distorted profile.

While the pump wavelength and crystal temperature were kept fixed, a change in the SPOPO cavity length was applied to alter the operating state. Within the degenerate regime, adjusting the roundtrip cavity length by $\lambda_c/2$ (where λ_c is the 1550-nm oscillating wavelength) switched between the offset eigenstates. A substantial length change caused the SPOPO to become non-degenerate (to preserve cavity synchronism) such that distinct signal and idler peaks appeared in the spectrum. As shown in Fig. 41 on the next page, the optical spectrum is the primary metric for distinguishing between degenerate and non-degenerate SPOPO operation.

Phase-coherence of the degenerate SPOPO was confirmed using three techniques. In the first method, the frequency-doubled output was interfered with the pump beam at a low angle to generate a spatial fringe pattern. Observation of stable fringes with high visibility implied phase coherence in accordance with Eq. (1) while blurring denoted random phases. In the second technique, the same interference setup was measured collinearly to analyze the RF spectrum. Observation of only harmonics of the repetition rate indicated phase coherence as stipulated by Eq. (2) whereas emergence of satellite beat notes represented unlocked SPOPO operation due to mismatch of CEO frequencies. Figure 42 shows the interference results and confirms that the degenerate SPOPO

exhibited phase-locked operation while the non-degenerate SPOPO produced unlocked behavior.

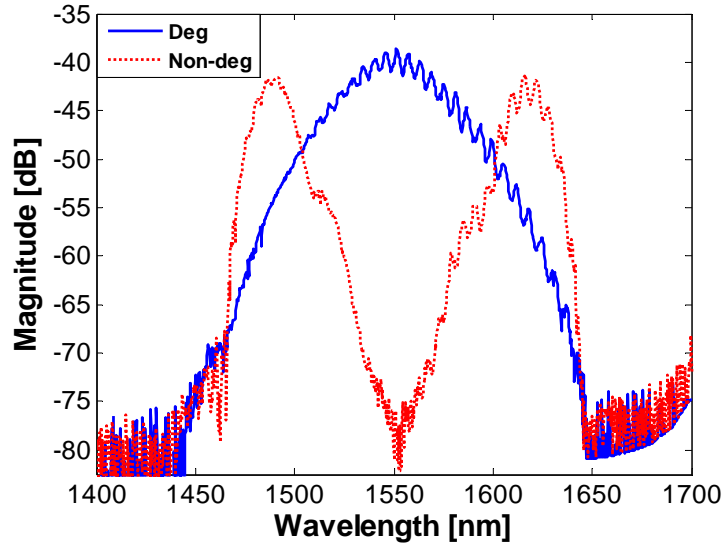


Figure 41 Comparison of the optical spectrum between degenerate and non-degenerate SPOPO operation. The degenerate spectrum is continuously broad around 1550 nm while the non-degenerate spectrum consists of distinct signal and idler peaks symmetric around 1550 nm.

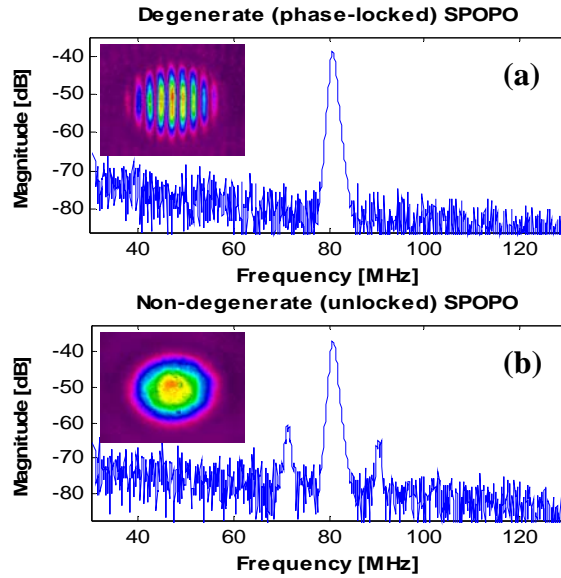


Figure 42 Measurements obtained from frequency-doubling the SPOPO output and interfering with the pump for (a) degenerate and (b) non-degenerate operation.

The third method employed an independent 1550-nm CW laser serving as an external phase reference. The beat notes between the degenerate SPOPO and CW laser and between the pump and frequency-doubled CW laser were compared. The pump laser was allowed to drift across the 80-MHz repetition rate to observe how the CEO frequency of the SPOPO would behave in response to a varying pump offset. Phase-locking required the SPOPO beat note to be half the pump beat note, in accordance with Eq. (2).

Figure 43 shows the scatter plot of the degenerate SPOPO beat notes with the drifting pump beat notes over an 80-MHz window.

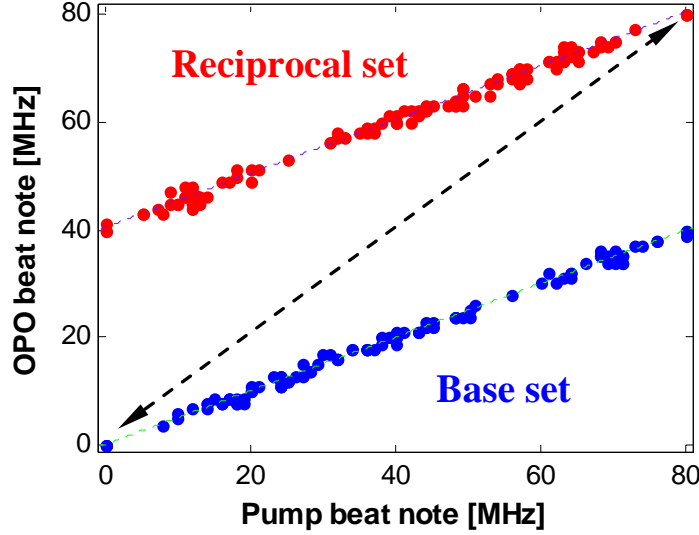


Figure 43 The scatter plot shows that the slope of the degenerate SPOPO vs. pump beat notes is one-half, as required for phase-locking. The base and reciprocal sets are redundant data points symmetrical around half the repetition rate.

No feedback servo loop was needed for the SPOPO to maintain self-injection-locked oscillation. Despite the lack of active stabilization, the phase-locked SPOPO would routinely regain self-phase-locking after application of deliberate small perturbations had stopped. The degenerate SPOPO operated stably for up to an hour when there were minimal environmental noise stimuli.

The frequency locking range can be interpreted as how much cavity length detuning is tolerated while maintaining self-phase-locked operation in the SPOPO. Around each degenerate signal/idler axial mode within the output comb, there exists some feedback mechanism from intrinsic parametric nonlinearity at gain saturation that pulls the signal and idler together, thus rendering this frequency excursion range as an effective potential well. Solving the phase evolution equation from the degenerate nonlinear coupled wave equations and using simple perturbation analysis, we discover a phase correction effect within the nonlinear crystal – a dynamic entity that not only has a gain profile but also a dispersion (phase) profile – that counters perturbations of the cavity length, thus enabling the OPO to continue operating at maximum gain, which occurs at degeneracy in our case. Making appropriate assumptions, we can derive an approximate analytic expression as a heuristic model for the frequency locking range based on operating parameters, given as

$$\Delta f_{lock} \approx \beta \gamma \sqrt{N-1} \quad (3)$$

where N is the number of times above pump threshold, $\gamma \equiv \alpha_s f_{rep}$ is the cavity decay rate with α_s as the resonating signal/idler losses (including out-coupling), and

$\beta \equiv \left(2\pi\sqrt{g_s g_t}\right)^{-1}$ is the coupling coefficient with g_s and g_t as the spatial and temporal overlap between the signal and pump pulses, respectively. The functional form of Eq. (3) is comparable to the locking range expression derived from the Adler phase equation for steady-state injection locking.

The length of the oscillation window versus cavity length detuning for each SPOPO degenerate state (in either offset eigenstate) is effectively a measure of the frequency locking range because the SPOPO ceases to oscillate when the signal and idler modes deviate outside the locking range around degeneracy owing to lack of sufficient gain. Figure 44 shows the locking range measured as a function of number of times above threshold (i.e., parametric gain), and Fig. 45 shows the locking range measurements by varying output coupling (i.e., inverse cavity Q) at twice above threshold. Both sets of data are consistent with Eq. (3) where the frequency excursion has a square root relation with the gain and a linear relation with the cavity decay rate.

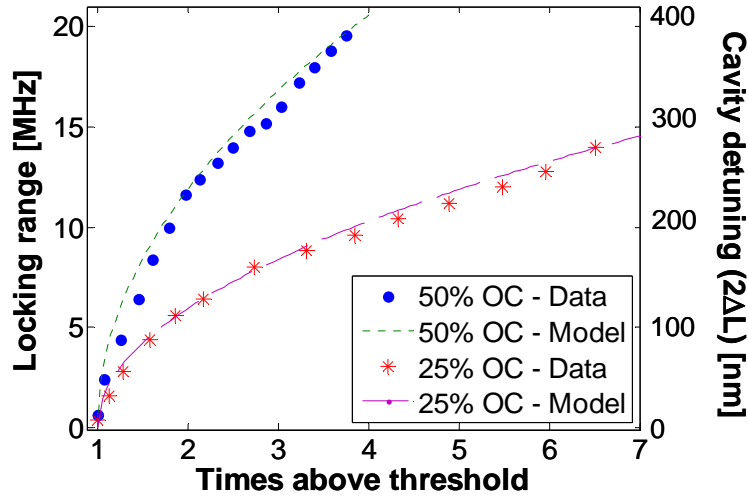


Figure 44 Measurements of locking range as a function of number of times above pump threshold for different output couplers. The data fit heuristic model in Eq. (3) reasonably well.

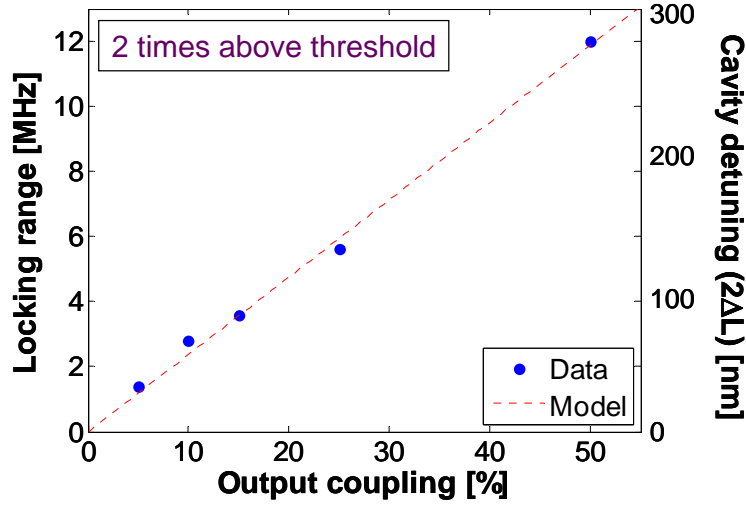


Figure 45 Measurements of locking range as a function of output coupling at twice above pump threshold. The data fit heuristic model in Eq. (3) reasonably well.

3. Summary and directions for further studies on phase-stable, ultra-short pulse systems

To our knowledge, this is the first demonstration of a self-stabilizing phase-locked divide-by-2 type I SPOPO operating in the degenerate regime as a novel frequency comb generator. In the past, type I degenerate mode-locked OPOs have been avoided due to the common misperception that such systems are inherently unstable and impractical, thus requiring exceptional control to operate. Our work confirms that this is not the case. We show that these OPOs are actually well-behaved where the frequency comb structure precludes mode hopping and clustering effects. When the SPOPO is self-phase-locked in the degenerate regime, it is inherently stable in its most preferred mode of operation where the signal and idler favorably couples with each other due to mutual injection locking. Not only does true degeneracy between individual signal and idler comb modes enable phase coherence relative to the pump modes, self-stabilization owing to intrinsic nonlinearity during gain saturation completes the self-phase-locking phenomenon.

Future directions for this work include broadening the output frequency comb to at least an octave and expanding the frequency locking range to a free spectral range (i.e., axial mode spacing) such that the phase-locked degenerate SPOPO would be impervious to any cavity perturbation. The biggest challenge for reaching an octave of output spectrum is not the phase-matching gain bandwidth, which is easily obtained using a very short crystal length, but dispersion control. Our SPOPO output bandwidth was limited primarily by third-order dispersion. We achieved a maximum locking range of 20 MHz (one-quarter of the FSR) using a 50% output coupler with the available pump power. The cavity Q could be reduced for a wider locking range but there is a limit to the amount of out-coupling. Other strategies would be to use shorter pulses or even shorter crystals. The basic premise is to increase the SPOPO threshold such that more pump power could

be injected into the system for higher parametric gain while maintaining the ideal OPO operating point of twice above threshold to minimize adverse effects from parasitic higher-order nonlinear processes.

To obtain higher peak powers, optical parametric amplifiers (OPA) could be employed. If the OPA is pumped by the same pump laser and seeded by the degenerate SPOPO output, the phase and CEO frequency relationships required for locking should be preserved. These SPOPO-OPA systems could then be cascaded to synthesize phase-stable frequency combs in the mid-IR, thus enabling high-precision metrology as well as high-resolution, broadband, and real-time molecular spectroscopy at wavelengths inaccessible to solid-state lasers. The phase-locked degenerate SPOPO could also be used as a robust front-end sub-harmonic injector for the laser-driven particle accelerator.

References

- [1] H. Lim et al, "Generation of 2-nJ pulses from a femtosecond ytterbium fiber laser", OPTICS LETTERS, Vol. 28, 3550 (2003)

VI. 1.48 μm Laser Diodes for In-band Pumping of Erbium-Doped Laser Hosts

H. Bae, T. Sarmiento, J. S. Harris Jr.

1. Introduction

High power laser sources operating at 1.5~2.0 μm are important for eye-safe remote sensing applications. Erbium-doped solid state lasers are good candidates for high power laser sources at these wavelengths. These lasers are most efficient when the quantum defect is minimized by using in-band pumping at around 1.48 μm . However, efficient high power laser diodes at this wavelength have not been available; thus, most systems use 975 nm pump diodes. We propose to develop high power, high efficiency laser diodes operating at 1.48 μm , using GaInNAsSb/GaNAs quantum wells grown on GaAs.

2. Progress

2.1 Background

InGaAsP grown on InP has been mainly used for 1.3~1.55 μm optical communications. As 1.48 μm falls in this wavelength range, InGaAsP on InP may seem like a reasonable choice for 1.48 μm high power diode lasers. However, this material system does not possess good material properties for high power laser diodes. InGaAsP/InP has small conduction band offset and low thermal conductivity, which severely limits its usefulness for continuous high-power operation. Our research has focused on a new quinary material, GaInNAsSb grown on GaAs, as the active gain layer for 1.48 μm high power laser diodes.

GaInNAsSb is one of the materials that are collectively called “dilute nitrides”, which have a small amount (up to a few percent) of nitrogen incorporated into other III-V materials, such as InGaAs, GaAs or InP. Research of dilute nitrides has been of particular interest since Kondow and coworkers discovered that the addition of small amount of nitrogen can drastically reduce the bandgap of GaAs[1]. Among dilute nitrides, GaInNAs has been heavily researched for optoelectronic devices for 1.3~1.55 μm wavelength range. This opens up a new wavelength range that was previously unavailable for GaAs substrates, enabling monolithic VCSEL (vertical-cavity surface-emitting laser), which is a promising light source for low-cost high-density optical links. GaInNAs can also be a part of multi-junction solar cells grown on GaAs, to improve their conversion efficiency[2]. For laser diode applications, larger conduction band offset for GaInNAs on GaAs is believed to enable better temperature stability, which, in combination with the better heat conductivity of GaAs substrates, can enable higher-power laser operation.

1.3 μm laser operation using GaInNAs was achieved with reasonable efforts, but it has been difficult to increase the emission wavelength beyond 1.3 μm , mainly due to the

rapidly degrading material quality with higher nitrogen content. It has since been found that adding antimony to GaInNAs as a surfactant improves the material quality [3], and that antimony also helps to further red-shift the emission wavelength [4]. Employing GaInNAsSb as the active material, we achieved the first continuous-wave edge-emitting laser operation at 1.5 μ m grown on GaAs [5], which is a solid first step toward high-power laser diodes in this wavelength range. And we further reduced the threshold current density significantly, through various growth and structure optimizations, achieving lowest threshold at 1.5 μ m and 1.55 μ m wavelengths. Lower threshold current density can increase the efficiency of laser, which in turn reduces undesirable heat generation during high power laser operation. More recently, we found additional four-fold improvement in the material quality as measured by photoluminescence. But it did not reduce the threshold as expected, and we believe the laser threshold is now more dominated by Auger recombination or leakage current rather than by defect-related recombination, and it agrees well with the low characteristic temperature of our lasers. Further analysis is under way to determine whether the dominant mechanism is Auger recombination or leakage current.

The overall progress that was achieved through the project years is presented in the following two sections. Results from earlier project years are presented first, and the results from the last project year is presented in the second section.

2.2 Developments during earlier project years

The quality of GaInNAsSb quantum well(QW) was measured by photoluminescence (PL) technique, where electron-hole pairs are generated by irradiation from an argon laser, and the spontaneous emission from the recombining pairs is measured by a photodetector. This measurement shows higher PL intensity as the material is improved by reducing defect density. We tried to improve and optimize the growth of the GaInNAsSb material based on the PL intensity as a measure of material quality, and tested the effects of the improvements by fabricating and measuring edge emitting lasers.

The edge-emitting lasers fabricated and measured for this project were grown on a (100) n-type GaAs substrate by solid source molecular beam epitaxy (MBE), with nitrogen supplied by a plasma cell. Monomeric and dimeric antimony was supplied by an unvalved antimony cracker. N- and P-doping were provided by silicon and CBr₄, respectively. The active layer is a single 75 Å GaInNAsSb quantum well surrounded on either side by 220 Å GaNAs barrier. The GaNAs barrier is under tensile strain, and compensates for the compressive strain of the GaInNAsSb layer. The QW and the GaNAs barrier is embedded in the center of an undoped GaAs waveguide, surrounded by doped AlGaAs cladding layers [5].

Ridge widths of 5, 10, and 20 μ m were defined using a combination of lift-off metallization and a self-aligned DRIE etch. The wafer was thinned down to 120 μ m and back metal was evaporated. Then the devices were annealed at 410°C to reduce contact resistance. Device bars ranging in length from 400~3000 μ m were manually cleaved, and measured with the epi-side up.

We first achieved CW lasing at $1.498\ \mu\text{m}$ with a threshold current of $1.06\text{kA}/\text{cm}^2$, as shown in Fig. 46. The continuous-wave slope efficiency was $0.26\text{W}/\text{A}$, corresponding to a 31% external quantum efficiency. Additionally, devices showed maximum CW output powers of $\sim 140\text{mW}$ before thermal rollover. Excellent temperature stability was also observed. The CW characteristic temperature (T_0) was measured to be 101K in the range of $10\text{--}70^\circ\text{C}$ and 135K in $10\text{--}60^\circ\text{C}$. The devices did not lase beyond 70°C indicating the onset of Auger recombination or other highly temperature dependent process. This was the first report of a CW GaAs-based laser in this wavelength range.

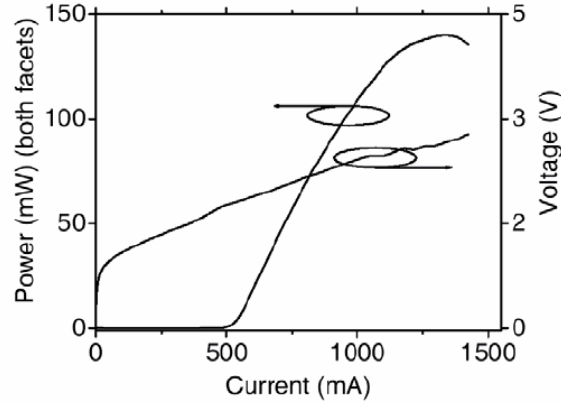


Figure 46 CW L-I curve for a $20\mu\text{m} \times 2450\mu\text{m}$ device (1st generation[5])

We improved the material quality of GaInNAsSb quantum well, by better purification of the nitrogen source gas and reduced plasma damage by using deflection plates at the exit aperture of the plasma cell to steer ions away, as shown in Fig. 47.

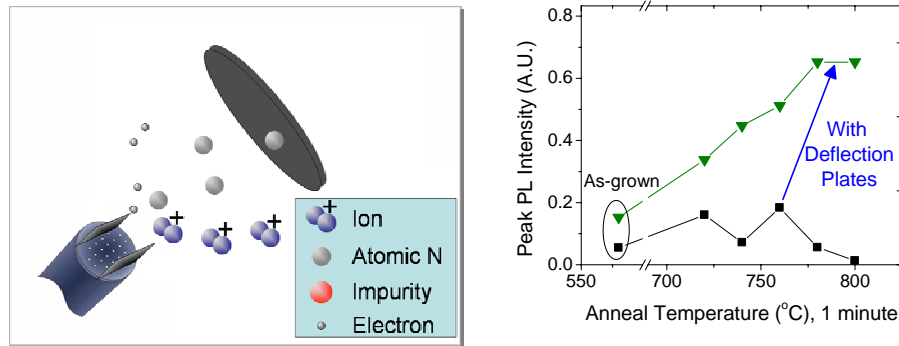


Figure 47 Schematic of ion removal by deflection plates and PL intensity comparison [6]

The edge-emitting lasers employing this improvement lased at $1.5\ \mu\text{m}$ with a threshold current of $580\ \text{A}/\text{cm}^2$ [7]. The external efficiency was 54% and the peak wall-plug efficiency was $\sim 14.8\%$, as shown in Fig. 48a. The peak CW output power was limited to $200\ \text{mW}$ due to junction heating (epi-side up mounting). Under 0.1% duty cycle pulsed operation, the threshold current density was $450\ \text{A}/\text{cm}^2$ and peak output power was 1.1W , which was limited by the current supply, shown in Fig. 48b. The threshold values were the lowest value on GaAs-based lasers for this wavelength at the time.

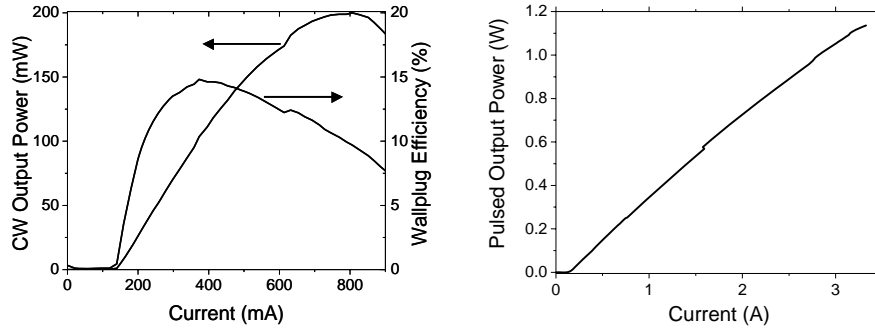


Figure 48 Results for a 20 μm x 1220 μm device (2nd generation [7])
 (a) L-I curve and wall-plug efficiency, CW operation (b) L-I curve, pulsed operation

Two more growth and structure optimizations led us to achieve the next generation of lasers, which lased at 1.54 μm with a record low threshold current density of 373 A/cm² under CW mode operation[8].

The first optimization was to change QW composition for thermal robustness. The QW in a laser structure is exposed to about 2 hours of subsequent GaAs and AlGaAs growth, during which it may be damaged by the heat. We found that less indium and more nitrogen leads to better thermal robustness, which allows the QW to survive the heat from the subsequent growth [9].

The second optimization was etching the ridge waveguide deeper than before, etching through the QW layer. In our first process, we stopped etching about 200 nm above the QW as shown in Fig. 49(a). These shallow-etched diode lasers showed a threshold current density of 550 A/cm² in pulsed mode and 580 A/cm² in CW mode. When we etched them through the QW (Figure 49(b)), they exhibited substantially lower thresholds of 373 A/cm² and 318 A/cm² in CW and pulsed modes, respectively. We believe that the deeper etch reduces the lateral diffusion of carriers away from the ridges, thereby resulting in lower threshold [8].

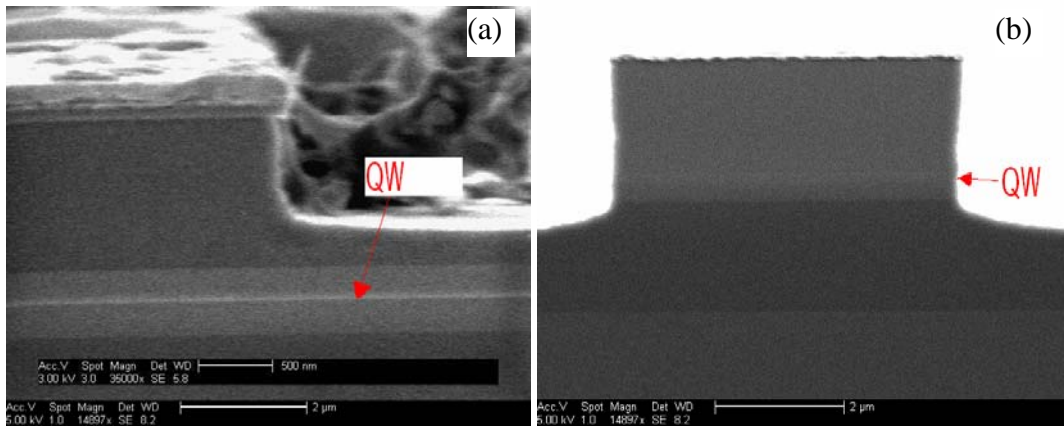


Figure 49 SEM picture of (a) shallow-etched lasers (b) deep-etched lasers.

The external efficiency was 41% and the maximum CW output power was 250 mW, shown in Fig. 50a. To investigate the maximum power achievable in the absence of thermal rollover, we operated the laser diode at a duty cycle of 0.1% and we obtained a peak output power of 650 mW, shown in Fig. 50b.

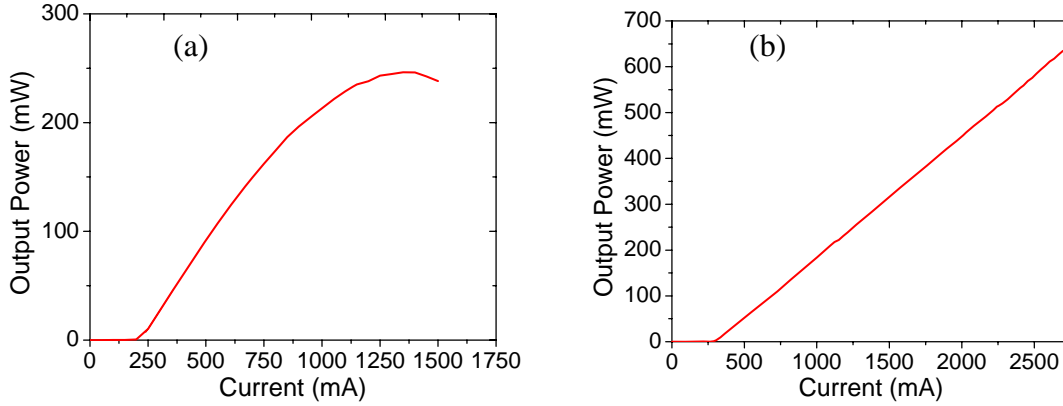


Figure 50 L-I curve for a 20 μm x 2933 μm 3rd generation device [8], (a) cw operation (b) pulsed operation

We found further improvement in material quality is possible by using lower As and Sb fluxes during growth, and annealing at lower temperatures for longer durations.

Up to this point, we had been growing the GaInNAsSb material at 440°C under a group-V-to-group-III flux ratio of 20. We had chosen this growth condition in the past, because the growth temperature of 440°C seemed to be optimum when the V/III flux ratio was fixed at 20, and the V/III flux ratio of 20 seemed optimum when only the arsenic flux was varied while the antimony flux was fixed. It is to be noted that in this previous optimization scheme, the antimony flux was actually not optimized at all. Therefore, we tried changing the antimony flux along with the arsenic flux, with the Sb/As flux ratio fixed [10]. The result was pleasantly surprising. As shown in Fig. 6, we improved the PL intensity by a factor of two, by using lower group V fluxes than in the past.

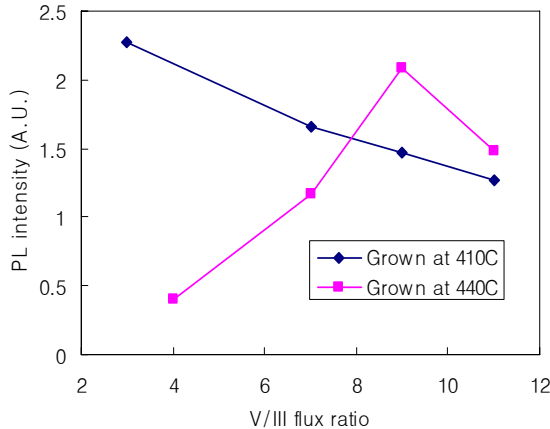


Figure 51 Group V(arsenic + antimony) flux ratio optimization. 20 was used in the past. (PL Intensity normalized to the best quality, after one-minute anneal, achieved through 2006)

Further improvement in material quality was achieved by improving post-growth annealing methods. The PL experiment samples and the lasers in the past were annealed for one minute at different temperatures, to find the optimum annealing temperature. The results in Figure 6 were also annealed for one minute. We found that annealing for longer durations and at lower temperatures results in better PL intensity by a factor of two, compared to the best achievable with one-minute annealing [11,12]. This improvement combines multiplicatively with the improvement by lower As/Sb fluxes. As shown in Fig. 52, we found about four times higher PL intensity than was possible with shorter, higher temperature anneals.

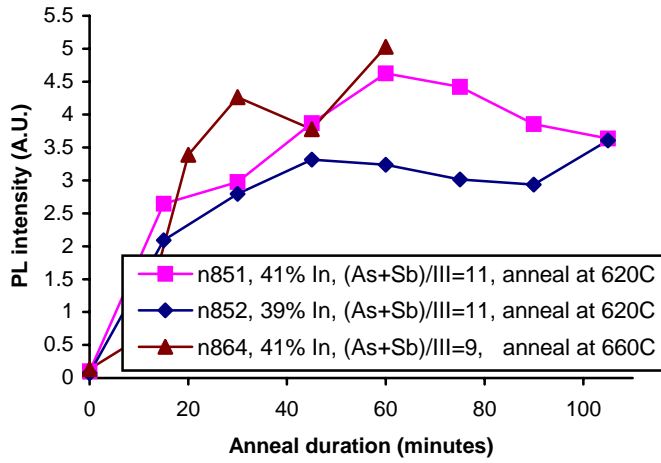


Figure 52 Optimization of post-growth annealing. Annealed at 620C. (PL Intensity normalized to the best quality after one-minute anneal, up to 2006)

2.3 Developments during the final project year

Despite the four-fold improvement in PL intensity, the lasers using improved QWs did not show improvement in threshold current density. The lasers showed threshold current density of 554A/cm² in CW mode at 1.48μm wavelength. The maximum output power was 750mW in pulsed mode and 230mW in CW mode, as shown in Fig.53. Pulsed-mode output power was limited by the laser driver, and CW-mode output was limited by the heat sink.

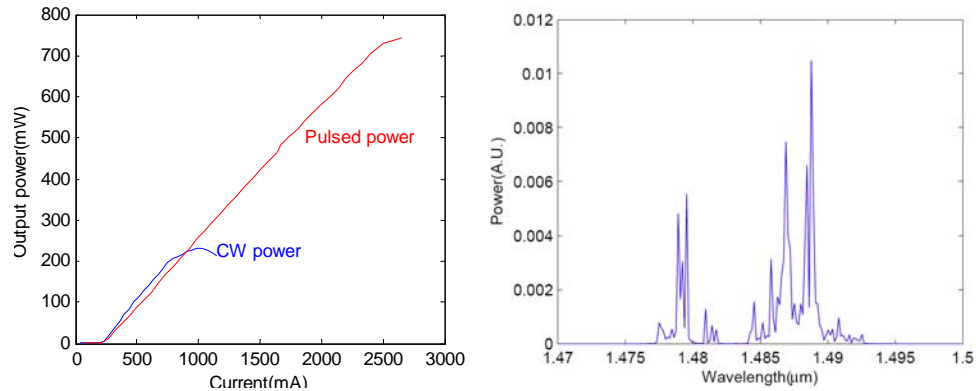


Figure 53 L-I curve and spectrum for 4th generation lasers

As the PL measurement is mostly sensitive to the defect density in the material, we believe the PL intensity improvements we achieved in the past were reductions in defect density. On the other hand, the defect density may not be the determining factor for the laser threshold, as shown in the following equation for threshold *current* density, J_{th} , as a function of the threshold *carrier* density, n_{th} .

$$J_{th} = A * n_{th} + B * n_{th}^2 + C * n_{th}^3 + Leakage$$

The first term represents the monomolecular recombination due to defects, and the second term represents spontaneous recombination. The third term represents Auger recombination, and the last term is the leakage current out of the QW, which has the following exponential dependence on the barrier height and the temperature.

$$Leakage \propto \exp(-E_{barrier} / kT)$$

GaNAs barrier used in our lasers were found to have relatively small band offset[13], so it is quite possible that there is significant leakage current. Auger recombination can also be a significant portion for GaInNAsSb lasers at around 1.48 μ m, as Auger recombination is known to get exponentially more severe as the wavelength becomes longer, and it is also a significant problem for InGaAsP/InP lasers at the same wavelength of 1.5 μ m[14]. Despite the possibility of significant leakage and Auger currents, we had been able to achieve improved laser thresholds by reducing defects in the GaInNAsSb material, but now it seems that defect-related recombination is no longer a dominant factor, and leakage and Auger currents have to be seriously considered for further improvement of lasers.

To corroborate this point, we grew and tested the two additional QW laser structures illustrated schematically in Fig. 54, in addition to our conventional single QW(SQW) laser structure. One was a triple QW structure, which can reduce the proportion of Auger recombination by reducing the required n_{th} per QW, and the other was a thinner-barrier QW with 10nm GaNAs instead of 20nm GaNAs, which could reduce the leakage and Auger problem by reducing the number of confined energy levels in the barrier.

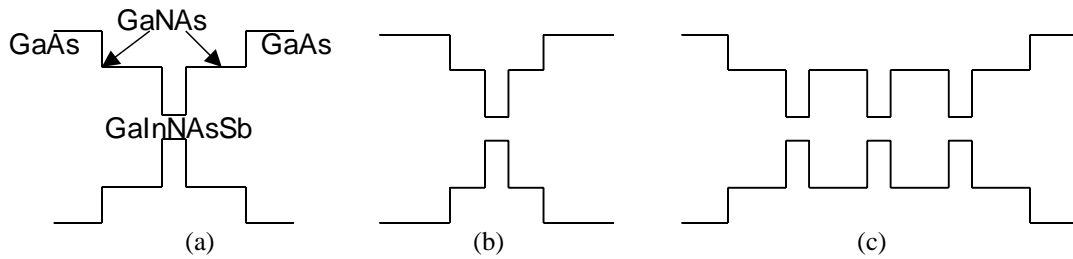


Figure 54 Schematics of 3 different QW structures
(a) SQW with 20nm GaNAs (b) SQW with 10nm GaNAs (c) 3QW

We measured the characteristic temperature, T_0 , which was found by fitting an exponential function to the threshold current density as a function of temperature T . It is known that defect recombination and spontaneous recombination lead to relatively high (200K or higher) T_0 values, whereas Auger and leakage recombination lead to low (100K or lower) T_0 values. Thus, the T_0 parameter can give us a valuable indication about the dominant recombination mechanism for the threshold current. T_0 is an important value in its own right, as it is a measure of temperature stability of the laser threshold. (Better temperature stability, or equivalently higher T_0 , is more desirable for high power CW-mode laser operation.)

$$J_{th} = J_0 \exp\left(\frac{T}{T_0}\right)$$

The T_0 value for SQW was quite low at 75K (Fig. 55a). This indicated the dominance of Auger recombination or leakage current. On the other hand, the 1st generation lasers showed quite high threshold density (1.06kA/cm^2) and a high T_0 of 135K, which implied that the 1st generation lasers were still somewhat limited by defect-related recombination. Subsequent PL intensity improvements reduced the defect recombination, and thus threshold current, except the last batch of improvements. Thus, we believe that our GaInNAsSb material had finally reached a stage where the defect density was no longer the limiting factor.

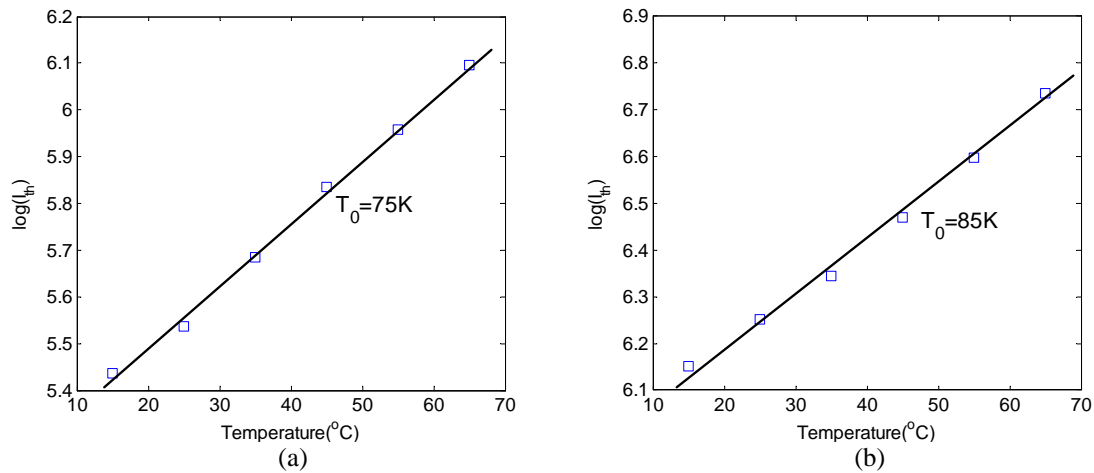


Figure 55 T_0 comparison for SQW vs 3QW lasers ([15])

The use of multiple QWs usually improves T_0 by reducing the threshold carrier density per QW. However, 3QWs were found to barely improve the T_0 , indicating that Auger and leakage processes were still dominant. The total threshold current density was also rather high at 1263A/cm^2 . On the other hand, the thinner-barrier QWs exhibited a little higher T_0 of 85K (Fig. 55b), but these came with a higher threshold (860A/cm^2). We believe the 10nm GaNAs layer was not sufficient to compensate the compressive strain in the GaInNAsSb layer and resulted in increased defects, leading to higher T_0 and higher J_{th} .

3. Summary and directions for future work on 1.48 μm laser diodes for in-band pumping of erbium-doped laser hosts

During the project years, we achieved record-low threshold room-temperature CW laser operation at 1.5 μm and 1.55 μm on GaAs substrates. The improvements mainly came from improving the GaInNAsSb material quality (i.e. reducing defect density) by better growth control. Our most recent laser results showed that material quality was no longer the limiting factor in the laser performance, and that future research should be directed towards reducing Auger and leakage problem rather than trying to further reduce defect density, as we have done in the past.

It is not yet clear whether it is Auger or leakage that is dominant, and further measurements are currently under way under different auspices to clarify that. In addition to these measurements, we plan to replace the GaNAs barrier material with another material that has high bandgap to suppress leakage, and a smaller lattice constant for strain compensation. GaPAs has such properties, and we recently installed a phosphorus source to the MBE chamber to embark on GaPAs barrier research in future programs. By using this new barrier material, we hope to remove the leakage problem and realize the full potential of the GaInNAsSb material, not limited by the low band-offset of the GaNAs barrier.

A second potential issue is the reliability of lasers that are deeply etched through the QWs. Although deep-etching reduced the threshold, the exposed QW can be a source of early degradation under high power CW operation. The reliability of deep-etched lasers needs to be measured and compared with shallow etched lasers, and if deep-etched lasers show poorer reliability, surface passivation will need to be considered.

Maximum output power over 700mW in pulsed mode and over 200mW in CW mode has been routinely achieved from 20 μm -wide facets through many generations of our GaInNAsSb lasers. As they were all mounted epi-side up, the output power can be enhanced significantly by mounting the lasers epi-down and removing heat through the 2 μm -thick upper cladding instead of the 120 μm -thick substrate.

References

- [1] M. Kondow, T. Kitatani, S. Nakamura, M. C. Larson, K. Nakahara, Y. Yazawa, M. Okai, and K. Uomi, "GaInNAs: a novel material for long-wavelength semiconductor lasers," IEEE JSTQE **3**, 7190 (1997).
- [2] D. Jackrel, H. Yuen, S. Bank, J. Fu, X. Yu, Z. Rao, J. Harris, "MBE grown GaInNAs solar cells for multijunction applications," Proceedings, 31st IEEE PVSC, 854 (2005).
- [3] X. Yang, M. J. Jurkovic, J. B. Heroux, W. I. Wang, "Molecular beam epitaxial growth of InGaAsN:Sb/GaAs quantum wells for long-wavelength semiconductor lasers," Appl. Phys. Lett. **75**, p. 178-180 (1999).
- [4] V. Gambin, W. Ha, M. Wistey, H. Yuen, S. R. Bank, S. M. Kim, and J. S. Harris Jr., "GaInNAsSb for 1.3-1.6 μm long wavelength lasers grown by molecular beam epitaxy," IEEE JSTQE, **8**, p. 795-800 (2002).
- [5] S.R. Bank, M.A. Wistey, H.B. Yuen, L.L. Goddard, W. Ha, and J.S. Harris, "Low-threshold CW GaInNAsSb/GaAs Laser at 1.49 μm ," Elec. Lett., **39**, no. 20, p.1445-6 (2003).

- [6] M.A.Wistey, S.R.Bank, H.B.Yuen, H. **Bae**, J.S. Harris, "Nitrogen plasma optimization for high-quality dilute nitrides", *Journal of Crystal Growth* **278** (1-4), p.229-33 (2005).
- [7] S.R. Bank, M.A. Wistey, H.B. Yuen, L.L. Goddard, H.P. **Bae**, J.S. Harris, "Molecular Beam Epitaxy Growth of Low-Threshold CW GaInNAsSb Lasers at 1.5 μ m," *J. of Vac. Sci. Technol. B*, **23**(3), 1337 (2005).
- [8] S. R. Bank, H. P. Bae, H. B. Yuen, L. L. Goddard, M. A. Wistey, T. S. Sarmiento, J. S. Harris Jr., "Low-threshold CW 1.55 μ m GaAs-based lasers", OFC (2006).
- [9] S. R. Bank, H. B. Yuen, H. P. Bae, M. A. Wistey, and J. S. Harris Jr., "Over-Annealing Effects in GaInNAs(Sb) Alloys and Their Importance to Laser Applications," *Appl. Phys. Lett.*, **88**, no. 22, 221115 (2006).
- [10] S. R. Bank, H. B. Yuen, H. P. Bae, M. A. Wistey, A. Moto, and J. S. Harris Jr., "Enhanced Luminescence in GaInNAsSb Quantum Wells Through Variation of the Arsenic and Antimony Fluxes," *Appl. Phys. Lett.*, **88**, no. 24, p. 231923 (2006).
- [11] H. P. Bae, S. R. Bank, M. A. Wistey, H. B. Yuen, E. Pickett, T. Sarmiento, J. S. Harris Jr., "Investigation of GaInNAsSb annealing processes and its implications on GaInNAsSb lasers", Session F6, EMC (2006).
- [12] H. P. Bae, S.R. Bank, H. B. Yuen, T. Sarmiento, E. R. Pickett, M. A. Wistey, J. S. Harris Jr., "Temperature dependencies of annealing behaviors of GaInNAsSb/GaNAs quantum wells for long wavelength dilute-nitride lasers", *Appl. Phys. Lett.*, **90**, 231119 (2007).
- [13] R. Kudrawiec, S.R. Bank, H.B. Yuen, H. **Bae**, M.A. Wistey, L.L. Goddard, J.S. Harris, Jr., M. Gladysiewicz, M. Motyka, J. Misiewicz, "Conduction band offset for Ga_{0.62}In_{0.38}N_xAs_{0.991-x}Sb_{0.009}/Ga_yAs_{1-y}/GaAs systems with the ground state transition at 1.5–1.65 μ m," *Appl. Phys. Lett.* **90**, 131905 (2007).
- [14] E. P. O'Reilly, M. Silver, "Temperature sensitivity and high temperature operation of long wavelength semiconductor lasers", *Appl. Phys. Lett.* **63**, 3318, (1993).
- [15] H. Bae, T. Sarmiento, J.S. Harris, "Experimental investigation of temperature dependence of 1.55 μ m GaInNAsSb/GaNAs QW lasers grown in MBE", International Semiconductor Laser Conference, Sorrento, Italy, Sept.2008.

V. Optical Parametric Generation in QPM-GaAs

P.S. Kuo, K.L. Vodopyanov, M.M. Fejer

1. Introduction

As part of the objective of frequency conversion to 1.5 or 2.0 microns for eye-safe defense sensing applications, we are exploring different possibilities for the choice of nonlinear optical media. Materials with zincblende structure (ZnS, ZnSe, AlGaAs, GaP, GaAs) appear to be very promising candidates for generating new frequencies via three-wave processes. In this period, we investigated the polarization dependence of the optical parametric generator we reported last year.

2. Progress

2.1 Background

Gallium arsenide (GaAs) has excellent characteristics for parametric frequency conversion and is potentially one of the most attractive mid-IR nonlinear-optical materials. It has an extremely large second-order nonlinear optical coefficient, wide transparency range, excellent mechanical properties and high thermal conductivity [1]. The linear and nonlinear optical properties of GaAs are compared with those of other zincblende semiconductors in Table 1.

Table 1 Some linear and nonlinear optical properties of zincblende semiconductors [1,2]

Crystal	Transparency range (μm)	d_{eff}^* (pm/V)	Average refractive index	NLO FOM d_{eff}^2/n^3 with respect to PPLN
GaAs	0.9-17	$2/\pi \cdot 94 = 60$	3.3	6.2
GaP	0.51-7.2	$2/\pi \cdot 37 = 23.6$	3.05	2.30
ZnSe	0.51-18	$2/\pi \cdot 26.4 = 16.8$	2.44	0.93

* The $2/\pi$ factor represents the fact that the crystal can only be quasi-phase-matched

The phase-matching problem arising from the optical isotropy of zincblende-type semiconductors can be solved by spatially modulating the optical nonlinearity (i.e. quasi-phasing). Unfortunately, zincblende-type semiconductors are not ferroelectric and no techniques analogous to electric field poling in LiNbO_3 exist for inducing a quasi-phase-matching domain grating in an already grown crystal - domain reversal should be incorporated into the crystal growth process.

Recently, an all-epitaxial process for fabrication of orientation patterned (domain-inverted) GaAs structures has been developed [3-5], and has been applied for making structures for nonlinear-optical applications. The orientation patterned GaAs (OP-GaAs) films were fabricated by a multi-step process illustrated in Figure 56.

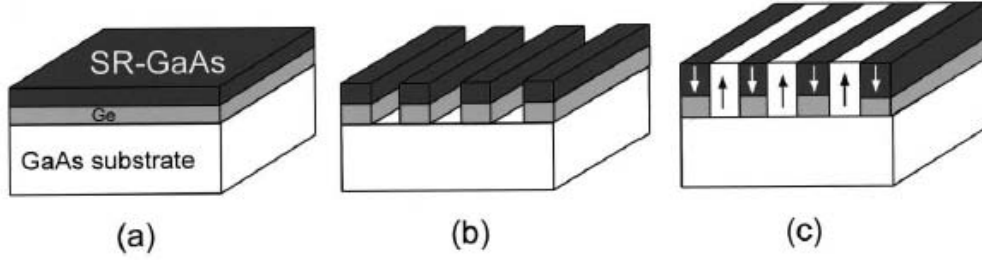


Figure 56 Fabrication process of OP-GaAs films. (a) First, GaAs/Ge/GaAs heteroepitaxy is used to create a sublattice-reversed (SR) GaAs layer on a GaAs substrate. (b) Then the wafer is patterned, using photolithography and wet chemical etching, to create an orientation template with the period determined by a specific QPM process. (c) This template then undergoes two epitaxial growth steps (molecular beam epitaxy (MBE) and hydride vapor phase epitaxy (HVPE)) to produce thick OP-GaAs film.

In this fashion, OP-GaAs layers can be grown to a thickness of 0.5 mm and length of up to 2 cm with excellent optical quality. Figure 57 shows the polished cross section of an OP-GaAs sample with the QPM period of 61 μm . Skauli et al. [2] demonstrated an

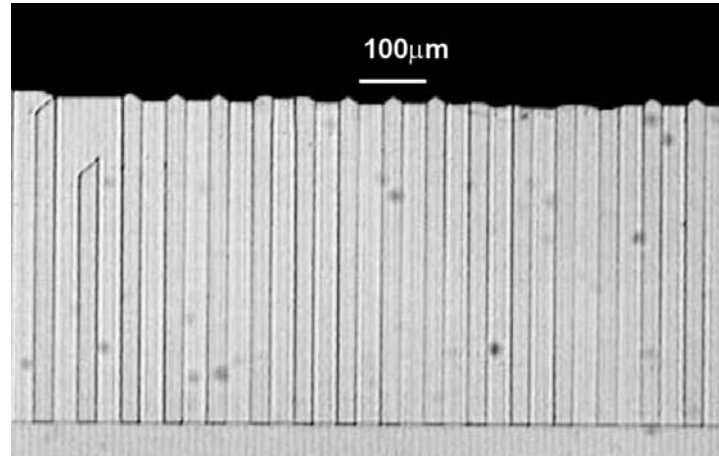


Figure 57 Cross section of an OP-GaAs sample with the QPM period of 61 μm .

efficient 4 $\mu\text{m} \rightarrow 2 \mu\text{m}$ frequency doubling in OP-GaAs with >30% internal efficiency at pump pulse energies of only 50 μJ . In the past several years, using OP-GaAs, difference frequency generation [6] and an efficient OPO tunable from 2-11 μm [7-8] have been demonstrated.

2.1 Recent developments

In the prior period, we reported on demonstration of optical parametric generation (OPG) in OP-GaAs. Using picosecond-duration pulses at 3.28 μm wavelength, an octave-wide spectrum was generated that spanned from 4.5 μm to 10.7 μm at 20 dB from peak, and the threshold for OPG was at 55 nJ (see Fig. 58).

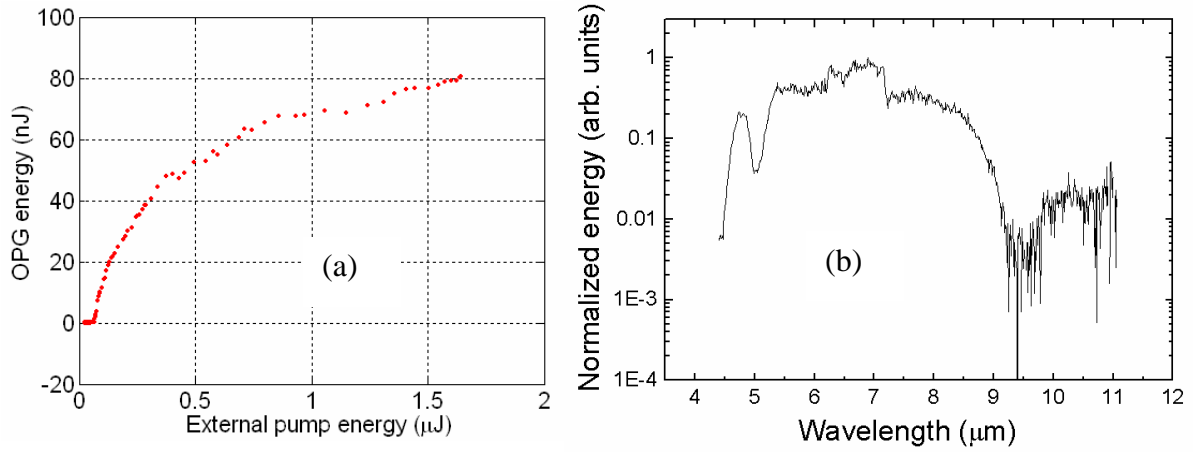


Figure 58 a) OP-GaAs OPG power curve b) OPG spectrum at 1.4 μJ pumping at 3.28 μm

We also explored the dependence on the pump polarization of an optical parametric oscillator (OPO) or OPG based on OP-GaAs. Because of the high symmetry in the nonlinear susceptibility tensor of GaAs (which has only three nonzero elements, $d_{14} = d_{25} = d_{36} = d_{xyz}$) and isotropy in its refractive index, OP-GaAs can be pumped with a wide variety of pump polarizations. In OP-GaAs, the waves typically propagate along the $[-110]$ crystallographic direction such that the electric fields of the interacting waves all lie in the plane containing $[001]$, $[110]$ and $[111]$. GaAs allows pumping of an OPO or optical parametric generator with linearly and circularly polarized light as well as depolarized light. Figure 59 plots the expected effective nonlinear coefficient (d_{eff}) for an OPG/OPO-type interaction for a linearly polarized pump as a function of the angle of the pump to the $[110]$ direction. We see that d_{eff} is maximized when the pump is polarized along $[111]$ (with a value of $d_{\text{eff}} = \frac{2}{\sqrt{3}}d_{14}$), and that $d_{\text{eff}} \geq d_{14}$ for all linear polarizations.

For a circularly polarized pump, we expect $d_{\text{eff}} = \frac{1+\sqrt{5}}{2\sqrt{2}}d_{14}$, which is nearly as large as

pumping with $[111]$ -linearly polarized light. If we examine the case where the pump is linearly polarized along $[110]$, we find that $d_{\text{eff}} = d_{14}$ is a constant for all signal polarizations so long as the idler wave is complementarily polarized. Thus, OP-GaAs can be used as a polarization-insensitive optical parametric amplifier, which may be of interest for WDM networks or photon-counting detectors. Since the indices of the nonlinear tensor can be permuted, we infer that an OP-GaAs OPO or OPG can be pumped with depolarized or unpolarized light, if the signal wave is fixed with $[110]$ polarization and the idler is complementarily polarized to the pump.

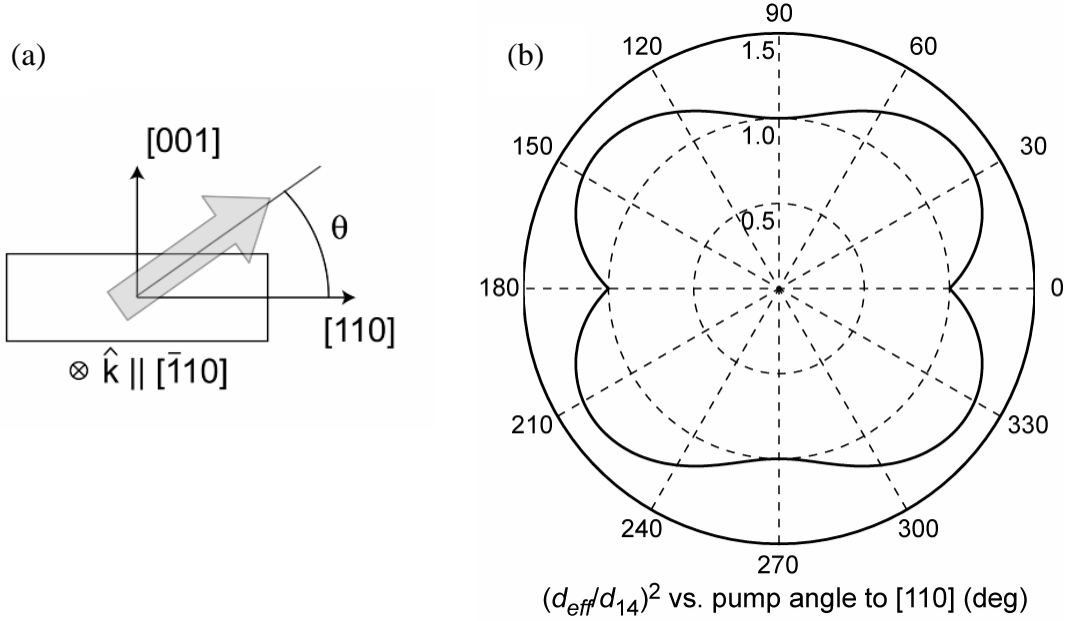


Figure 59 a) Sketch of propagation geometry in GaAs b) Relative gain, expressed as $(d_{\text{eff}}/d_{14})^2$, as a function of angle to the [110] direction for a linearly polarized pump

The capability of OP-GaAs to convert or amplify non-polarized light can be an interesting tool towards the generation of tunable, high power, coherent radiation. High-power, non-polarized lasers can be efficiently converted to different wavelengths. It should be noted that related nonlinear optical zincblende crystals, like GaP and ZnSe, also have this property. However, GaP and ZnSe both have bandgaps in the visible wavelength range and can therefore be pumped with 1- μm wavelength fiber lasers. GaAs unfortunately cannot be pumped at 1- μm wavelength because it suffers from residual band tail and two-photon absorption at that wavelength, and therefore must be pumped with 1.5- μm , 2- μm or longer wavelength lasers.

We explored pumping both an OP-GaAs OPG and OPO with various polarizations. Figure 60 plots OPG energy curves for three different pump polarizations, [001]- and [111]-linear polarizations and circular polarization. We observed almost equal thresholds for the circular and [111]-linear polarizations, which were both lower than the threshold for the [001]-linearly polarized pump. Since OPG is an exponential process where small differences in pump power are magnified in generated power, it is hard to do more than qualitative comparisons of the different cases. We note that we expected the [111]-linear polarized pump to have lower threshold than the circularly polarized pump. This slight discrepancy may be due to misalignment of the linearly polarized pump to the [111] direction, or some higher order nonlinear effect (like $\chi^{(3)}$ or n_2) favoring the circularly polarized pump. With picosecond-duration pulses, the intensity associated with $\sim 100\text{nJ}$ pulses is large enough to cause measurable n_2 effects, like self-phase modulation. Hutchings and Wherrett [9] have noted that the magnitude of n_2 is different for linear polarization compared to circular polarizations. Perhaps the interaction between n_2 and OPG causes the circularly polarized pump to have lower OPG threshold.

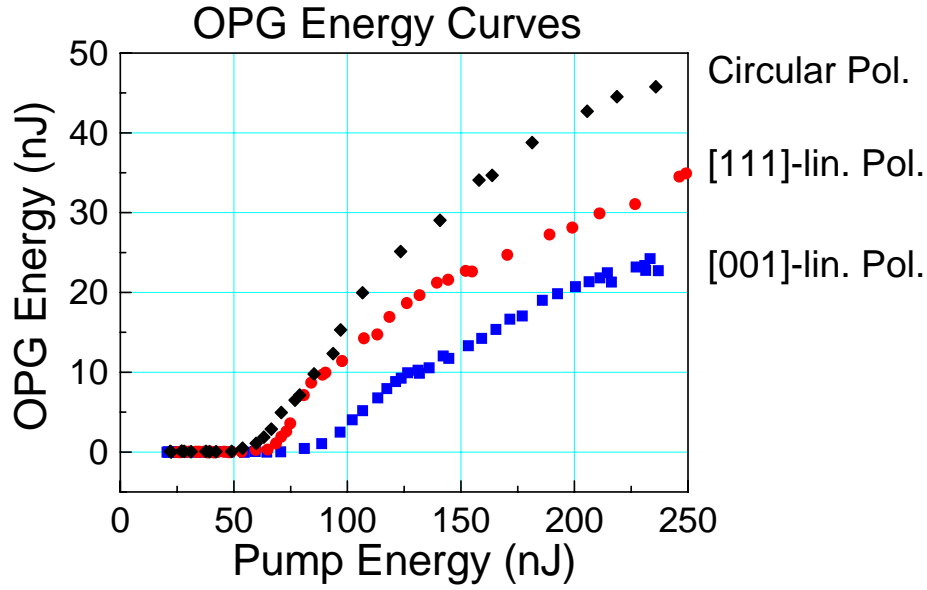


Figure 60 OP-GaAs optical parametric generation energy curves for three different pump polarizations.

We also studied the pump polarization dependence of an OP-GaAs optical parametric oscillator. The OPO threshold is a linear function of the gain (unlike OPG, which depends exponentially on the gain), so we can perform quantitative studies on the pump polarization dependence. We constructed an OP-GaAs OPO pumped with ns-duration pulses. The experimental setup is sketched in Fig. 61 on the next page. The OP-GaAs sample was 11-mm long, 6-mm wide, 600- μm thick and had 130- μm QPM period. The sample was pumped with 2.79- μm wavelength, 26-ns duration pulses with energy up to 65 μJ from a periodically poled LiNbO₃ (PPLN) OPO that was in turn pumped with a Q-switched Nd:YAG laser (Spectra-Physics X30-106Q laser, 1.064- μm , 1.3-mJ at 100-Hz repetition rate). The linewidth of the PPLN OPO spectrum was narrowed with an intracavity 40- μm thick YAG etalon to 6-nm FWHM in order to better match the pump acceptance bandwidth of the OP-GaAs OPO. After filtering out shorter wavelengths produced by the PPLN OPO, the linearly polarized 2.79- μm wavelength pulses were attenuated with pair of GaAs Brewster plates and then focused in the OP-GaAs with a BaF₂ lens to a 125- μm $1/e^2$ -intensity radius spot. The pump was double-passed in the OP-GaAs OPO, whose cavity consisted of a metal mirror (500-mm ROC) and a flat dielectric mirror that reflected the signal around 4.8 μm and transmitted the pump and idler around 6.7 μm . A dielectric beamsplitter (HR around 2.8 μm and HT from 4.5 to 8 μm) separated the pump from the signal and idler waves of the OP-GaAs OPO. The OP-GaAs crystal was coated with a broadband anti-reflection coating with low reflectivity at the signal ($R < 1\%$) and idler ($R < 3\%$) and modest reflectivity at the pump ($R \sim 20\%$). The output of the OP-GaAs OPO was detected with an amplified pyroelectric detector preceded by a 4- μm cutoff long pass filter.

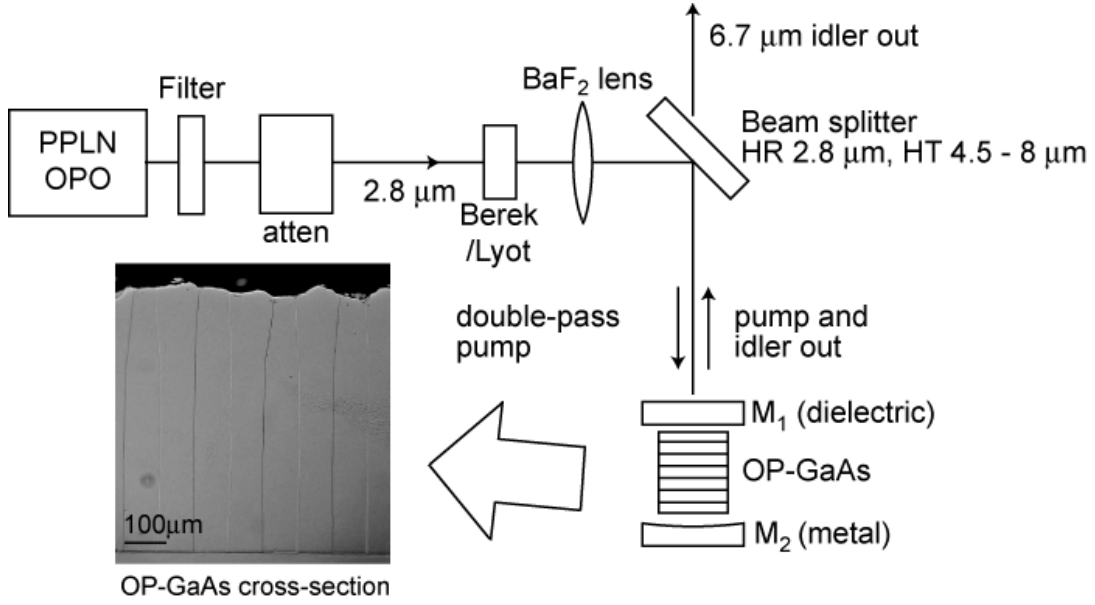


Figure 61 Experimental setup for ns-duration OP-GaAs OPO.

To change the orientation of the linear pump polarizations relative to the OP-GaAs crystal, the sample was rotated in the pump beam. The linearly polarized pulses from the PPLN OPO were converted to circular polarization using a quarter-wave plate formed with a MgF₂ Berek compensator (New Focus Model 5540). To produce pseudo-depolarized pump pulses, the output of the PPLN OPO was passed through a Lyot depolarizer consisting of a 75-mm long LiNbO₃ (LN) crystal oriented such that the light propagated with its k-vector orthogonal to the z-axis and its polarization at 45° to the principal birefringence axes. The LN crystal was sufficiently long such that the group delay between the two principal polarizations was much larger than the coherence time of the pump pulses, which effectively scrambled the polarization of the light. In order to avoid the need to refocus the pump, the LN crystal was left in the pump beam throughout the experiment and simply rotated between 0° and 45° to pass linearly polarized or produce pseudo-depolarized light.

Figure 62 plots the energy curves for the OP-GaAs OPO for [001]-, [110]-, [111]-linearly and circularly polarized pumps. From these curves, we estimated threshold for the [111]-linearly polarized pump to be at 30 μJ while the thresholds for both the [001]- and [110]-linearly polarized pumps were at 41 μJ. The observations that the [001]- and [110]-polarized-pump cases were equal and that the [111]-polarized pump threshold energy was 3/4 the size of the [001]-polarized case agree very well with theory since the OPO threshold energy is proportional to $1/\text{gain} \propto 1/d_{\text{eff}}^2$. The threshold for the circularly polarized pump was about 29 μJ, which was slightly lower than the threshold for the [111]-linearly polarized pump. From calculations, we expected the circularly polarized pump to have slight higher threshold than the [111]-linearly polarized case; the discrepancy in experimental results may be attributed to uncertainty in the alignment of the linearly polarized pump to the [111] direction.

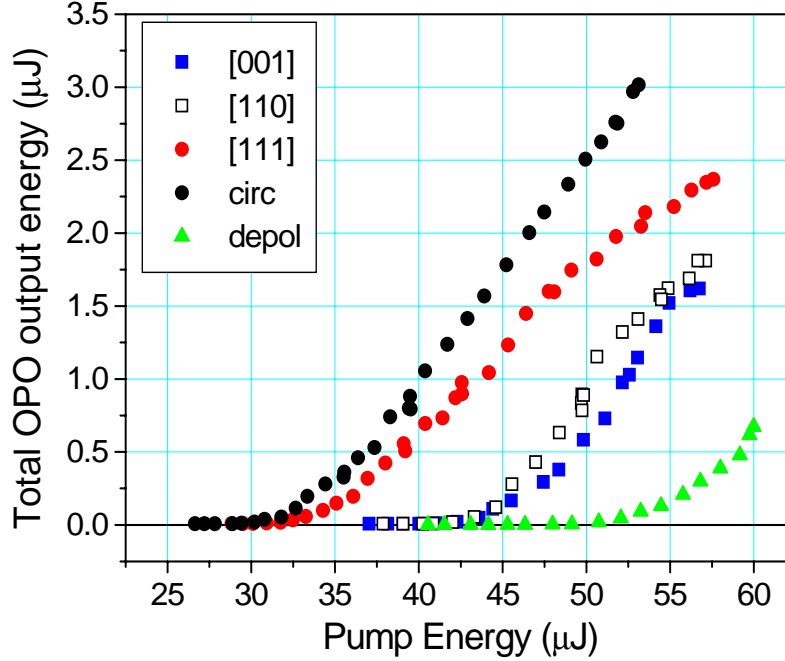


Figure 62 OP-GaAs OPO energy curves for [001]-, [110]-, and [111]-linearly polarized pumps, as well as circularly polarized and pseudo-depolarized pumps

The OPO energy curve for the pseudo-depolarized pump is also plotted in Figure 7. We observed threshold for the depolarized pump at 50 μJ , which was only 22% higher than the threshold for the [001]-linearly polarized pump and only 67% larger than the [111]-polarized case. Also, at 55 μJ pump energy (10% above threshold), we observed parametric oscillation for every pump pulse. Since the threshold for the depolarized pump is less than twice larger than that for the linearly polarized pump cases, we conclude that this is the first OPO to be pumped in a nontrivial way with a depolarized source.

In the final program year, we investigated pumping an OP-GaAs OPO with 1.55- μm wavelength lasers. GaAs suffers from two-photon absorption (TPA) at wavelengths shorter than $\sim 1.7 \mu\text{m}$, but since TPA is a nonlinear effect, it should be small at low intensities. For the same average intensity, continuous-wave (CW) lasers have less peak intensity than pulsed lasers, and therefore, we expected much less TPA when using a CW pump laser than a pulsed laser.

While the performance of a 1.55- μm wavelength pumped OP-GaAs OPO was definitely affected by TPA, a more significant limitation has been the material quality itself. Short-wavelength pumping requires short QPM periods. For 1.55 μm pumping, the OP-GaAs periods are required to be in the 30 - 40 μm range. Our collaborators at Hanscom Air Force Base have been able to grow increasingly thicker OP-GaAs samples with smaller periods. Figure 63 is a photograph of a stain-etched cross-section of a recent sample having 30 μm QPM period that was approximately 900 μm thick. Many QPM domains propagated almost to the top of the sample, but domain tapering and annihilation were still observed. None-the-less, the optical losses in this sample were measured to be less

than 0.005 cm^{-1} at both 1.55 and $2.015 \text{ }\mu\text{m}$, and we decided to use this sample, and others from the same growth run with periods ranging from 27 to $40 \text{ }\mu\text{m}$, to build a $1.55\text{-}\mu\text{m}$ pumped OP-GaAs OPO.

We designed a four-mirror, ring OPO cavity for the OP-GaAs. The ring geometry allowed only a single pass of the resonated wave through the crystal per round trip, thereby minimizing losses caused by the crystal and its coatings. We used a pair of 30mm

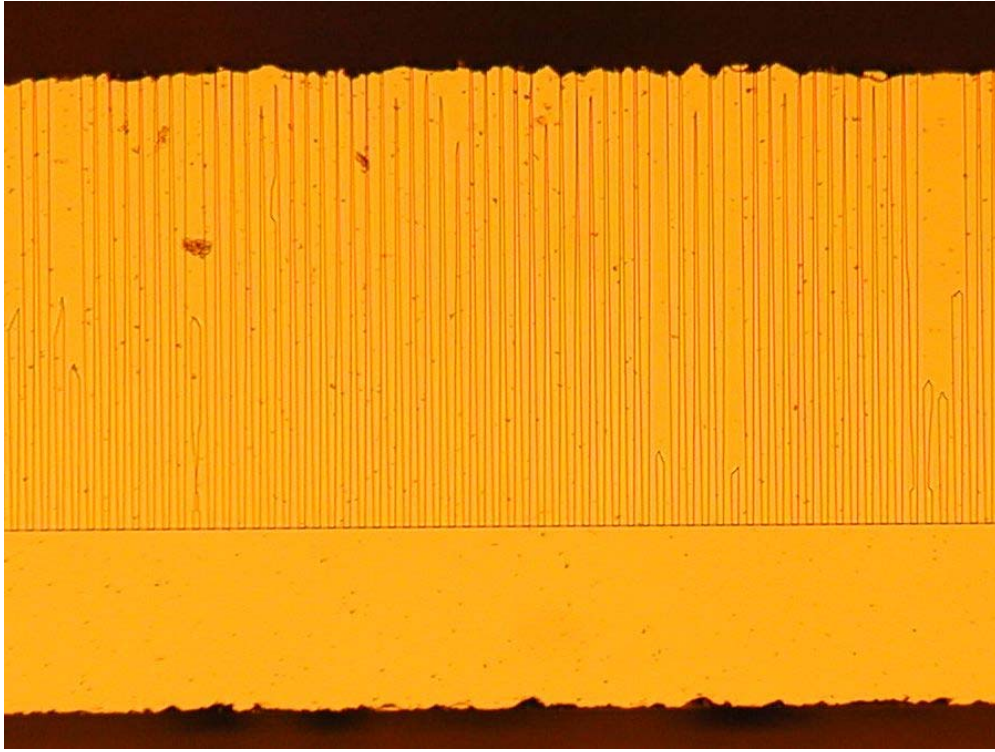


Figure 63 Stain-etched cross-section of a $900\text{-}\mu\text{m}$ thick, $30\text{-}\mu\text{m}$ period OP-GaAs sample. This and other similar samples were used in an OP-GaAs CW OPO pumped at $1.55 \text{ }\mu\text{m}$.

ROC mirrors to focus the signal tightly in the OP-GaAs. The OPO cavity was designed to support a $36\text{-}\mu\text{m}$ $1/e^2$ intensity radius signal beam, which was a little bit tighter than confocal focusing for our 32-mm long OP-GaAs samples.

The $1.55\text{-}\mu\text{m}$ wavelength pump was focused to a $40\text{-}\mu\text{m}$ intensity radius spot by an external mirror. The OP-GaAs QPM period was chosen to be $35 \text{ }\mu\text{m}$ to phasematch the process $1.55 \text{ }\mu\text{m} \rightarrow 2.0\text{ }\mu\text{m} + 6.7 \text{ }\mu\text{m}$. Using a telecom seed laser and an erbium-doped fiber amplifier, we produced up to 16 W of quasi-CW light at $1.55 \text{ }\mu\text{m}$. However, this amount of pump power was not sufficient to produce oscillation in the OP-GaAs OPO. It was concluded that either the loss in the sample was too high, or the signal gain was too low. Both can be attributed to insufficient material quality. We investigated the gain the sample by inserting a $2.015\text{-}\mu\text{m}$ wavelength CW probe laser and searching for parametric amplification of the $2\text{-}\mu\text{m}$ beam caused by the $1.55 \text{ }\mu\text{m}$ pump. We chopped the $1.55 \text{ }\mu\text{m}$ pump beam and looked for modulation on the $2\text{-}\mu\text{m}$ probe beam using a lock-in amplifier

and oscilloscope. Through these measurements, we observed modulation of the 2- μm probe caused by the pump, but upon close inspection, we discovered that the presence of the pump was not causing amplification but rather attenuation of the 2- μm beam.

We tuned the pump wavelength and varied the pump power to further investigate the interaction between the 1.55- μm pump and 2.015- μm probe. Figure 64 plots the magnitude of the observed modulation of the 2- μm beam caused by the 1.55- μm beam. The pump wavelength was scanned from 1541.5 to 1546.5 nm at four different pump powers. The filled circles represent measured data. Most of the modulation signal came from attenuation of the probe caused by the pump, an effect that we call “pump-induced probe absorption” (PIPA). All data showed a decrease in signal strength around 1543.7 nm, which we attributed to optical parametric amplification (OPA). Since the OPA process is quasi-phases-matched, it has a signature spectral shape that is determined by the GaAs dispersion function. Along the x-axis, we have plotted the theoretical OPA curve (in positive units of modulation, black solid line). We see that the location of the dip is very close to the expected location of OPA phase-matching. The width of the dip is seen to be broader than the width of the OPA curve (solid line), but if the effective length of the nonlinear crystal is reduced by a factor of three (dashed line), the widths of the features become close in magnitude.

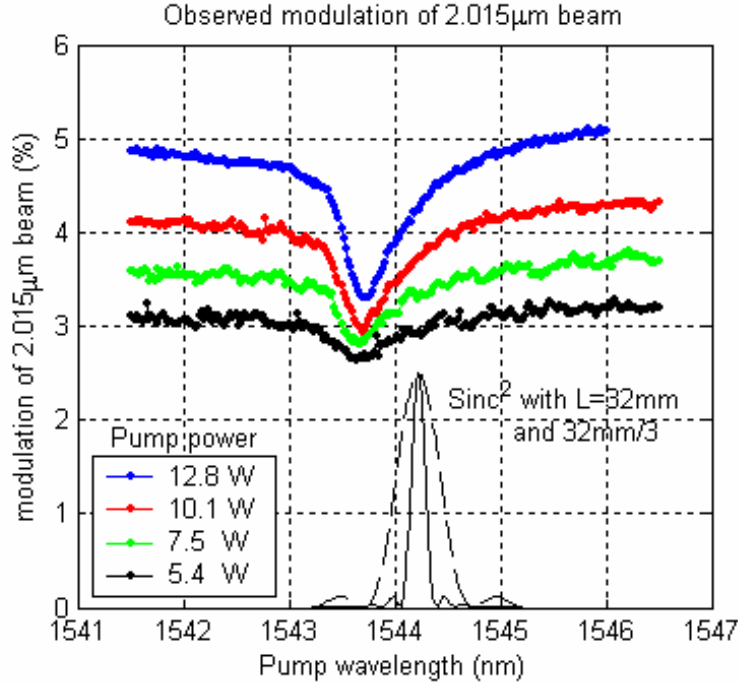


Figure 64 Modulation of the 2.015- μm probe beam caused by the 1.55- μm pump

Figure 64 also shows that the PIPA and OPA vary differently with pump power. The wings of the curves (associated with PIPA), change more slowly with pump power than the magnitude of the dip in the OPA signal. Also, we see that the dip never goes to zero modulation, which implies that the gain in the OP-GaAs crystal never exceeds the loss at these pump powers. We conclude that for this particular OP-GaAs crystal, parametric oscillation is not possible because of the excessive amount of induced loss from PIPA.

We also carried out a wavelength scan in a portion of the sample without the QPM grating, and we saw no dependence on pump wavelength, which further confirmed that the dip is caused by quasi-phasematched OPA.

3. Directions for future research on OP-GaAs devices

The results of these studies were disappointing from an immediate practical device point-of-view, but they did indicate important areas of research that still need to be explored in order to develop orientation-patterned GaAs as a widely applicable, nonlinear optical material. The cause of the pump-induced probe absorption needs to be determined in follow-on studies. We hypothesize that it may be due to unidentified deep levels or impurities in the GaAs, or that it may be tied to the free-carrier concentration. It is recommended that future work focus on a systematic study of PIPA in GaAs samples of varying free-carrier concentrations. It will also be important to determine whether PIPA is caused by longer-wavelength pumps. At this point in time, high-power, near-IR pumping of OP-GaAs remains very attractive, but it will require solving the problem of pump-induced probe absorption in this material.

The difficulties we encountered in pumping bulk OP-GaAs suggest that waveguide devices that operate at low powers may be of greater interest, especially in the near-infrared wavelength range. OP-GaAs waveguide work has been ongoing at Stanford. The losses in OP-GaAs waveguides have decreased significantly over the years as the corrugation of the template has been decreased [10]. Also, there has been increased interest in nonlinear mixing in GaAs microdisk resonators [11], which may facilitate low-power devices that have applications in spectroscopy and quantum computing

References

- [1] T. Skauli, K. L. Vodopyanov, T. J. Pinguet, A. Schober, O. Levi, L.A. Eyres, M. M. Fejer, J. S. Harris, B. Gerard, L. Becouarn, E. Lallier, "Measurement of nonlinear coefficient of orientation-patterned GaAs and demonstration of highly efficient second harmonic generation", *Opt. Lett.* 27, 628-630 (2002)
- [2] E.D. Palik, "Handbook of Optical Constants of Solids", Academic Press, Orlando, 1985.
- [3] L.A. Gordon, G.L. Woods, R.C. Eckardt, R.R. Route, R.S. Feigelson, M.M. Fejer, and R.L. Byer, "Diffusion-bonded stacked GaAs for quasi-phase-matched second-harmonic generation of a carbon dioxide laser," *Electron. Lett.* 29, 1942-1944 (1993)
- [4] C.B. Ebert, L.A. Eyres, M.M. Fejer, and J.S. Harris, "MBE growth of antiphase GaAs films using GaAs/Ge/GaAs heteroepitaxy," *J. Cryst. Growth* 201, 187-193 (1999)
- [5] S. Koh, T. Kondo, M. Ebihara, T. Ishiwada, H. Sawada, H. Ichinose, I. Shoji, and R. Ito, "GaAs/Ge/GaAs sublattice reversal epitaxy on GaAs (100) and (111) substrates for nonlinear optical devices," *Jpn. J. Appl. Phys.* 38, L508-L511 (1999)
- [6] L.A. Eyres, P.J. Tourreau, T.J. Pinguet, C.B. Ebert, J.S. Harris, M.M. Fejer, L. Becouarn, B. Gerard, and E. Lallier, "All-epitaxial fabrication of thick, orientation-patterned GaAs films for nonlinear optical frequency conversion," *Appl. Phys. Lett.* 79, 904-906 (2001)
- [7] L. A. Eyres, All-epitaxial orientation-patterned semiconductors for nonlinear optical frequency conversion, PhD Thesis, Stanford University, December 2001

- [8] O. Levi, T.J. Pinguet, T. Skauli, L.A. Eyres, K.R. Parameswaran, J.S. Harris, M.M. Fejer, T.J. Kulp, S.E. Bisson, B. Gerard, E. Lallier, L. Becouarn "Difference frequency generation of 8- μ m radiation in orientation-patterned GaAs", Opt. Lett. 27, 2091-2093 (2002)
- [9] D.C. Hutchings and B.S. Wherrett, "Theory of the anisotropy of ultrafast nonlinear refraction in zinc-blende semiconductors," Phys. Rev. B 52, 8150 (1995)
- [10] Xiaojun Yu; Scaccabarozzi, L.; Lin, A.C.; Fejer, M.M.; Harris, J.S., "Growth of GaAs with orientation-patterned structures for nonlinear optics", Journal of Crystal Growth (April 2007) vol.301-302, p.163-7, and references therein
- [11] Andronico, A.; Favero, I.; Leo, G., "Difference frequency generation in GaAs microdisks", Optics Letters (15 Sept. 2008) vol.33, no.18, p.2026-8

VII. Publications and Proceedings

1. Refereed Publications

2008

[Lee 2008-2]

Yin-Wen Lee, Michel J. F. Digonnet, Supriyo Sinha, Karel E. Urbanek, Robert L. Byer, and Shibin Jiang, "High-Power Yb³⁺-Doped Phosphate Fiber Amplifier," to be published in *IEEE Journal of Quantum Electronics*.

[Wong 2008-1]

Wong, S.T., Plettner, T., Vodopyanov, K.L., Urbanek, K., Digonnet, M.J.F., Byer, R.L., "Self phase-locked degenerate femtosecond optical parametric oscillator," *Optics Letters*, **Vol. 33**, Issue 16, pp. 1896-1898 (August 15, 2008).

[Sinha 2008-1]

Sinha, S., Urbanek, K.E., Hum, D.S., Digonnet, M.J.F., Fejer, M.M., Byer, R.L., "Linearly polarized 3.35W narrow-linewidth, 1150nm fiber master oscillator power amplifier for frequency doubling to the yellow," *Optics Letters*, **Vol. 32**, Issue 11, pp. 1530-1532 (June 1, 2008).

[Lee 2008-1]

Lee, Y.W., Sinha, S., Digonnet, M.J.F., Byer, R.L., Jiang, S., "Measurement of high photo-darkening resistance in heavily Yb³⁺-doped phosphate fibers," *Electronics Letters*, **Vol. 44**, Issue 1, pp. 14-16 (2008).

[Ramirez 2008-1]

Ramirez, M.O., Wisdom, J, Li, H., Aung, Y.L., Stitt, J., Byer, R.L. et al., "Three-dimensional grain boundary spectroscopy in transparent high power ceramic laser materials," *Optics Express*, **Vol. 16**, Issue 9, pp. 5965-5973 (April 28, 2008).

2007

[Sridharan 2007-1]

Sridharan, A.K., Saraf, S., Byer, R.L., "Yb:YAG Master Oscillator Power Amplifier for Remote Wind Sensing," *Applied Optics*, **Vol. 46**, Issue 30, pp. 7552-7565 (October 20, 2007).

[Sinha 2007-2]

S. Sinha, K. E. Urbanek, D. S. Hum, M. J. F. Digonnet, M. M. Fejer and R. L. Byer, "Linearly Polarized 3.35-W Narrow-Linewidth, 1150-nm Fiber Master Oscillator Power Amplifier for Frequency Doubling to the Yellow", *Opt. Lett.*, Vol. **32**, No.11, pp. 1530-1532 (2007). <http://www.stanford.edu/~rlbyer/2007/428.pdf>

[Sinha 2007-1]

S. Sinha, K. E. Urbanek, A. Krzywicki, and R. L. Byer, "Investigation of the suitability of silicate bonding for facet termination in active fiber devices", *Opt. Express* Vol. **15**, No. 20, pp. 13003-13022 (2007). <http://www.stanford.edu/~rlbyer/2007/429.pdf>

[Saraf 2007-1]

Saraf, S., Byer, R.L., King, P.J., "High-extinction-ratio Resonant Cavity Polarizer for Quantum-optics Measurements", *Applied Optics*, Vol. **46**, No. 18, pp. 3850-3855. June 20, 2007. <http://www.stanford.edu/~rlbyer/2007/426.pdf>

[Hum 2007-1]

Hum, D.S., Route, R.K., Miller, G.D., Kondilenko, V., Alexandrovski, A., Huang, J., Urbanek, K., Byer, R.L., Fejer, M.M., "Optical Properties and Ferroelectric Engineering of Vapor-transport-Equilibrated, Near-Stoichiometric Lithium Tantalate for Frequency Conversion", *Journal of Applied Physics*, Vol. **101**, No. 9, pp. 093108, May 1, 2007. <http://www.stanford.edu/~rlbyer/2007/425.pdf>

[Kudrawiec 2007-1]

R. Kudrawiec, S. R. Bank, H. B. Yuen, H. Bae, M. A. Wistey, L. L. Goddard, and James S. Harris, Jr. "Conduction band offset for $\text{Ga}_{0.62}\text{In}_{0.38}\text{N}_x\text{As}_{0.991-x}\text{Sb}_{0.009}/\text{GaN}_y\text{As}_{1-y}/\text{GaAs}$ systems with the ground state transition at 1.5–1.65 μm ," *Appl. Phys. Lett.* **90**, 131905 (2007)

[Bae 2007-1]

H. P. Bae, S.R. Bank, H. B. Yuen, T. Sarmiento, E. R. Pickett, M. A. Wistey, J. S. Harris Jr., "Temperature dependencies of annealing behaviors of $\text{GaInNAsSb}/\text{GaNAs}$ quantum wells for long wavelength dilute-nitride lasers", *Appl. Phys. Lett.*, **90**, 231119 (2007).

2006

[Lee 2006-1]

Lee, YW, Sinha, S., Digonnet, M.J.E., Byer, R.L., Jiang, S., "20 W Single-Mode Yb^{3+} Doped Phosphate Fiber Laser", *Optics Letters*, Vol. **31**, No. 22, pp. 3255-3257, (15 November 2006). <http://www.stanford.edu/~rlbyer/2006/422.pdf>

[Sridharan 2006-1]

Sridharan, A.K., Saraf, S., Sinha, S., Byer, R.L., "Zigzag Slabs for Solid-State Laser Amplifiers: Batch Fabrication and Parasitic Oscillation Suppression", *Applied Optics*, Vol. **45**, No. 14, pp. 3340-3351, May 10, 2006. <http://www.stanford.edu/~rlbyer/2006/421.pdf>

[Sinha 2006-1]

Sinha, S., Langrock, C., Digonnet, M.J.F., Fejer, M.M., Byer, R.L., "[Efficient yellow-light generation by frequency doubling a narrow-linewidth 1150 nm ytterbium fiber oscillator](http://www.stanford.edu/~rlbyer/2006/415.pdf)" *Optics Letters*, Vol. **31**, No.3, pp.347-349 (1 February 2006), <http://www.stanford.edu/~rlbyer/2006/415.pdf>

[Bank 2006-2]

S. R. Bank, H. B. Yuen, H. P. Bae, M. A. Wistey, and J. S. Harris Jr., "Over-Annealing Effects in GaInNAs(Sb) Alloys and Their Importance to Laser Applications," *Appl. Phys. Lett.*, **88**, no. 22, p. 221115 (2006).

[Bank 2006-1]

S. R. Bank, H. B. Yuen, H. P. Bae, M. A. Wistey, A. Moto, and J. S. Harris Jr., "Enhanced Luminescence in GaInNAsSb Quantum Wells Through Variation of the Arsenic and Antimony Fluxes," *Appl. Phys. Lett.*, **88**, no. 24, p. 231923 (2006).

[Kuo 2006-1]

P. S. Kuo, K. L. Vodopyanov, M. M. Fejer, D. M. Simanovskii, X. Yu, J. S. Harris, D. Bliss, D. Weyburne. "Optical parametric generation of a mid-infrared continuum in orientation-patterned GaAs." *Opt. Lett.* **31** (1), 71-73 (2006).

http://www.stanford.edu/group/fejer/fejerpubs/2006/Kuo_OL2006.pdf

[Vodopyanov 2006-1]

K. L. Vodopyanov, "Optical generation of narrow-band terahertz packets in periodically inverted electro-optic crystals: conversion efficiency and optimal laser pulse format," *Opt. Express* **14**, 2263-2276 (2006)

[Imeshev 2006]

G. Imeshev, M. E. Fermann, K. L. Vodopyanov, M. M. Fejer, X. Yu, J. S. Harris, D. Bliss, C. Lynch, "High-power source of THz radiation based on orientation-patterned GaAs pumped by a fiber laser", *Opt. Express* **14**, 4439-4444 (2006).

http://www.stanford.edu/group/fejer/fejerpubs/2006/Imeshev_Opt_Express2006.pdf

2005

[Saraf 2005-1]

Saraf, S., Urbanek, K., Byer, R.L., King, P.J., "[Quantum Noise Measurements in a Continuous-Wave Laser-Diode-Pumped Nd:YAG Saturated Amplifier](#)", *Optics Letters*, 15 May 2005, Vol. **30**, No. 10, pp. 1195-1197. <http://www.stanford.edu/~rlbyer/2005/408.pdf>

[Wistey 2005-1]

M.A.Wistey, S.R.Bank, H.B.Yuen, H. Bae, J.S. Harris, "Nitrogen plasma optimization for high-quality dilute nitrides", *Journal of Crystal Growth* **278** (1-4), p.229-33 (2005).

[Bank 2005-1]

S.R. Bank, M.A. Wistey, H.B. Yuen, L.L. Goddard, H.P. Bae, J.S. Harris, "Molecular Beam Epitaxy Growth of Low-Threshold CW GaInNAsSb Lasers at 1.5 μ m," *J. of Vac. Sci. Technol. B*, **23**(3), 1337 (2005).

2004

[Wisdom 2004-1]

Wisdom, J., Dignonnet, M., Byer, R.L., "[Ceramic Lasers: Ready for Action](#)", *Photonics Spectra*, February 2004. <http://www.stanford.edu/~rlbyer/2004/403.pdf>

2003

[Bank 2003-1]

S.R. Bank, M.A. Wistey, H.B. Yuen, L.L. Goddard, W. Ha, and J.S. Harris, "Low-threshold CW GaInNAsSb/GaAs Laser at 1.49 μm ," *Electronics Letters*, **39**, no. 20, p.1445-6 (2003)

2. Conference Proceedings

Lee, Y.W.; Sinha, S.; Digonnet, M.J.F.; Byer, R.L.; and Jiang, S., "10-watt, single-mode, single-frequency, 1.03 μm Yb³⁺-doped phosphate fiber amplifier," *Proceedings of the Quantum Electronics and Laser Science conference on Lasers and Electro-Optics, CLEO/QELS* (2008)

Lee, Y.W.; Sinha, S.; Digonnet, M.J.F.; Byer, R.L.; and Jiang, S., "Measurement of high-photo-darkening resistance in phosphate fiber doped with 12% Yb₂O₃," *Proceedings of SPIE - the International Society for Optical Engineering*, **Vol. 6873** (2008)

Wisdom, J.A; Gaume, R; Route, R; Yan Lin Aung; Ikesue, A; Byer, and R.L., "Design of transverse Nd doping profiles in transparent YAG ceramics for edge-pumped laser geometries," *Proceedings of SPIE - the International Society for Optical Engineering*, **Vol. 6871**, pp. 68711-1-68711-12 (February 7, 2008)

H. Bae, T. Sarmiento, J.S. Harris, "Experimental investigation of temperature dependence of 1.55 μm GaInNAsSb/GaNAs QW lasers grown in MBE", International Semiconductor Laser Conference, Sorento, Italy, Sept.2008

Wisdom, J.A.; Hum, David S.; Digonnet, M.J.F.; Ikesue, A.; Fejer, M.M.; and Byer, R.L., "2.6-watt average-power mode-locked ceramic Nd: YAG laser," *Proceedings of SPIE - the International Society for Optical Engineering*, **Vol. 6469** (2007)

Lee, Y.W.; Urbanek, K.E.; Digonnet, M.J.F.; Byer, R.L.; and Jiang, S., "Measurement of the stimulated Brillouin scattering gain coefficient of a phosphate fiber," *Proceedings of SPIE - the International Society for Optical Engineering*, **Vol. 6469** (2007)

Hum, D.S.; Route, R.K.; Urbanek, K.; Byer, R.L.; Fejer, M.M. "Generation of 10.5-W CW, 532-nm radiation by SHG in vapor-transport- equilibrated, periodically-poled, near-stoichiometric lithium tantalate" Conference on Lasers and Electro-Optics and 2006 Quantum Electronics and Laser Science Conference, CLEO/QELS 2006 (2006)

S. R. Bank, H. P. Bae, H. B. Yuen, L. L. Goddard, M. A. Wistey, T. S. Sarmiento, J. S. Harris Jr., "Low-threshold CW 1.55 μm GaAs-based lasers", OFC (2006)

H. P. Bae, S. R. Bank, M. A. Wistey, H. B. Yuen, E. Pickett, T. Sarmiento, J. S. Harris Jr., "Investigation of GaInNAsSb annealing processes and its implications on GaInNAsSb lasers", Session F6, EMC (2006)

Lee, Y.W.; Sinha, S.; Digonnet, M.J.F.; Byer, R.L.; and Jiang, S. “12-watt single-mode Yb⁺³-doped phosphate fiber laser” Conference on Lasers and Electro-Optics and 2006 Quantum Electronics and Laser Science Conference, CLEO/QELS 2006 (2006)

Sridharan, A.K.; Roussev, R.; Urbanek, K.; Fejer, M.M.; Byer, R.L. “Eyesafe, 1.55 μ m, 1 μ s pulse energy source for space-based remote sensing using optical parametric amplifiers in PPLN” Conference on Lasers and Electro-Optics (CLEO) (2004) p.3 pp. **Vol. 1** (2004)

Saraf, S.; Sinha, S.; Sridharan, A.K.; Byer, R.L. “Power scaling of diffraction limited, single frequency lasers for LIGO” 2003 OSA Topical Meeting on Advanced Solid-State Photonics (ASSP) (Trends in Optics and Photonics Series **Vol. 83**) p.426-31 (2003)

Saraf, S.; Sinha, S.; Sridharan, A.K.; Byer, R.L. “100 W, single frequency, diffraction-limited Nd:YAG MOPA for LIGO” Conference on Lasers and Electro-Optics (CLEO) (IEEE Cat. No.CH37419-TBR) p.3 pp. (2003)

Saraf, Shailendhar; Sinha, Supriyo; Sridharan, Arun Kumar; Byer, Robert L. “100 W, single frequency, diffraction-limited Nd:YAG MOPA for LIGO”. OSA Trends in Optics and Photonics Series **Vol. 88**, p.2145-2147 (2003)

3. Collected Reprints as pdf attachment